UNIVERSIDADE DE SÃO PAULO

INSTITUTO DE FÍSICA

Anisotropia azimutal elíptica de elétrons de decaimentos de quarks pesados em colisões de Pb-Pb a $\sqrt{s_{NN}}$ = 2.76 TeV medida no experimento ALICE

Denise Aparecida Moreira de Godoy

Orientador:

Prof. Dr. Alexandre Alarcon do Passo Suaide

Co-orientador:

Dr. Mateusz Andrzej Ploskon

Tese de doutorado apresentada ao Instituto de Física para a obtenção do título de Doutor em Ciências

Banca Examinadora:

Prof. Dr. Alexandre Alarcon do Passo Suaide (IFUSP)

Prof. Dr. Celso Luiz Lima (IFUSP)

Prof. Dr. Airton Deppman (IFUSP)

Prof. Dr. Takeshi Kodama (UFRJ)

Profa. Dra. Maria Beatriz de Leone Gay Ducati (UFRGS)

São Paulo

2013

FICHA CATALOGRÁFICA

Preparada pelo Serviço de Biblioteca e Informação

do Instituto de Física da Universidade de São Paulo

Godoy, Denise Aparecida Moreira de

Anisotropia azimutal elíptica de elétrons de decaimentos de quarks pesados em colisões de Pb-Pb a $\sqrt{s_{NN}}$ = 2.76 TeV medida no experimento ALICE — São Paulo, 2013.

Tese (Doutorado) — Universidade de São Paulo. Instituto de Física. Departamento de Física Nuclear.

Orientador: Prof. Dr. Alexandre Alarcon do Passo Suaide

Co-orientador: Dr. Mateusz Andrzej Ploskon

Área de Concentração: Física Experimental de Partículas

Unitermos: 1. Quark; 2. Elétrons; 3. Colisões de íons pesados relativísticos.

USP/IF/SBI-119/2013

University of Sao Paulo

Physics Institute

Elliptic azimuthal anisotropy of electrons from heavy-flavour decays in Pb-Pb collisions at $\sqrt{s_{NN}}$ = 2.76 TeV measured with ALICE

Denise Aparecida Moreira de Godoy

Advisor:

Prof. Dr. Alexandre Alarcon do Passo Suaide

Co-advisor:

Dr. Mateusz Andrzej Ploskon

A dissertation submitted in partial satisfaction of the requirements for the degree Doctor of Philosophy in Physics

---

Sao Paulo

2013

Godoy, Denise Aparecida Moreira de

Elliptic azimuthal anisotropy of electrons from heavy-flavour decays in Pb-Pb collisions at $\sqrt{s_{NN}}$ = 2.76 TeV measured with ALICE — São Paulo, 2013.

Thesis — University of Sao Paulo. Physics Institute. Department of Nuclear Physics.

Advisor: Prof. Dr. Alexandre Alarcon do Passo Suaide

Co-advisor: Dr. Mateusz Andrzej Ploskon

Keywords: 1. Quark; 2. Electrons; 3. Relativistic heavy-ion collisions

USP/IF/SBI-119/2013

"Understanding nature surely means taking a close look at its connections, being certain of its inner workings. Such knowledge cannot be gained by understanding an isolated phenomenon or a single group of phenomena, even if one discovers some order in them. It comes from the recognition that a wealth of experimental facts are interconnected and can therefore be reduced to a common principle. In that case, certainty rests precisely on this wealth of facts. The danger of making mistakes is the smaller, the richer and more complex the phenomena are, and the simpler is the common principle to which they can all be brought back." Physics and Beyond: Encounters and Conversations, by Werner Heisenberg.

Acknowledgments

I would like to thank people that contributed, direct or indirectly, to this project. First, I would like to thank my advisor, Alexandre Suaide, for his guidance and patience. I am grateful to my co-advisor at CERN, Mateusz Ploskon, for all fruitful discussions and suggestions. I also would like to thank Shingo Sakai for his interest in this project and for sharing his experience.

I am really grateful to Raphaelle Bailhache and Theodor Rascanu for their collaboration in this project and for all discussions.

Many thanks to the EMCal group, particularly to Constantin Loizides and Mauro Cosentino, for all useful discussions concerning the electron analysis. Thanks to my officemates at CERN, Tomas Aronsson and Rongrong Ma, for all discussions and technical supports.

I would like to thank the heavy-flavour and flow groups at ALICE for their interest and useful suggestions. Particularly, I am grateful to Andrea Daianese, Philippe Crochet, Ralf Averbeck, Francesco Prino, Ilya Selyuzhenkov, and Sergei Voloshin for the fruitful discussions of my analysis.

Many thanks to people from my group in University of Sao Paulo for their help: Antonio, Caios, Camila, Cristiane, Danilo, Diogenes, Elienos, Gabriel, Lucas, Marcel, and Renato. In particular, I am grateful to Marcelo Munhoz and Nelson Carlin for their interest in this project and administrative help.

Thanks to my friends Alexandra, Ana, Cesar, Gabriela, Leonardo, Lucas, Luciene, Mariana, Mariane, Paulo, Tatiane, and Ulisses for sharing great years of studies.

I would like to thank Coordenação de Aperfeiçoamento de Pessoal de Nível Superior (CAPES), and Conselho Nacional de Desenvolvimento Científico e Tecnológico (CNPq) for the financial support.

Finally, I would like to thank my family for giving me support. I dedicate this thesis to them.

Resumo

Nessa tese serão apresentadas medidas de anisotropia azimutal elíptica de elétrons de decaimentos de quarks pesados feitas no experimento de colisão de íons pesados ALICE (A Large Ion Collider Experiment, em inglês). As medidas foram obtidas em colisões de Pb-Pb com energia de centro de massa por par de nucleons ($\sqrt{s_{NN}}$) igual a 2.76 TeV com o colisor de hadrons LHC (Large Hadron Collider, em inglês).

Colisões ultrarelativísticas de íons pesados podem alcançar temperaturas e/ou densidades de energia suficientemente altas para formar o Plasma de Quarks e Gluons (QGP, na sigla em inglês), o estado da matéria onde os partons estão desconfinados dos hadrons.

O parâmetro de anisotropia azimutal elíptica é um dos observáveis mais importantes utilizados no estudo da formação do QGP. Esse parâmetro é quantificado pelo segundo harmônico, denominado v_2, da distribuição do ângulo azimutal das partículas em relação ao ângulo do plano de reação, o qual é definido pela direção do parâmetro de impacto e pela direção do feixe de partículas. Medidas de anisotropia azimutal elíptica de quarks pesados (charm e beauty) são interessantes, pois os quarks pesados são sondas sensíveis às propriedades do QGP, visto que eles são predominantemente produzidos em processos iniciais de espalhamento duro e interagem com o meio desconfinado.

Medidas de v_2 de elétrons de decaimentos de quarks pesados em baixos valores de momento transversal indicam movimento coletivo de quarks pesados e possível termalização no QGP. Por outro lado, medidas de v_2 de elétrons de decaimentos de quarks pesados em altos valores de momento transversal são interpretadas como uma dependência da geometria do meio por onde os quarks pesados atravessam e perdem energia.

Serão mostrados resultados de v_2 de elétrons de decaimentos de quarks pesados em função do momento transversal em colisões de Pb-Pb a $\sqrt{s_{NN}}$ = 2.76 TeV em eventos com centralidades 20-40% e 30-50%. O resultado é comparado com previsões teóricas e medida obtida em colisões de Au-Au a $\sqrt{s_{NN}}$ = 0.2 TeV no experimento RHIC. Resultados preliminares de v_2 de elétrons de decaimentos de charm e beauty, separadamente, também serão mostrados em colisões de Pb-Pb a $\sqrt{s_{NN}}$ = 2.76 TeV em eventos com centralidade 30-50%.

Abstract

This thesis presents measurements of the elliptic azimuthal anisotropy of electrons from heavy-flavour decays with the A Large Ion Collider Experiment (ALICE). The measurement is performed for the first time in Pb-Pb collisions at center-of-mass energy per colliding nucleon pair $\sqrt{s_{NN}}$ = 2.76 TeV at the Large Hadron Collider (LHC).

In heavy-ion collisions at ultrarelativistic energies sufficiently high temperature and/or energy density can be achieved to form the Quark-Gluon Plasma (QGP), the state of matter predicted by Quantum Chromodynamics (QCD) in which quarks and gluons are deconfined from hadrons. One of the most important probes of the QGP formation is the elliptic azimuthal anisotropy, which is quantified by the second harmonic v_2 of the particle azimuthal angle distribution with respect to the angle of the reaction plane, which is defined by the impact parameter direction and the beam direction. In addition, heavy quarks (charm and beauty) serve as a sensitive probe of the QGP properties since they are predominantly produced in initial hard scattering processes and interact with the deconfined medium.

The transverse momentum dependence of the heavy-flavour decay electron v_2 can be used to investigate the QGP properties. The measurement of v_2 of electrons from heavy-flavour decays at low transverse momentum provides a way to test whether heavy quarks take part in the collective motion in the medium. Whereas, v_2 of electrons from heavy-flavour decays at high transverse momentum is interpreted as a path length dependence of heavy-quark energy loss within the created dense medium.

Results of the elliptic azimuthal anisotropy of electrons from heavy-flavour decays as a function of tranverse momentum obtained in 20-40% and 30-50% central Pb-Pb collisions at $\sqrt{s_{NN}}$ = 2.76 TeV will be shown. The measurement is compared with theoretical predictions and previous measurement at the RHIC experiment. Preliminary measurements of the elliptic azimuthal anisotropy of electrons from charm and beauty as a function of tranverse momentum in 30-50% central Pb-Pb collisions at $\sqrt{s_{NN}}$ = 2.76 TeV will be shown as well.

Contents

List of Figures

List of Tables

1

Introduction

Heavy-ion collisions at high energies can achieve sufficiently high temperature and/or energy density to form the quark-gluon plasm (QGP). The QGP is a state of matter predicted by the Quantum Chromodynamics (QCD), in which quarks and gluons are deconfined from hadrons.

The hadronic matter undergoes a phase transition to the QGP at extremely high temperature or baryonic chemical potential. These conditions are expected to be similar to the early Universe and core of neutron stars, respectively. According to lattice QCD calculations performed at zero baryon chemical potential, the temperature of transition from the hadronic matter to the QGP is approximately 170 MeV, which corresponds to an energy density $\varepsilon \approx 1$ GeV/fm^3. As an example of capability of the current experiments of heavy-ion collisions, the energy density obtained in Au-Au collisions at $\sqrt{s_{NN}} = 0.2$ TeV at RHIC is approximately 15 GeV/fm^3.

Elliptic azimuthal anisotropy is one of the most important probes of the QGP formation in experiments of heavy-ion collisions at high energy and it is related to the collective motion of particles due to the pressure gradients created in early stages of non-central collisions. The overlap region of non-central

collisions has almost an ellipsoidal shape, which results in an initial spatial distribution of the created particles with predominantly the same shape. If the QGP is created after such collisions, the initial spatial anisotropy of the created particles is converted to momentum space anisotropy since the pressure gradient is larger along the impact parameter direction compared to the other directions. Once the spatial anisotropy decreases with the expansion of the QGP, the anisotropic flow is sensitive to the particle interactions in early stages of the collision. On the other hand, if the QGP is not created, particles move freely and the momentum space anisotropy of emitted particles can not be observed.

The elliptic azimuthal anisotropy is quantified by the second parameter v_2 of the azimuthal distribution of the emitted particles with respect to the azimuthal angle of the reaction plane, which is defined by the impact parameter direction and the beam direction. The reaction plane is not measured in the experiment, but it can be estimated from event-plane angle, which is obtained from the angle of symmetry of the particle azimuthal distribution in the transverse plane.

This thesis presents measurements of elliptic azimuthal anisotropy of electrons from heavy-flavour decays. Heavy flavours are produced in initial stage of collisions via hard partons processes and experience the full evolution of the medium created in heavy-ion collisions at high energy. Since only particles resulting from the heavy-quark fragmentation can be detected, the semileptonic heavy-flavour decay to inclusive electron channel is used to investigate elliptic azimuthal anisotropy of heavy flavours.

Elliptic azimuthal anisotropy of electrons from heavy-flavour decays is measured with ALICE, the LHC experiment dedicated to study heavy-ion collisions at ultrarelativistic energies. ALICE has several sub-systems, which provide high capability for the particle identification. The electrons are identified with the TPC and EMCal detectors. The identification using the TPC detector is based on the measurement of the specific energy loss in the detector. Electron identification with the EMCal is based on the E/p distribution, where E is the energy measured with the EMCal and p is the total momentum of the particle. The E/p distribution for electrons is around unity, since they deposit all their energy in the EMCal detector.

The azimuthal angle of the identified electrons and the event-plane angle are correlated in order to obtain the elliptic azimuthal anisotropy of the electrons. However the electron sample identified in the experiment contains electrons from heavy-flavour decays and background electrons (electrons from photon conversions, Dalitz decays of light neutral mesons, direct photons from hard scattering processes, $K \rightarrow e\pi\nu$ decays, dielectron decays of light vector mesons, heavy quarkonia, etc). Therefore the con-

tribution of the background electron v_2 must be obtained and subtracted from the identified electron v_2. In this analysis, the background electron v_2 is evaluated with Monte Carlo simulation based on the measured yield and v_2 of the main background sources.

Measurements of the elliptic azimuthal anisotropy of electrons from heavy-flavour decays are presented for the first time in 20-40% and 30-50% central Pb-Pb collisions at $\sqrt{s_{NN}}$ = 2.76 TeV with ALICE. Previous measurement of the prompt D mesons is used to obtain, for the first time, the preliminary measurement of the elliptic azimuthal anisotropy of electrons from charm and beauty, separately, in 30-50% central Pb-Pb collisions at $\sqrt{s_{NN}}$ = 2.76 TeV with ALICE.

Details of the measurement and discussion of the results will be shown in this thesis.

2

Quark-Gluon Plasma

In this chapter the main aspects of the Quark-Gluon Plasma (QGP) will be discussed. Section 2.1 contains an introduction of the theory of strong interactions, the so-called Quantum Chromodynamics (QCD). The relevant aspects of the theory will be presented, with particular focus on the asymptotic freedom. The Quark-Gluon Plasma will be discussed in Section 2.2 and experimental evidences of the formation of the QGP in heavy-ion collisions will be shown in 2.2.3.

2.1. Quantum Chromodynamics (QCD)

In early 1930s, only three constituents of matter were known (protons, neutrons, and electrons) and the challenge was to explain the attraction between proton and neutron inside the atomic nucleus [1, 2].

When particle accelerators started to be used as a tool in Particle Physics in 1950s, the number of discovered particles increased enormously. In order to classify the new particles, Gell-Mann and Zweig proposed independently a geometrical scheme, which is based on the quantum numbers of charge and

strangeness of baryons and mesons [1, 2]. The scheme was a first step of the *quark model* that classifies particles according to elementary constituents, which are called *quarks* [1, 2, 3, 4, 5, 6]. In this model, baryons are composed of three quarks and mesons are composed of a quark and an anti-quark.

The existence of quarks was first observed in inelastic electron-proton collisions, the so-called *Deep Inelastic Scattering (DIS)*, at the Stanford Linear Accelerator Center (SLAC) [7]. Two theoretical results contributed to the interpretation of the proton structure observed at the SLAC. The first one is the *parton model* [1, 2, 3, 4, 5, 6] proposed by Feynman, in which quarks are assumed to be pointlike constituents inside the hadrons. The second one is the *scaling* [1, 2, 3, 4, 5, 6], proposed by Bjorken, who showed that the structure functions that describe the cross section of electron-proton collisions can be written in terms of the fraction of the momentum carried by quarks inside the nucleon in collisions at high energy. The electric charge and spin of the quarks were also observed in inelastic electron-proton collisions at the SLAC [7].

In 1964 Greenberg proposed that quarks carry a quantum number called *color* to explain the inconsistency with the Pauli principle observed in the Δ^{++} baryon [1, 2, 3, 4, 5, 6], which consists of three up quarks with spins aligned in the same direction.

Color and gluons, which are mediators of the strong interactions, were observed in electron-positron collisions [1, 2, 3, 4, 5, 6]. The evidence of the color was obtained from the ratio of the electron-positron cross sections into hadrons and di-muons, $R = \sigma(e^-e^+ \to H)/\sigma(e^-e^+ \to \mu^-\mu^+)$, which is proportional to the number of colors [1, 2, 3, 4, 5, 6]. Gluons were observed experimentally in fragmentations of electron and positron into three jets ($e^-e^+ \to q\bar{q}g$) [1, 2].

The current theories that describe elementary particles and their interactions except gravity are grouped into the *Standard Model* [1, 2, 3, 4, 5, 6]. According to this theory, the elementary particles are composed of leptons, quarks, and mediators. Quarks have degrees of freedom called flavour (up, down, strange, charm, bottom, and top) and carry fractional electric charge in addition to a quantum number named color (red, green, and blue). They interact strongly by exchange of gluons, which are mediators without mass, electric charge and flavour. However, gluons are bicolored so they interact strongly among themselves. Table 2.1 shows some properties of quarks and gluons.

The gauge field theory that describes the strong interaction of quarks and gluons, the so-called *Quantum Chromodynamics* (QCD), was proposed by Fritzch, Gell-Mann and Leutwyler in 1973 [1, 2, 3, 4, 5, 6]. The SU(3) algebra is used in the QCD theory to guarantee that hadrons are singlets under rotations

	symbol	charge	spin	mass (GeV)
up	u	2/3	1/2	$(2.3^{+0.7}_{-0.5}) \times 10^{-3}$
down	d	-1/3	1/2	$(4.8^{+0.7}_{-0.3}) \times 10^{-3}$
strange	s	-1/3	1/2	$(95 \pm 5) \times 10^{-3}$
charm	c	2/3	1/2	1.275 ± 0.025
bottom	b	-1/3	1/2	4.18 ± 0.03
top	t	2/3	1/2	$173.5 \pm 0.6 \pm 0.8$
gluon	g	0	1	0

Table 2.1.: Charge, spin, and mass of quarks and gluons [8].

in color space, since they are neutral states. Indeed, quarks and gluons are not observed as free particles, the so-called *color confinement* phenomenon [1, 2, 3, 4, 5, 6]. The non-abelian character of the SU(3) algebra results in self-interaction of gluons.

The QCD Lagrangian is given by [1, 2, 3, 8]:

$$\mathcal{L}_{QCD} = \sum_f \bar{q}_f \left(i\gamma^\mu D_\mu - m_f \right) q_f - \frac{1}{4} G_a^{\mu\nu} G^a_{\mu\nu} \,, \tag{2.1}$$

where f indicates the flavour, m_f indicates the mass, q_f represents the quark-field spinors, $G_a^{\mu\nu}$ are the gluon fields, γ^μ are the Dirac matrices, D^μ is the covariant derivative, which is defined as [1, 2, 3, 8]:

$$D^\mu q_f \equiv \left[\partial^\mu - i g_s \frac{\lambda^a}{2} G_a^\mu \right] q_f \,, \tag{2.2}$$

where $\lambda^a (a = 1, ..., 8)$ are 3×3 hermitian and traceless matrices that denote the generators of the SU(3) algebra.

Calculations of physical observables in perturbative QCD (pQCD) are expressed as a series expansion in terms of the *strong coupling* $\alpha_s = g_s^2/4\pi$, which diverges in one or more loop corrections [1, 2, 3, 4, 5, 6, 8, 9]. However the divergences can be removed by redefining the fields and couplings in the renormalization procedure. In this case, the physical observables can be expressed in terms of the renormalized coupling $\alpha_s(\mu^2)$, where μ is the renormalization scale.

From the calculation of 1-loop Feynman diagrams that contribute to the renormalization of the strong coupling, the *running coupling* $\alpha_s(Q^2)$ is given by [1, 2, 3, 8]:

$$\alpha_s \left(Q^2 \right) = \frac{\alpha_s \left(\mu^2 \right)}{1 + \alpha_s \left(\mu^2 \right) \frac{11 N_c - 2 N_f}{12\pi} \ln \left(\frac{Q^2}{\mu^2} \right)} \,, \tag{2.3}$$

where N_f is the number of active flavours at the scale energy Q, and $N_c = 3$ is the number of colors.

Normally the running coupling is expressed conveniently in terms of a scale (Λ_{QCD}) that limits the validation of perturbative QCD. It is expected that Λ_{QCD} ranges from 100 MeV to 300 Mev[3]. The running coupling in terms of Λ_{QCD} is given by [1, 2, 3, 8]:

$$\alpha_s(Q^2) = \frac{12\pi}{11N_c - 2N_f \ln \frac{Q^2}{\Lambda^2_{QCD}}} \,. \tag{2.4}$$

Perturbative QCD can be used to describe the so-called *hard processes*, which correspond to processes involving large momentum transfer ($Q > \Lambda_{QCD}$) [1, 2, 3, 4, 5, 6, 8, 10]. The *soft processes* involve low energy ($Q \to \Lambda_{QCD}$) and can not be treated by perturbative QCD, since the series in terms of the running coupling diverges. These processes are treated by lattice QCD.

Equation 2.4 shows that, for $N_f \leq 16$, the running coupling decreases when the energy scale increases or when distance between quarks decreases. When $Q \gg \Lambda_{QCD}$, the strong interaction of partons becomes weak and they can be treated as free particles. This phenomenon is called *asymptotic freedom* [1, 2, 3, 4, 5, 6, 8, 10]. On the other hand, the running coupling increases when the energy scale decreases or the distance increases. For instance, when the distance between a quark and an anti-quark within a meson is increased, it becomes energetically favorable to produce a new pair of quark and anti-quark from the vacuum in order to combine and form a new meson.

Figure 2.1 shows the running coupling α_s as a function of energy scale Q. Experimental results of α_s at different energy scales agree, within uncertainties, with the asymptotic freedom predicted by QCD calculations [10, 11].

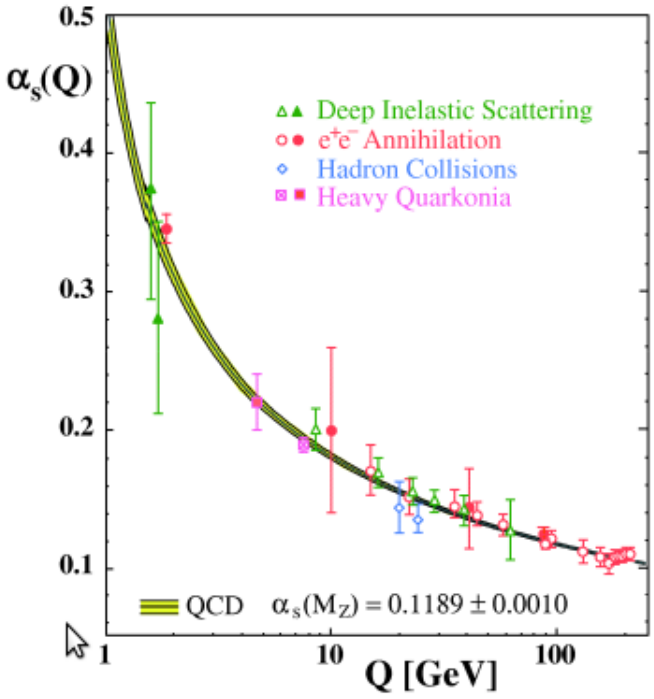

Figure 2.1.: Measurements of the running coupling $\alpha_s(Q)$ as a function of energy scale Q. The results are compared with theoretical prediction [10].

2.2. Quark-Gluon Plasma in heavy-ion collisions

As discussed in the previous section, quarks can be treated as free particles in processes involving high energy or small distance. It is expected that a state with deconfined parton constituents, the so-called *Quark-Gluon Plasma* (QGP), occurred in early Universe, where the temperature was extremely high, and it is present in the core of neutron stars, where the nuclear matter is extremely compressed [12].

The phase transition from the hadronic matter to the QGP can be illustrated by the QCD phase diagram (Fig. 2.2) of temperature as a function of baryon chemical potential $\mu_B = \partial E/\partial N_B$ [13], even though the boundary lines are not known precisely. The baryon chemical potential corresponds to the energy required to add a baryon to a system at constant volume and entropy. Experimentally, the baryon chemical potential is estimated by the net baryon density.

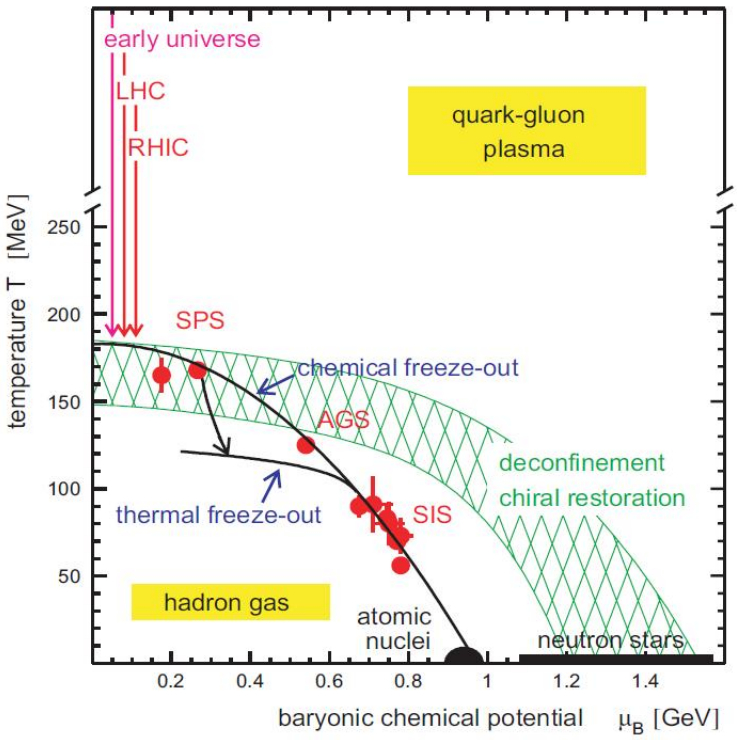

Figure 2.2.: Illustration of the QCD phase diagram [13].

At ordinary temperatures and baryonic chemical potential greater than approximately 0.94 GeV, which corresponds to the proton mass [8], quarks and gluons are confined within the atomic nucleus. At temperatures greater than the nuclear binding energy, the nuclear matter becomes a hadron gas, and, at extremely high temperatures and low baryon chemical potential, the hadronic matter undergoes a phase transition to the QGP [14]. The phase transition also occurs at low temperature and extremely high baryon chemical potential.

Collision of heavy ions at high energy, which can achieve extreme conditions of temperature and/or energy density [15, 16], is the only known way to form the QGP in the laboratory. Collider experiments, for instance the Relativistic Heavy-Ion Collider (RHIC) and the Large Hadron Collider (LHC), have been used to investigate whether the properties of system created in ultrarelativistic heavy-ion collisions resemble the QGP.

2.2.1. Phase transition

Lattice QCD thermodynamics have been used to study the QCD phase transition and the equation of state [17, 18, 19, 20]. According to lattice QCD calculations performed at $\mu_B = 0$, the temperature of transition from a hadronic phase to a partonic phase occurs at $T_c \approx 170$ MeV, which corresponds to an energy density $\varepsilon \approx 1$ GeV/fm^3 [19].

Theoretical predictions show that the equation of state of an ideal gas with gluons and massless quarks at zero chemical potential and extremely high temperature is determined only by the number of degrees of freedom [20]:

$$\frac{\varepsilon_{SB}}{3T^4} = \frac{p_{SB}}{T^4} = \left[2(N_c - 1) + \frac{7}{2} N_c N_f\right] \frac{\pi^2}{90}, \tag{2.5}$$

where ε_{SB} and p_{SB} are, respectively, the Stefan-Boltzmann energy density and pressure, T is the temperature, N_f is the number of flavours, and N_c is the number of colors.

Figure 2.3 shows the energy density and pressure normalized by the temperature to the fourth power as a function of temperature [18, 19, 20]. The critical temperature is approximately 175 MeV in 2-flavour QCD. The calculations were done for N_f = 0, 2 and 3 light quarks as well as two light quarks and one heavy quark [18, 19, 20]. The arrows indicate the Stefan-Boltzmann values from the Eq. 2.5 for a system of free massless quarks at asymptotic high temperatures.

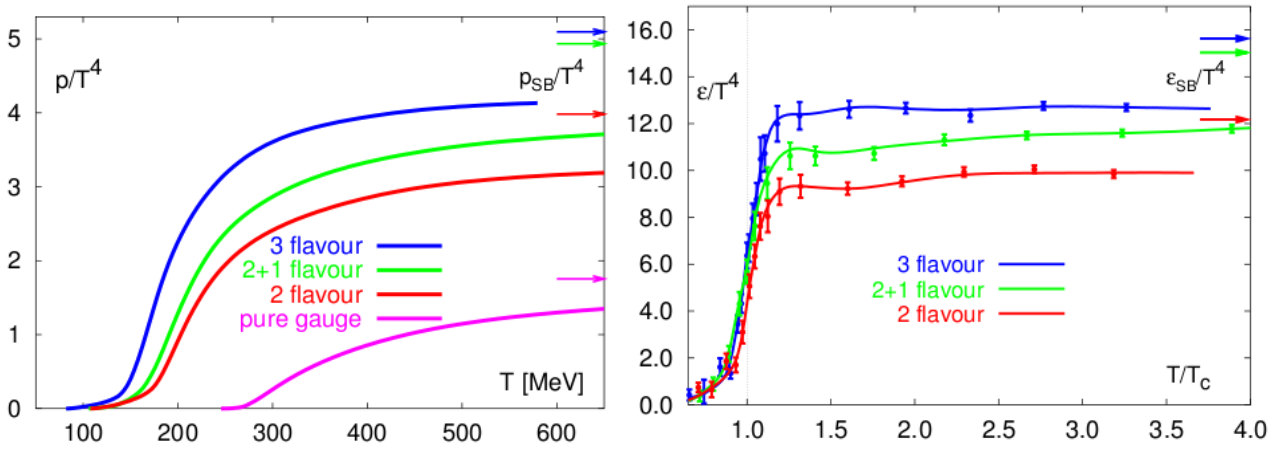

Figure 2.3.: Equation of state predicted by lattice QCD of a QGP composed of 3 light flavours, 2 light flavours, and 2 light flavours and 1 heavy flavour [18].

The equation of state shows three different behaviors, which are more pronounced in the right panel of Fig. 2.3 [18]:

- $T < T_c$: quarks and gluons are confined within the hadrons and the equation of state is well parametrized by a hadron gas [18];
- $T \approx T_c$: the abrupt rise, which is a similar behavior of systems in a phase transition, indicates a change in the number of degrees of freedom (see Eq. 2.5);
- $T > T_c$: quarks and gluons are deconfined, which means they can travel distances larger than typical size of hadrons. The level of saturation depends on the number of degrees of freedom.

Thermodynamic properties of the QGP can be evaluated from the equation of state, energy-momentum and current conservation laws, which form a closed system of equations in terms of the thermodynamic variables [21].

2.2.2. Space-time evolution

The relativistic hydrodynamics model is convenient to describe the space-time evolution of the QGP due to the simplicity of the dynamical description and non-requirement of microscopic details [19, 21, 22]. The idea of describing the evolution of the medium produced in nucleus-nucleus collisions with hydrodynamics was first suggested by Landau in 1953 [23].

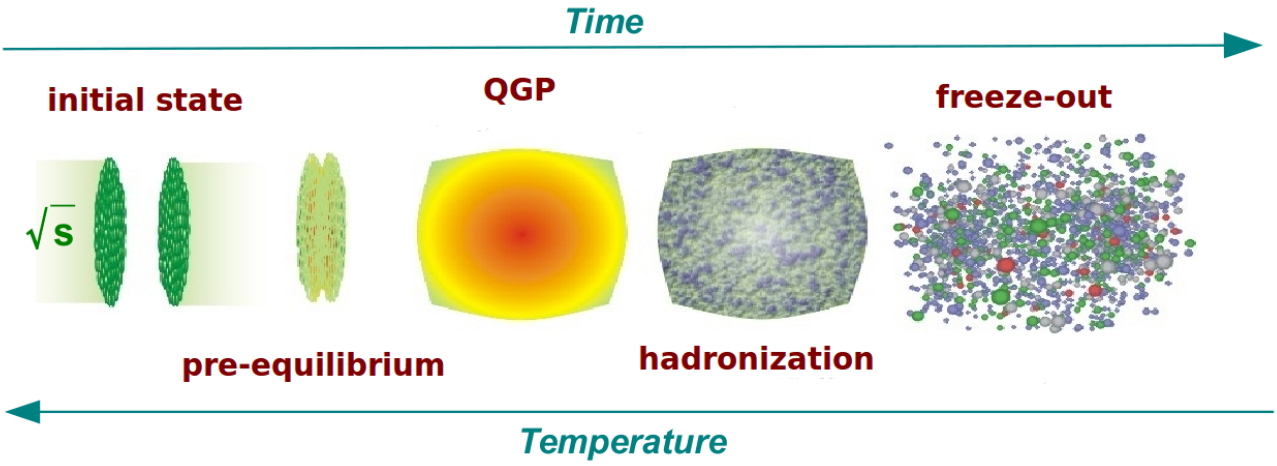

Figure 2.4.: Time evolution of the QGP created in relativistic heavy-ion collisions [24].

The time evolution of the QGP created in heavy-ion collisions at high energy is illustrated in Figure 2.4. At the initial state, Lorentz contracted nuclei coming from opposite directions collide with each other and thousands of secondary particles are created in a small volume. The formed system expands

due to the pressure gradients created in early stages of the collision. The created particles interact inelastically and, if the interactions are sufficiently strong, the system reaches thermal equilibrium. This transient phase between the initial state and the QGP is called pre-equilibrium [19].

The pre-equilibrium stage can not be described by the hydrodynamic model, since the production of particles is not an adiabatic process. However, the description of this stage is essential to obtain the initial particle distribution, which is the initial condition in the hydrodynamic model, and must be obtained from another model, for instance, the wounded nucleon model [19].

The QGP created in experiments of heavy-ion collisions appears to be in local thermodynamic equilibrium, which means that the pressure and temperature of the system vary slowly in the neighborhood [19, 21]. In terms of interactions, the mean free path of the particles is much smaller than the dimensions of the system.

The dynamics of the QGP is determined by the equation of state and conservation laws of energy, momentum and current. The conservation of energy and momentum is given by [19, 21]:

$$\partial_\mu T^{\mu\nu} = 0 \,, \tag{2.6}$$

where $T^{\mu\nu}$ is the energy-momentum tensor. For a viscous and relativistic fluid, the energy-momentum tensor can be expressed as [19, 21]:

$$T^{\mu\nu} = \varepsilon u^\mu u^\nu - P\Delta^{\mu\nu} + W^\mu u^\nu + W^\nu u^\mu + \pi^{\mu\nu} \,, \tag{2.7}$$

where ε is the energy density, P represents the hydrostatic and bulk pressure, W^μ is the energy tensor, $\pi^{\mu\nu}$ is the shear stress tensor. In this equation $u^\mu = (1,0,0,0)$ is the 4-velocity of the fluid, and the tensor operator is defined as $\Delta^{\mu\nu} = g^{\mu\nu} - u^\mu u^\nu$, where $g^{\mu\nu} = diag(1,-1,-1,-1)$ is the Minkowsk metric tensor.

The conservation of the current is given by [19, 21]:

$$\partial_\mu N_i^\mu = 0 \,, \tag{2.8}$$

where N_i^μ is the i-th conserved current, which is given by [19, 21]:

$$N_i^\mu = n_i u^\mu + V_i^\mu \,, \tag{2.9}$$

n_i is the conserved charge density (baryon number, electric charge, strangeness, etc), and V_i^μ is the charge

current.

When the system reaches the critical temperature T_c, the local thermal equilibrium breaks down and the partons start to group into hadrons. The particles interact inelastically until the chemical freeze-out and elastically until the kinetic freeze-out. After the kinetic freeze-out phase, the particles propagate to the detectors without interaction [19].

Relativistic hydrodynamics can not be used to describe the space-time evolution of the hadron gas formed after the QGP. This phase can be described by other models, for instance the *Cooper-Frye model* [19, 21], which assumes that the hadron gas is an ideal gas and the particles have the same momentum distribution as in the QGP.

2.2.3. Experimental evidences

The transverse energy of the emitted particles with respect to rapidity (see rapidity definition in Appendix B.1) dE_T/dy can be used to obtain the initial energy density of the collision, as it was shown by Bjorken [25, 26]:

$$\langle \varepsilon_{Bj}(\tau_{\text{form}}) \rangle \tau_{\text{form}} = \frac{1}{A} \frac{dE_T(\tau_{\text{form}})}{dy} , \tag{2.10}$$

where A is nuclear overlap region, and τ_{form} is the time of formation of the secondary particles.

Figure 2.5 shows $\varepsilon_{Bj}\tau$ as a function of the number of participant nucleons of the nuclei collisions (N_p) measured with PHENIX. It is estimated that $\tau \approx 0.35$ fm/c [25], which corresponds to $\langle \varepsilon \rangle = 15$ GeV/fm^3 in central Au-Au collisions at $\sqrt{s_{\text{NN}}} = 0.2$ TeV, i.e. 15 times larger than the required value to form the QGP according to QCD calculations.

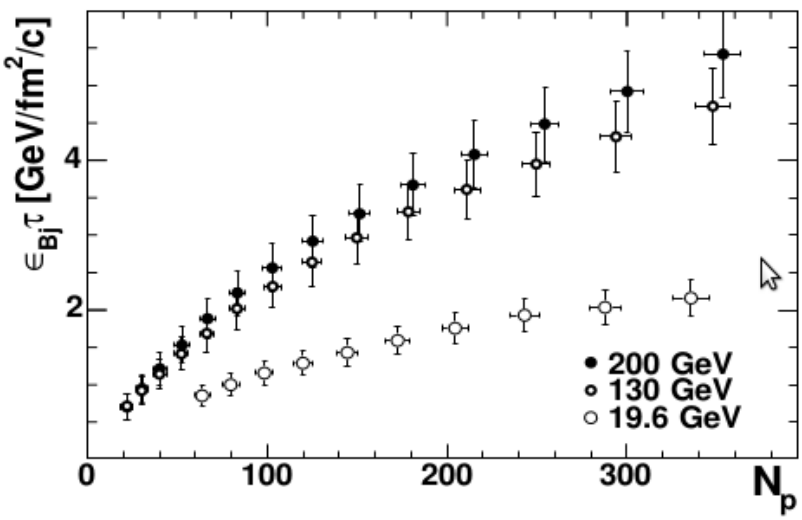

Figure 2.5.: Initial energy density of the collision region times the proper time of the secondary particle production ($\varepsilon_{Bj}\tau$) as a function of the number of participant nucleons (N_p) measured with PHENIX [25].

Figure 2.6 shows the azimuthal correlation between hadrons with $p_T > 2$ GeV/c and a trigger hadron with $p_T^{trig} > 4$ GeV/c in pp, p-Au and Au-Au collisions measured with STAR [27]. The peak at $\Delta\varphi \approx 0$ corresponds to the azimuthal correlation of a hadron pair from a single jet and the peak at $\Delta\varphi \approx \pi$ corresponds to the azimuthal correlation of a hadron pair from back-to-back dijets. A suppression of the peak at $\Delta\varphi \approx \pi$ is observed in Au-Au collisions, which suggests that the suppression is due to the interaction of partons or their fragmentation products with the medium created in Au-Au collisions.

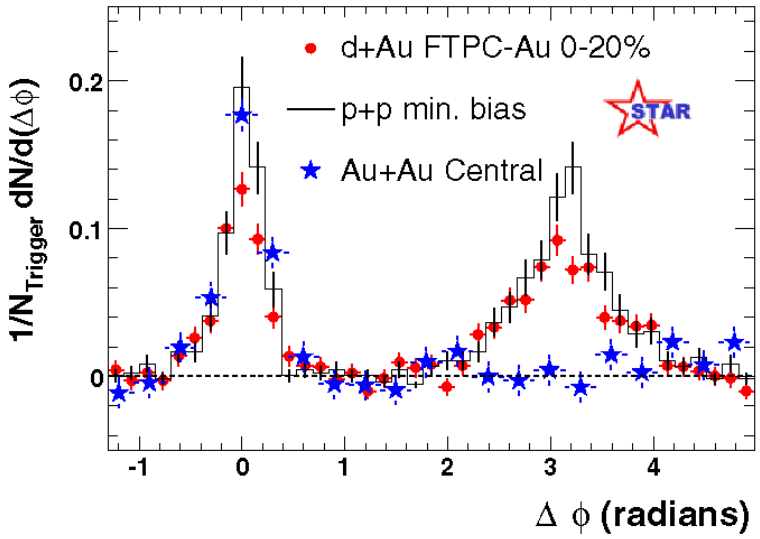

Figure 2.6.: Dihadron azimuthal correlations at high transverse momentum in pp, central d-Au, and central Au-Au collisions measured with STAR [27].

The nuclear modification factor is used to compare the production of particles in nucleus-nucleus

collisions with respect to the production in proton-proton collisions. The observable is defined as [27]:

$$R_{\mathrm{AA}}(p_{\mathrm{T}}) = \frac{1}{\langle N_{coll} \rangle} \frac{dN_{AA}/dp_{\mathrm{T}}}{dN_{pp}/dp_{\mathrm{T}}}, \tag{2.11}$$

where dN_{AA}/dp_{T} is the differential yield in nucleus-nucleus collisions, dN_{pp}/dp_{T} is the differential yield in pp collisions, and $\langle N_{coll} \rangle$ is the number of binary collisions. One expects $R_{\mathrm{AA}} = 1$ in absence of initial and final state effects in nuclear collisions [27], i.e. the nucleus-nucleus collision can be interpreted as a superimposition of nucleon-nucleon collisions. $R_{\mathrm{AA}} < 1$ indicates suppression of particles, which can be related to the interaction of particles with the dense medium created in heavy-ion collisions [27]. However the suppression of particles can also be related to initial state effects, such as nuclear modification of parton density function, saturation for small-x gluons, etc. The contribution of the initial state effects is obtained with the R_{pA}, which compares the production of particles in proton-nucleus collisions and proton-proton collisions[28, 29].

Figure 2.7 shows the nuclear modification factor R_{AA} of J/Ψ ($c\bar{c}$) as a function of the average number of participant nucleons in nucleus-nucleus collisions measured with ALICE and PHENIX experiments at forward rapidity. A strong suppression of J/Ψ is observed in both measurements and the suppression increases in more central collisions.

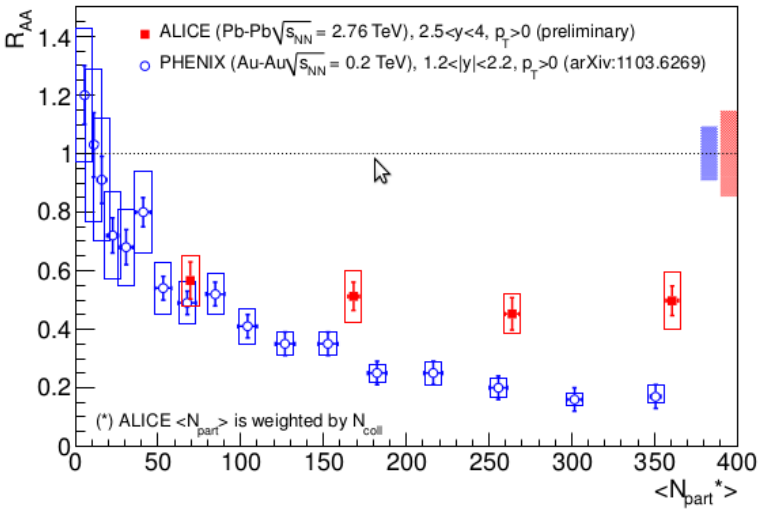

Figure 2.7.: J/Ψ R_{AA} as a function of the average number of participant nucleons in Pb–Pb collisions at $\sqrt{s_{\mathrm{NN}}}$ = 2.76 TeV compared to PHENIX results in Au-Au collisions at $\sqrt{s_{\mathrm{NN}}}$ = 0.2 TeV [30]. Error bars are the statistical uncertainties, empty boxes are the total systematic uncertainties, and the filled box centered at $R_{\mathrm{AA}} = 1$ depicts the normalization uncertainty.

The average of the transverse momentum of the quarks in the beginning of the QGP is expected to be

zero, since the particle production is isotropic. Therefore an anisotropy in the distribution of transverse momentum of the emitted particles caused by pressure gradients in early stages of the collision indicates a collective motion of the particles in the created medium. This evidence of the QGP formation is the focus of this thesis and it will be discussed in details in Chapter 4.

3

Heavy flavours

Heavy flavours are produced in initial stage of collision via hard parton scattering processes. They propagate through the dense medium created in heavy-ion collisions and loss energy via elastic scattering and gluon radiation mechanisms. The production of the heavy flavours will be discussed in Section 3.1 and the energy loss of the heavy quarks in the QGP will be discussed in Section 3.2. Some relevant measurements will be shown in Section 3.3.

3.1. Production of heavy flavours

The production of heavy flavours can be calculated by the perturbative QCD [31, 32, 33, 34, 35], since their masses (see Tab. 2.1) are larger than the QCD perturbation scale Λ_{QCD}.

Figure 3.1 shows the main Feynman diagrams of heavy-flavour production in nucleus-nucleus collisions. Heavy flavours can be produced by pair annihilation and gluon fusion processes of leading-order (LO) Feynman diagrams $O(\alpha_s^2)$. Processes of heavy-flavour productions that include corrections, and

therefore have more accurate description of the production, are included in next-to-leading order (NLO) Feynman diagrams $O(\alpha_s^3)$. These processes include pair creation with gluon emission, flavour excitation, gluon splitting, etc[32].

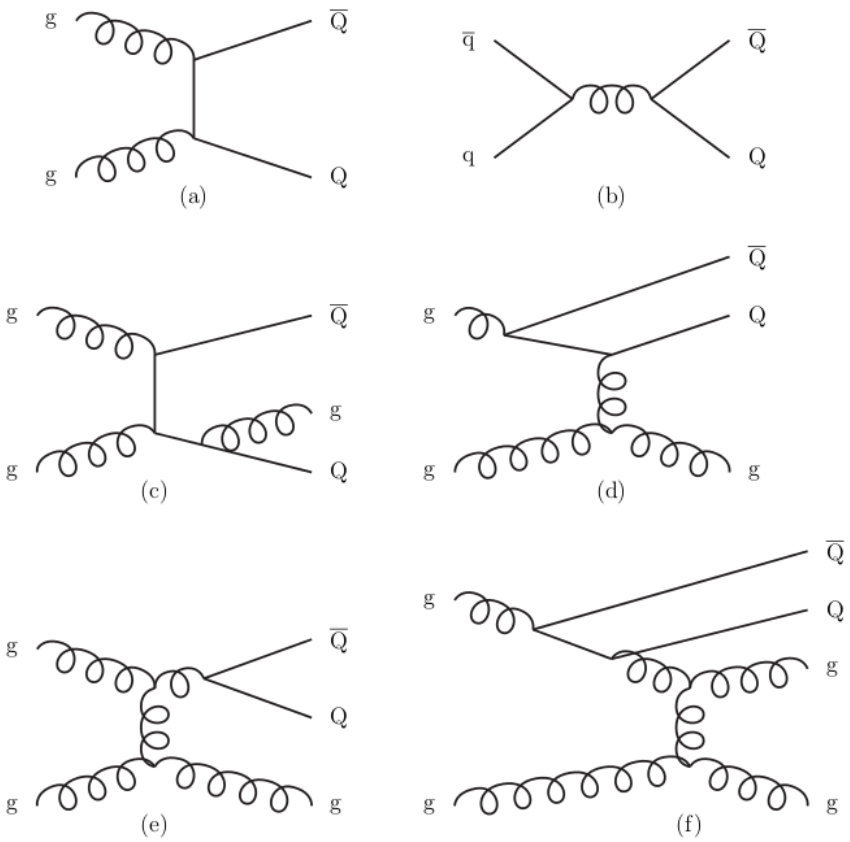

Figure 3.1.: Main diagrams of heavy-flavour production mechanisms in nuclei collisions. LO processes: (a) gluon fusion, (b) pair annihilation. NLO processes: (c) pair creation with gluon emission, (d) flavour excitation, (e) gluon splitting, (f) Gluon splitting of flavour-excitation character[32].

In heavy-ion collision at high energy, gluon fusion is the predominant process of heavy-flavour production since the LO order is the predominant process and the density of gluons is higher at high energy.

Since only particles resulting from the heavy-quark fragmentation can be detected, a channel decay needs to be used in order to investigate the heavy-quark production. In this analysis, the semileptonic heavy-flavour decays to inclusive electrons [36, 37] (Figure 3.2) were used to measure elliptic azimuthal anisotropy of heavy flavours. The branching ratios of relevant semileptonic decay to inclusive electron channel are shown in Table 3.1.

semileptonic modes	branching ratio (%)
$D^+(c\bar{d}) \rightarrow K^-\pi^+e^+\nu_e$	4.00 ± 0.10
$D^+(c\bar{d}) \rightarrow \bar{K^0}e^+\nu_e$	8.83 ± 0.22
$D^0(c\bar{u}) \rightarrow K^-e^+\nu_e$	3.55 ± 0.04
$D^0(c\bar{u}) \rightarrow K^*(892)^-e^+\nu_e$	2.16 ± 0.16
$D^0(c\bar{u}) \rightarrow K^-\pi^0e^+\nu_e$	1.6 + 1.3 - 0.5
$D^0(c\bar{u}) \rightarrow \bar{K^0}\pi^-e^+\nu_e$	2.7 + 0.9 - 0.7
$B^+(u\bar{b}) \rightarrow e^+\nu_e X_c$	10.8 ± 0.4

Table 3.1.: Branching ratio of some semileptonic modes [8].

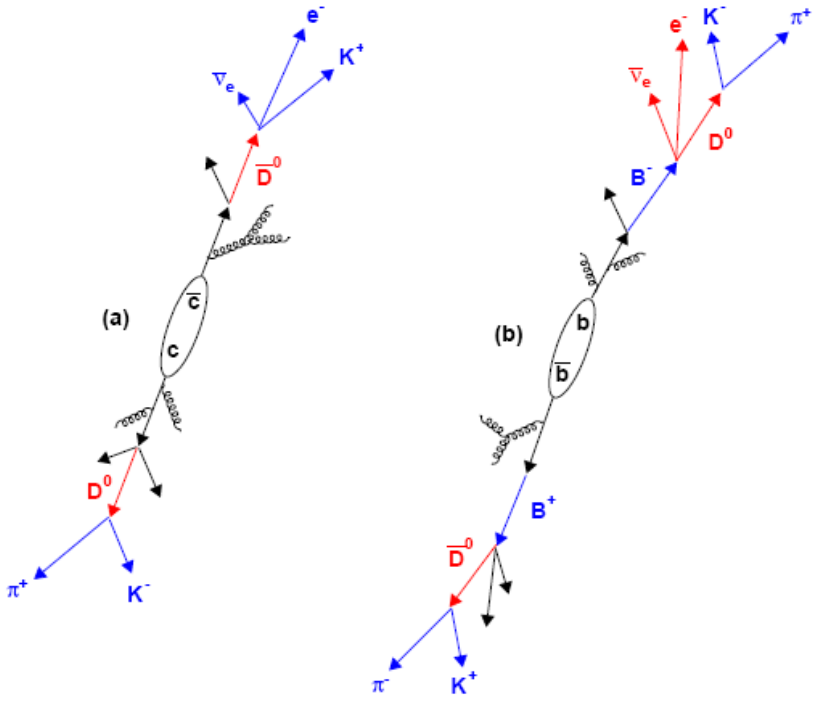

Figure 3.2.: Semileptonic heavy-flavour decays to electrons[38].

3.2. Energy loss of heavy flavours in the QGP

Heavy flavours, charm and beauty, produced in the initial stage of collisions via hard parton scattering processes, propagate through the strongly interacting medium and lose energy via elastic scattering and gluon radiation mechanisms [39, 40, 41, 42, 43, 44, 45, 46, 47, 48, 49, 50, 51].

Figure 3.3 shows the fraction of energy loss of collisional and radiative mechanisms as a function of total momentum for charm and beauty quarks [39]. It was assumed that the thickness of the QGP (L) is equal to 5 fm and the mean free path of the quark (λ) is equal to 1 fm [39]. Elastic elastic scattering is

observed to be dominant at low p_T and radiative scattering is dominant at high p_T [39].

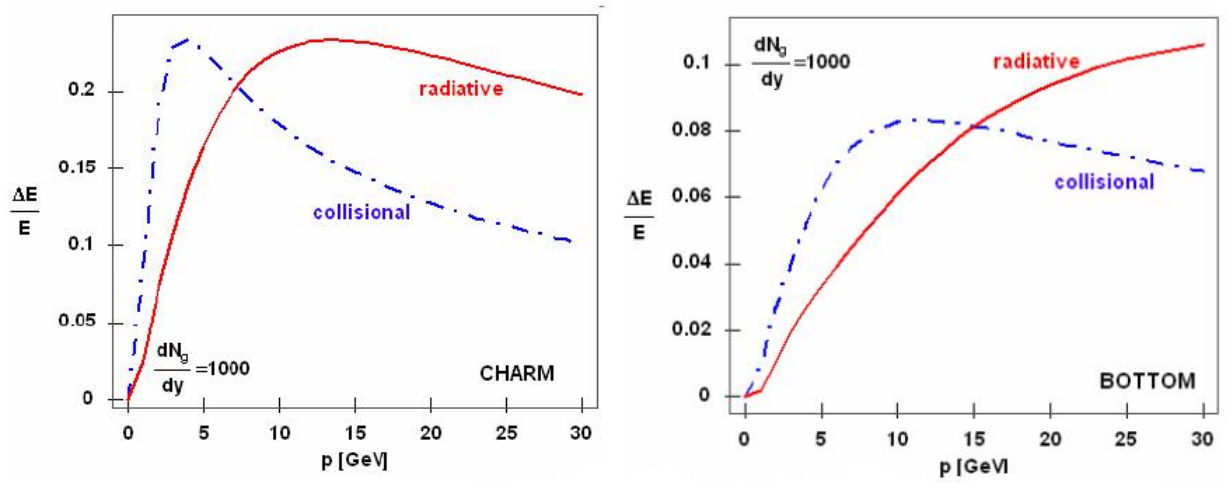

Figure 3.3.: Fraction of energy loss of collisional and radiative mechanisms as a function of total momentum of charm (left panel) and beauty (right panel) quarks. It was assumed L = 5 fm and λ = 1 fm[39].

Figure 3.4 shows the fraction of radiative energy loss of light quark, charm and bottom as a function of total momentum [40]. The dashed line corresponds to energy loss in a static medium, which assumes thickness of the QGP (L) equal to 5 fm in the calculation, and the solid line corresponds to the energy loss in a dynamic medium [40]. A mass ordering is observed in the radiative energy loss results, i.e. the energy loss via radiation of gluons increases when the quark mass decreases [40].

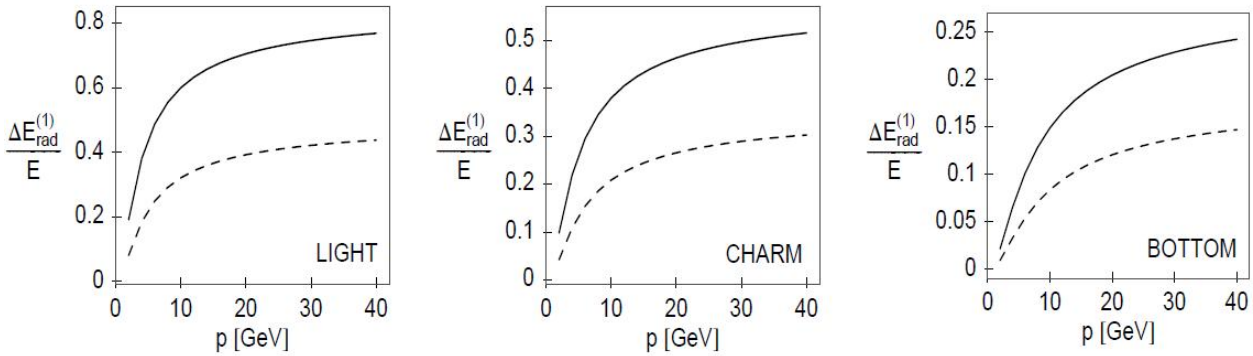

Figure 3.4.: Fraction of radiative energy loss of light quarks, charm and bottom as a function of total momentum. The dashed line corresponds to energy loss in a static medium with L = 5 fm, and the solid line corresponds to the energy loss in a dynamic medium [40].

3.3. Previous measurements

Figure 3.5 shows the electron from beauty decays to electron from heavy-flavour decays (charm and beauty) ratio in pp collisions at mid-rapidity ($|\eta| < 0.7$) at $\sqrt{s}$ = 2.76 TeV meaured with ALICE [52]. It is observed that charm decay contribution is dominant in the measured yield of heavy-flavour decay electrons up to approximately 5 GeV/c [52].

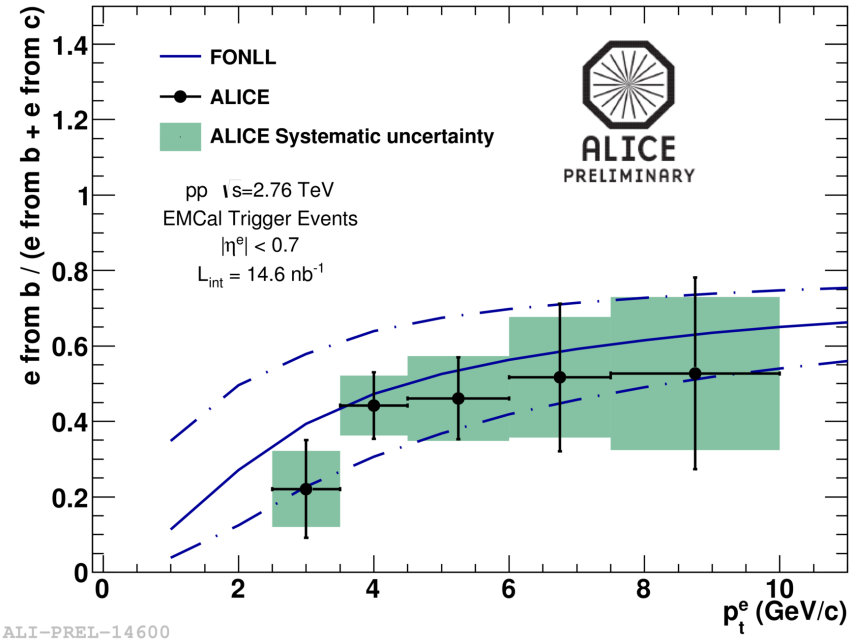

Figure 3.5.: Electron from beauty decays to electron from heavy-flavour decays (charm and beauty) ratio in pp collisions at mid-rapidity ($|\eta| < 0.7$) at $\sqrt{s}$ = 2.76 TeV [52]. Vertical error bars are the statistical uncertainties, horizontal error bars indicate the bin widths, and empty boxes are the total systematic uncertainties.

The modification of the transverse momentum spectra of heavy flavours in heavy-ion collisions with respect to pp collisions (Eq. 2.11) is a sensitive probe of the parton energy loss within the QGP, as discussed in Section 2.2.3.

Figure 3.6 shows the R_{AA} of average D^0, D^+, and D^{*+} mesons in 0-7.5% central Pb-Pb collisions at $\sqrt{s_{\mathrm{NN}}}$ = 2.76 TeV measured with ALICE [30]. The result is compared with R_{AA} of unidentified charged particles and charged pions in 0-10% central in Pb-Pb collisions at $\sqrt{s_{\mathrm{NN}}} = 2.76$ TeV. The prompt D meson suppression is similar to that observed for charged particles with a possible indication of the mass ordering $R^{D}_{\mathrm{AA}} > R^{\text{charg. part.}}_{\mathrm{AA}}$, however it is not conclusive within current uncertainties [30].

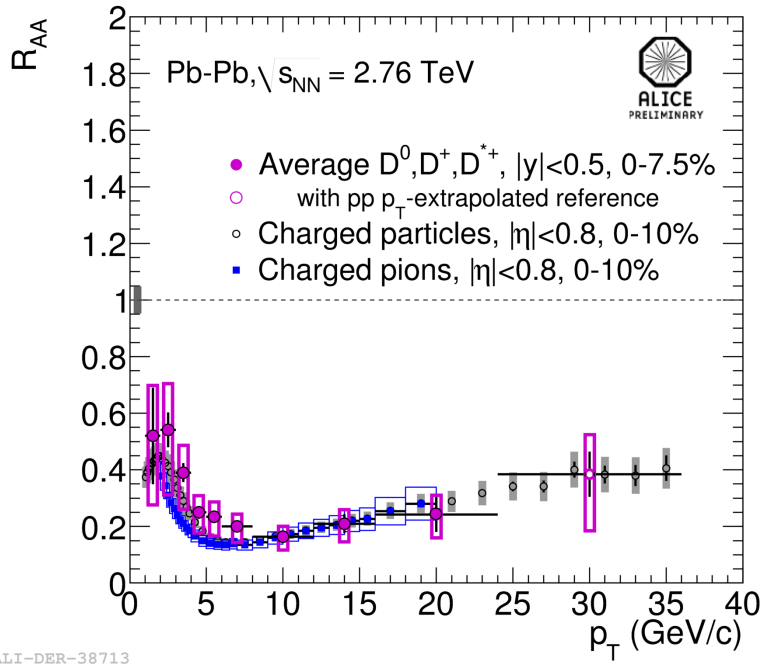

Figure 3.6.: R_{AA} of prompt D mesons, unidentified charged particles and charged pions as a function of p_{T} in central Pb-Pb collisions at $\sqrt{s_{\mathrm{NN}}} = 2.76$ TeV [30]. Vertical error bars are the statistical uncertainties, horizontal error bars indicate the bin widths, and empty boxes are the total systematic uncertainties. The filled box centered at $R_{\mathrm{AA}} = 1$ is the normalization uncertainty.

Figure 3.7 shows the nuclear modification factor of D mesons from charm decays (prompt D mesons) with $6 < p_{\mathrm{T}} < 12$ GeV/c as a function of the number of participant nucleons, which is proportional to the centrality, in $|y| < 0.5$ in Pb-Pb collisions at $\sqrt{s_{\mathrm{NN}}} = 2.76$ TeV measured with ALICE [53]. The result is compared with the nuclear modification factor of J/Ψ from B meson decays (non-prompt J/Ψ) with $p_{\mathrm{T}} > 6.5$ GeV/c in $|y| < 1.2$ in Pb-Pb collisions at $\sqrt{s_{\mathrm{NN}}} = 2.76$ TeV measured with CMS [54, 55]. The larger suppression of prompt D mesons with respect to non-prompt J/Ψ is an indication that charm quarks lose more energy than beauty quarks in the deconfined medium [30].

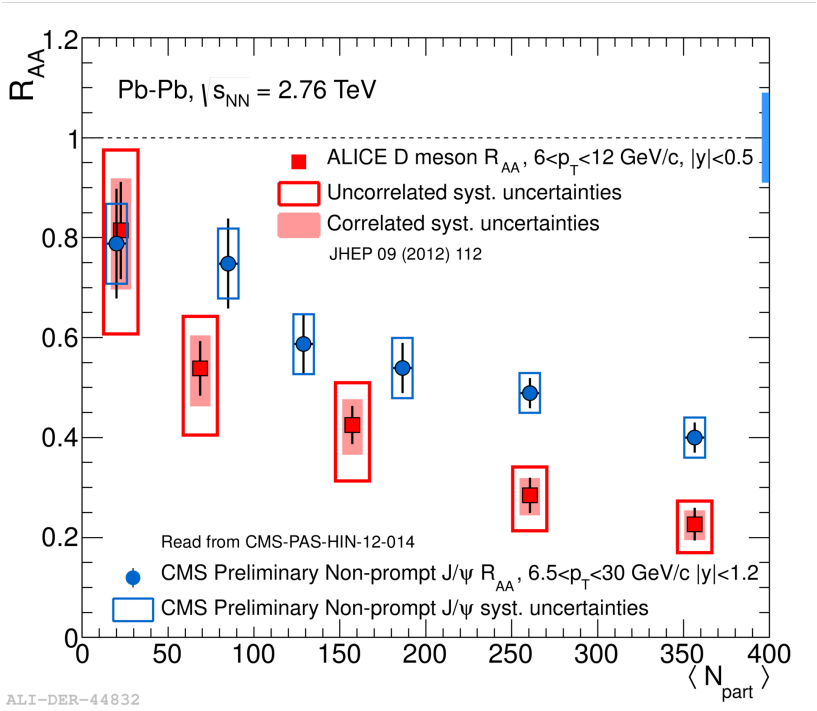

Figure 3.7.: Centrality dependence of R_{AA} of prompt D mesons in $|y| < 0.5$ and $6 < p_{\mathrm{T}} < 12$ GeV/c[53] and non-prompt J/Ψ measured by the CMS Collaboration in $|y| < 1.2$ and $p_{\mathrm{T}} > 6.5$ GeV/c[54, 55] in Pb-Pb collisions at $\sqrt{s_{\mathrm{NN}}} = 2.76$ TeV. Vertical error bars are the statistical uncertainties and boxes are the systematic uncertainties [30].

4

Elliptic azimuthal anisotropy

The measurement of the elliptic azimuthal anisotropy will be discussed in this chapter. The physics of this observable will be discussed in Section 4.1. In Section 4.2, the main methods used to obtain the magnitude of the azimuthal anisotropy will be presented and the contributions of nonflow and flow fluctuations, which are sources of systematic errors in the analysis, will be discussed. The procedure of the measurement of the elliptic azimuthal anisotropy of electrons from heavy-flavour decays will be discussed in Section 4.3 Some previous results will be shown in Section 4.4.

4.1. Physics of the elliptic azimuthal anisotropy

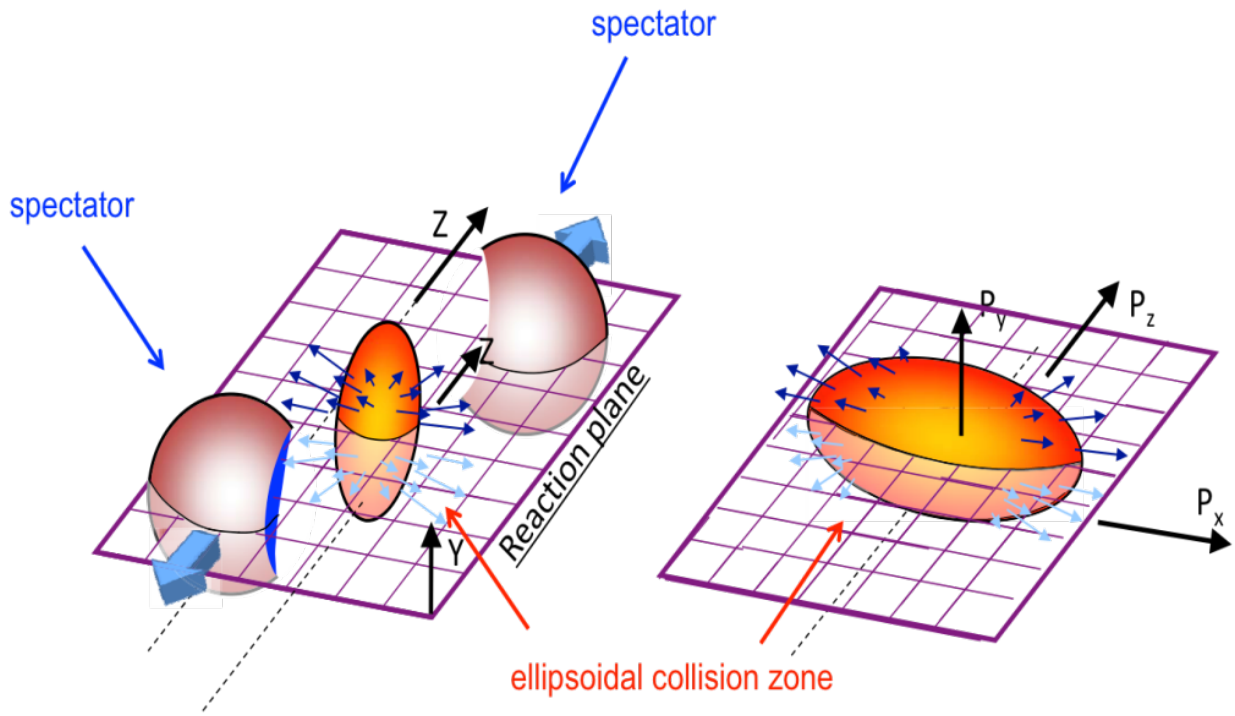

Figure 4.1.: Left panel: ellipsoidal shape of non-central collisions of heavy ions and definition of the reaction plane. Right panel: initial spatial anisotropy of the created particles is converted to momentum space anisotropy due to the pressure gradients created in early stage of non-central collisions of heavy ions [56].

The overlap region of non-central collisions has almost an ellipsoidal shape (see left panel in Fig. 4.1), which results in an initial spatial distribution of the created particles with predominantly the same shape. If the QGP is created after such collisions, the initial spatial anisotropy of the created particles is converted to momentum space anisotropy since the pressure gradient is larger along the impact parameter direction compared to the other directions [19] (see right panel in Fig. 4.1). Once the spatial anisotropy decreases with the expansion of the QGP, the anisotropic flow is sensitive to the particle interactions in early stages of the collision. On the other hand, if the QGP is not created, particles move freely and the momentum space anisotropy of emitted particles can not be observed [19]. Therefore the elliptic azimuthal anisotropy is an evidence of collective motion of particles in non-central collisions of heavy ions at high energy[57, 58, 59, 60, 61, 62, 63].

As illustrated in Fig. 4.1, the path length is smaller in the impact parameter direction compared to the other directions. Therefore the energy loss of quarks that traverse the QGP depends on their directions, which generates an azimuthal anisotropy of the emitted particles. The elliptic azimuthal anisotropy of

particles at high transverse momentum, which are not sensitive to the flow of particles, is interpreted as a path length dependence of quark energy loss within the created dense medium.

The particle azimuthal anisotropy in momentum space is conveniently measured in a coordinate system where the impact parameter is fixed, the so-called *reaction plane*, which is defined by the impact parameter direction and the beam direction, as illustrated in Fig. 4.1. The particle azimuthal distribution measured with respect to the reaction plane can be expressed as a Fourier series [57, 58, 59, 60, 61]:

$$\frac{dN}{d(\varphi - \Psi_{\mathrm{RP}})} = \frac{1}{2\pi}\left\{1 + \sum_{n=1}^{\infty} 2v_n \cos\left[n(\varphi - \Psi_{\mathrm{RP}})\right]\right\}, \tag{4.1}$$

where φ is the azimuthal angle of the emitted particle, Ψ_{RP} is the reaction-plane angle, and $v_n = \langle\cos\left[n(\varphi - \Psi_{\mathrm{RP}})\right]\rangle$ is the azimuthal anisotropy magnitude of the n-th harmonic, as demonstrated in Eq. 4.2 [57, 58, 59, 60, 61]:

$$\begin{aligned}
\langle\cos(n\Delta\varphi)\rangle &= \frac{\int_0^{2\pi}\cos(n\Delta\varphi)\frac{dN}{d\Delta\varphi}d\Delta\varphi}{\int_0^{2\pi}\frac{dN}{d\Delta\varphi}d\Delta\varphi} \\
&= \frac{1}{2\pi}\int_0^{2\pi}\cos(n\Delta\varphi)d\Delta\varphi + \frac{1}{\pi}\int_0^{2\pi}\sum_{m=1}^{\infty} v_m\cos(n\Delta\varphi)\cos(m\Delta\varphi)d\Delta\varphi \\
&= 0 + \frac{v_n}{\pi}\int_0^{2\pi}\cos^2(n\Delta\varphi)d\Delta\varphi \\
&= v_n\,,
\end{aligned} \tag{4.2}$$

where $\Delta\varphi = \varphi - \Psi_{RP}$, and the angle brackets represent the average over the particles of interest in the events in the considered centrality interval. The v_n coefficients depend on the transverse momentum of the particles, pseudorapidity, and centrality of the collision.

The second harmonic v_2 quantifies the elliptic azimuthal anisotropy and can be related to the eccentricity of the collision [61]:

$$v_2 = \left\langle \left(\frac{p_x}{p_T}\right)^2 - \left(\frac{p_y}{p_T}\right)^2 \right\rangle . \tag{4.3}$$

Figure 4.2 shows the harmonic v_2 as a magnitude in the particle azimuthal angle distribution (left panel) and v_2 as an eccentricity in the transverse plane (right panel).

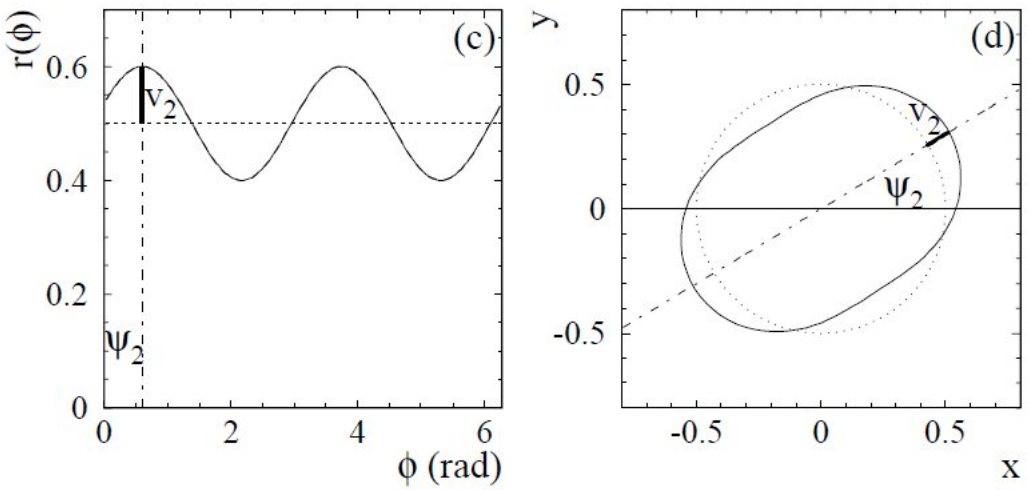

Figure 4.2.: Left panel: v_2 as a magnitude in the particle azimuthal angle distribution. Right panel: v_2 as an eccentricity in the transverse plane [64].

4.2. Experimental methods

Experimentally, several methods are used to obtain the magnitude of the azimuthal anisotropy. In this section, the general concepts of the main methods will be presented as well as their advantages and disadvantages. The concepts will be generalized for all harmonics n, but the elliptic azimuthal anisotropy can be derived from the $n = 2$ change.

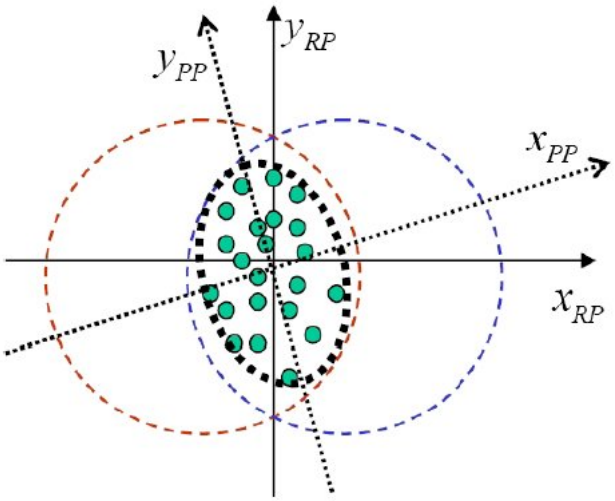

Figure 4.3.: Participant plane (PP) is the deviation from the reaction plane (RP) due to the fluctuations of the participant nucleons in the collision overlap region [65].

The measurement of the harmonics v_n can be affected by *nonflow* contributions, which correspond to

correlations that are not related to the anisotropic flow (jets, resonance decays, momentum conservation, etc), and also *flow fluctuations*, whose main source is the fluctuation of the participant nucleons in the collision overlap region, as illustrated in Fig. 4.3.

The contributions of nonflow and flow fluctuations will be discussed, especially in the event plane method, which is the method used in the analysis. The magnitude of the flow fluctuations (Eq. 4.4 [65]) will be an important parameter for method comparisons in the discussion.

$$\sigma_n^2 \equiv \langle v_n^2 \rangle - \langle v_n \rangle^2 \, . \tag{4.4}$$

4.2.1. Event plane

The reaction plane can not be measured, but the reaction-plane angle can be estimated from the event-plane angle, which is defined as the angle of symmetry of the particle azimuthal distribution in the transverse plane. Therefore it is assumed that the azimuthal distribution of the particles is anisotropic in this method.

The event-plane angle is defined as [61]:

$$\Psi_n = \frac{1}{n} \arctan \frac{Q_{n,y}}{Q_{n,x}} \, , \tag{4.5}$$

where $Q_{n,x}$ and $Q_{n,y}$, defined in Eq. 4.6, are components of an unit vector called Q [61].

$$\begin{aligned} Q_{n,x} &= Q_n \cos(n\Psi_n) \\ Q_{n,y} &= Q_n \sin(n\Psi_n) \, . \end{aligned} \tag{4.6}$$

Experimentally, the components of the Q-vector are obtained by [61]:

$$\begin{aligned} Q_{n,x} &= \sum_i^M \omega_i \cos(n\varphi_i) \\ Q_{n,y} &= \sum_i^M \omega_i \sin(n\varphi_i) \, , \end{aligned} \tag{4.7}$$

where M is the total number of particles used to determine the event plane, φ is the azimuthal angle of

the emitted particles, and ω is the weight of the sum.

Since the number of particles used to determine the event plane affects the event-plane determination, the measured coefficients v_n must be corrected for the event-plane resolution [61]:

$$v_n = \frac{\langle \cos[n(\varphi - \Psi_n)] \rangle}{\langle \cos[n(\Psi_n - \Psi_{\mathrm{RP}})] \rangle} , \tag{4.8}$$

where the angle brackets represent the average, which is done over the particles of interest in the events in the considered centrality interval, the numerator is the v_n obtained with respect to the measured event-plane angle and the denominator is the correction for the event-plane resolution, which is given by (a complete proof can be seen in reference [62]):

$$\langle \cos[n(\Psi_n - \Psi_{RP})] \rangle = \frac{\sqrt{\pi}}{2\sqrt{2}} \chi_n e^{\frac{-\chi_n^2}{4}} \left[I_0\left(\frac{\chi_n^2}{4}\right) + I_1\left(\frac{\chi_n^2}{4}\right) \right] , \tag{4.9}$$

where

$$\chi_n = v_n \sqrt{M} , \tag{4.10}$$

M is the number of particles used to determine the event plane and I is the modified Bessel function.

The *sub-event method*[58] can be used to obtain the correction for the event-plane resolution. In this method, each event plane is divided randomly into two sub-event planes with the same number of particles and event-plane angles are calculated for both sub-events (Ψ_n^A and Ψ_n^B). In absence of fluctuations due to the finite sample of particles used to determine the event-plane angle, the correlation between the event-plane angles of the two sub-events is given by [61]:

$$\langle \cos[n(\Psi_n^A - \Psi_n^B)] \rangle = \langle \cos[n(\Psi_n^A - \Psi_{RP})] \rangle \langle \cos[n(\Psi_n^B - \Psi_{RP})] \rangle . \tag{4.11}$$

If the resolutions of the sub-event planes are the same, they are given by [61]:

$$\langle \cos[n(\Psi_n^A - \Psi_{RP})] \rangle = \langle \cos[n(\Psi_n^B - \Psi_{RP})] \rangle = \sqrt{\langle \cos[n(\Psi_n^A - \Psi_{RP})] \rangle} . \tag{4.12}$$

The χ_n parameter that corresponds to the sub-event is obtained by comparing the equations 4.9 and

4.12. The equation 4.10 is then used to calculate the χ_n parameter of the full event [61]:

$$\chi_n^{event} = \frac{\chi_n^{sub-event}}{\sqrt{2}} \,. \tag{4.13}$$

Finally the calculated χ_n^{event} parameter is used in the equation 4.9 to obtain the event plane resolution of the full event.

Another method used to obtain the correction for the event-plane resolution is the *three event method*[61], which is particularly convenient if the detector used to reconstruct the event plane does not have full acceptance. The correction for the event-plane resolution in this method is obtained by permutation of the event-plane angle with two more event-plane angles (Ψ_n^A and Ψ_n^B) of the same events, but determined from different sample of particles. For instance the three event-plane angles can be reconstructed with detectors at different rapidities. Assuming that the fluctuations due to the determination of the event-plane angle with a finite sample of particles are negligible, the correction for the event plane resolution is given by [61]:

$$\langle \cos[n(\Psi_n - \Psi_{\mathrm{RP}})] \rangle = \sqrt{\frac{\langle cos[n(\Psi_n - \Psi_n^A)] \rangle \langle cos[n(\Psi_n - \Psi_n^B)] \rangle}{\langle cos[n(\Psi_n^A - \Psi_n^B)] \rangle}} \,. \tag{4.14}$$

Contributions of nonflow can be reduced if the event plane and the particles of interest are reconstructed in different rapidities. Another implementation used to reduce the contribution of nonflow is to flatten the event plane if the detector has azimuthal asymmetry.

The elliptic azimuthal anisotropy obtained by the event plane method depends on flow fluctuations in the following way [65]:

$$v_2\{EP\} = \langle v_2^{\alpha} \rangle^{1/\alpha} \,, \tag{4.15}$$

where $\alpha \approx 2$ for small values of resolution and $\alpha \approx 1$ for large values.

4.2.2. Scalar product

In the *scalar product method*, the Q-vector is not an unit vector as in the event plane method and the magnitude of the Q-vector is used as a weight to calculate the v_n coefficients [66]:

$$v_n = \frac{\langle |Q_n| \cos[n(\varphi - \Psi_n)] \rangle}{\langle \cos[n(\Psi_n - \Psi_{\mathrm{RP}})] \rangle} , \tag{4.16}$$

where the denominator represents the correction for the event-plane resolution, which can also be obtained with the sub-event method or the three event plane method.

The elliptic azimuthal anisotropy obtained by the scalar product is given by [65]:

$$v_2\{SP\} = \sqrt{\langle v_2^2 \rangle} . \tag{4.17}$$

When the flow fluctuations are negligible, $\langle v_2^2 \rangle = \langle v_2 \rangle^2$ and the scalar product method is comparable with the event plane method at large values of resolution.

4.2.3. 2- and 4-particle azimuthal correlations

In this method, the Q-vector is conveniently defined as [58]:

$$Q_n = e^{in\varphi} , \tag{4.18}$$

where φ is the azimuthal angle of the particle.

The azimuthal correlation of two particles (a and b) is related to the v_n harmonics as [58, 67]:

$$\begin{aligned} \langle Q_{n,a} Q_{n,b}^* \rangle &= \langle \langle e^{in(\varphi_a - \varphi_b)} \rangle \rangle \\ &= \langle \langle e^{in(\varphi_a - \Psi_{\mathrm{RP}}) - in(\varphi_b - \Psi_{\mathrm{RP}})} \rangle \rangle \\ &= \langle \langle e^{in(\varphi_a - \Psi_{\mathrm{RP}})} \rangle \langle e^{-in(\varphi_b - \Psi_{\mathrm{RP}})} \rangle \rangle \\ &= \langle v_n^2 \rangle , \end{aligned} \tag{4.19}$$

where the two angle brackets represent the average over the particles of interest in the events in the considered centrality interval.

Experimentally the average over the particles can be obtained by [58, 67]:

$$\langle e^{in(\varphi_a-\varphi_b)}\rangle = P_{\langle 2\rangle}\sum_{i,j=1}^{M} e^{in(\varphi_i-\varphi_j)}\ , \tag{4.20}$$

where $i \neq j$ to avoid autocorrelations, and $P_{\langle 2\rangle} = M!/(M-2)!$ is the permutation of the particles.

The average over the events can be obtained by [58, 67]:

$$\langle\langle e^{in(\varphi_a-\varphi_b)}\rangle\rangle = \frac{\sum_{k=1}^{N}(W_{\langle 2\rangle})_k\langle e^{in(\varphi_i-\varphi_j)}\rangle_k}{\sum_{k=1}^{N}(W_{\langle 2\rangle})_k}\ , \tag{4.21}$$

where, in general, the weight is given by $W_{\langle 2\rangle} = M(M-1)$ in order to minimize the effect of multiplicity variation in the measurement.

The azimuthal correlation of four particles (a, b, c, and d) is analogous [58, 67]:

$$\begin{aligned}
\langle Q_{n,a}Q_{n,b}Q^*_{n,c}Q^*_{n,d}\rangle &= \langle\langle e^{in(\varphi_a+\varphi_b-\varphi_c-\varphi_d)}\rangle\rangle \\
&= \langle\langle e^{in(\varphi_a-\Psi_{\mathrm{RP}})+in(\varphi_b-\Psi_{\mathrm{RP}})-in(\varphi_c-\Psi_{\mathrm{RP}})-in(\varphi_d-\Psi_{\mathrm{RP}})}\rangle\rangle \\
&= \langle\langle e^{in(\varphi_a-\Psi_{\mathrm{RP}})}\rangle\langle e^{in(\varphi_b-\Psi_{\mathrm{RP}})}\rangle\langle e^{-in(\varphi_c-\Psi_{\mathrm{RP}})}\rangle\langle e^{-in(\varphi_d-\Psi_{\mathrm{RP}})}\rangle\rangle \\
&= \langle v_n^4\rangle\ .
\end{aligned} \tag{4.22}$$

Experimentally, the average over the particles can be obtained by [58, 67]:

$$\langle e^{in(\varphi_a+\varphi_b-\varphi_c-\varphi_d)}\rangle = P_{\langle 4\rangle}\sum_{i,j,k,l=1}^{M} e^{in(\varphi_a+\varphi_b-\varphi_c-\varphi_d)}\ , \tag{4.23}$$

where $i \neq j \neq k \neq l$ to avoid autocorrelations, and $P_{\langle 4\rangle} = M!/(M-4)!$ is the permutation of the particles.

The average over the events can be obtained by [58, 67]:

$$\langle\langle e^{in(\varphi_a+\varphi_b-\varphi_c-\varphi_d)}\rangle\rangle = \frac{\sum_{k=1}^{N}(W_{\langle 4\rangle})_k\langle e^{in(\varphi_i+\varphi_j-\varphi_k-\varphi_l)}\rangle_k}{\sum_{k=1}^{N}(W_{\langle 4\rangle})_k}\ , \tag{4.24}$$

where the weight is given by $W_{\langle 4\rangle} = M(M-1)(M-2)(M-3)$.

According to Eq. 4.19 and 4.22, the results obtained in 2- and 4-particle azimuthal correlations are, respectively, $\langle v_n^2\rangle$ and $\langle v_n^4\rangle$. However, even in absence of nonflow, the magnitude of the azimuthal anisotropy can not be obtained without bias since $\langle v_n^k\rangle \neq \langle v_n\rangle^k$ due to flow fluctuations [65], as shown in

Eq. 4.4.

4.2.4. Cumulants

The expectation value of the azimuthal correlation of two particles (a and b) statistically dependent is given by [68]:

$$E[e^{in(\varphi_a-\varphi_b)}] = E[e^{in\varphi_a}]E[e^{-in\varphi_b}] + E_c[e^{in(\varphi_a-\varphi_b)}] \,, \tag{4.25}$$

where the last term is called *2-particle cumulant* ($c_n\{2\}$) [67, 68]. Ideally the expectation value is obtained from the probability distribution function, but it can be estimated from the average of random azimuthal correlations of two particles over a large quantity of events [58, 67, 68]:

$$\langle Q_{n,a}Q^*_{n,b}\rangle = \langle Q_{n,a}\rangle\langle Q^*_{n,b}\rangle + c_n\{2\} \,, \tag{4.26}$$

where Q_n is the Q-vector defined in Eq. 4.18. If the detector used to measure the particle azimuthal correlation has uniform acceptance, the terms $\langle Q_{n,a}\rangle$ and $\langle Q^*_{n,b}\rangle$ vanish and the 2-particle cumulant results in:

$$\begin{aligned} c_n\{2\} &= \langle Q_{n,a}Q^*_{n,b}\rangle \\ &= \langle v_n^2\rangle \,. \end{aligned} \tag{4.27}$$

Therefore the v_n obtained with the 2-particle cumulant is given by [58, 67, 68]:

$$v_n\{2\} = \sqrt{c_n\{2\}} = \sqrt{\langle v_n^2\rangle} \,. \tag{4.28}$$

The concept of the 4-particle cumulant is analogous. The expectation value of the azimuthal correlation of four particles (a, b, c, and d) statistically dependent is given by [68]:

$$
\begin{aligned}
E[e^{in(\varphi_a+\varphi_b-\varphi_c-\varphi_d)}] &= E[e^{in(\varphi_a-\varphi_c)}]E[e^{in(\varphi_a-\varphi_d)}] \\
&+ E[e^{in(\varphi_b-\varphi_c)}]E[e^{in(\varphi_b-\varphi_d)}] \\
&+ E_c[e^{in(\varphi_a+\varphi_b-\varphi_c-\varphi_d)}] \,, \qquad (4.29)
\end{aligned}
$$

where the terms that vanish were neglected and the last term is called *4-particle cumulant* ($c_n\{4\}$) [67, 68]. If the expectation value is estimated from measurements of random correlations of four particles in a large quantity of events, the 4-particle cumulant results in [58, 67, 68]:

$$
\begin{aligned}
c_n\{4\} &= \langle Q_{n,a}Q_{n,b}Q^*_{n,c}Q^*_{n,d}\rangle - \langle Q_{n,a}Q^*_{n,c}\rangle\langle Q_{n,a}Q^*_{n,d}\rangle\langle Q_{n,b}Q^*_{n,c}\rangle\langle Q_{n,b}Q^*_{n,d}\rangle \\
&= \langle v_n^4\rangle - 2\langle v_n^2\rangle^2 \,. \qquad (4.30)
\end{aligned}
$$

The v_n obtained with the 4-particle cumulant is given by [58, 67, 68]:

$$
v_n\{4\} = \sqrt[4]{-c_n\{4\}} = \sqrt[4]{2\langle v_n^2\rangle^2 - \langle v_n^4\rangle} \,. \qquad (4.31)
$$

The flow fluctuations of the 2- and 4-particle cumulant methods can be evaluated if the distribution of v_n with respect to flow fluctuations is known. According to Eq. 4.4, Eqs. 4.28 and 4.31 result in Eqs. 4.32 and 4.33, respectively, if the v_n distribution is assumed to be a Gaussian [58]:

$$
v_n\{2\} = \sqrt{\langle v_n\rangle^2 + \sigma_n^2} \approx \langle v_n\rangle + \frac{\sigma_n^2}{2\langle v_n\rangle} \,, \qquad (4.32)
$$

and

$$
v_n\{4\} = \sqrt[4]{\langle v_n\rangle^4 - 2\sigma_n^2\langle v_n\rangle^2 - \sigma_n^4} \approx \langle v_n\rangle - \frac{\sigma_n^2}{2\langle v_n\rangle} \,. \qquad (4.33)
$$

According to Eqs. 4.32 and 4.33, which are also valid for other distributions with $\sigma_n \ll \langle v_n\rangle$, the $\langle v_n\rangle$ ranges from $v_n\{4\}$ to $v_n\{2\}$ if the v_n measurement is affected by flow fluctuations [65].

4.2.5. Fitted q-distribution

In this method, the v_n coefficients are obtained from the length of the reduced Q-vector, which is defined as [65]:

$$q_n = \frac{|Q_n|}{\sqrt{M}} , \tag{4.34}$$

where $|Q_n|$ is the magnitude of the Q-vector defined in Eq. 4.18, and M is the number of particles used to determine the Q-vector. Since the Q-vector grows as $\sqrt{M}$ if the particles are uncorrelated, the term $1/\sqrt{M}$ is used as a normalization constant in order to remove the dependence on multiplicity, and consequently the multiplicity fluctuations [65].

The distribution of the reduced Q-vector magnitude in the limit of $M \gg 1$ can be expressed as [65]:

$$\frac{dN}{dq_n} = \frac{q_n}{\sigma^2_{q_n}} e^{-\frac{v_n^2 M + q_n^2}{2\sigma^2_{q_n}}} I_0\left(\frac{q_n v_n \sqrt{M}}{\sigma^2_{q_n}}\right) , \tag{4.35}$$

where I_0 is the modified Bessel function, and $\sigma^2_{q_n}$ is given by [65]:

$$\sigma^2_{q_n} = \frac{1}{2}\left[1 + M(\delta_n + 2\sigma^2_n)\right] , \tag{4.36}$$

where σ^2_n represents the fluctuation contribution (see Eq. 4.4) and δ_n represents the nonflow contribution.

The v_n coefficients are obtained by fitting the measured q-distribution with Eq. 4.35. However the v_n coefficients can only be obtained in integrated value of p_T and η.

4.2.6. Lee-Yang Zeros

The aim of this method is to find a zero of the generating function related to the Q-vector. In this method, the Q-vector is defined as the projection on to an arbitrary azimuthal angle θ [65, 69]:

$$Q_n^\theta = \sum_{i=1}^{M} \omega_i \cos[n(\varphi_i - \theta)] , \tag{4.37}$$

where φ is the azimuthal angle of the emitted particle, ω is the weight of the sum, and M is number of particles used to calculate the Q-vector.

In practice, the first minimum of the positive variable r of the complex generating function is used

[65, 69]:

$$G_n^{\theta}(ir) = \left| \langle e^{irQ_n^{\theta}} \rangle \right| , \tag{4.38}$$

where the angle brackets represent the average over the events. After finding the first minimum, which is represented by r_0^{θ}, the v_n coefficients are given by [65, 69]:

$$v_n = \frac{\langle V_n^{\theta} \rangle}{M} , \tag{4.39}$$

where the angle brackets represent the average over the azimuthal angles θ, and the V_n^{θ} parameters are given by [65, 69]:

$$V_n^{\theta} = \frac{j_{01}}{r_0^{\theta}} , \tag{4.40}$$

where j_{01} is the first root of the Bessel function J_0.

This method subtracts the nonflow contributions since the correlation involves a large number of particles and nonflow contributions correspond to correlations involving few particles. However this method is difficult to be implemented since two steps over the data are needed in order to obtain the magnitude of the azimuthal anisotropy.

4.3. Elliptic azimuthal anisotropy of electrons from heavy-flavour decays

Experimentally, inclusive electrons are measured, which means electrons from all possible decays. The main components of the inclusive electrons are [70]:

- Heavy-flavour electron decays;
- Photonic electron background, which is composed mainly of photon conversions, Dalitz decays of light neutral mesons (π^0, η, ω, ϕ), and direct photons from hard scattering processes;
- Non-photonic electron background, whose main components are K $\rightarrow e\pi\nu$ decays, dielectron decays of light vector mesons (ρ,ω,ϕ), and heavy quarkonia (J/Ψ, Υ).

The azimuthal distribution of the inclusive electrons can be expressed as a function of the azimuthal distributions of the heavy-flavour electrons and background electrons:

$$\frac{dN^{inc.\ elec.}}{d\Delta\varphi} = \frac{dN^{HF\ elec.}}{d\Delta\varphi} + \frac{dN^{backg.\ elec.}}{d\Delta\varphi} \ , \tag{4.41}$$

$\Delta\varphi = \varphi - \Psi_{RP}$, where φ is the azimuthal angle of the related electrons and Ψ_{RP} is the reaction plane angle.

If one assumes that v_2 is the dominant harmonic in the particle azimuthal distribution, which is valid in non-central collisions, the azimuthal distribution results in:

$$\frac{dN}{d\Delta\varphi} \approx k\left[1 + 2v_2 cos(2\Delta\varphi)\right] \ , \tag{4.42}$$

and, consequently, the elliptic azimuthal anisotropy of electrons from heavy-flavour decays results in [70]:

$$v_2^{HF\ elec.} = \frac{(1+R)v_2^{inc.\ elec.} - v_2^{backg.\ elec.}}{R} \ . \tag{4.43}$$

where R is the heavy-flavour electron to background electron ratio:

$$R = \frac{N^{HF\ elec.}}{N^{backg.\ elec.}} \ . \tag{4.44}$$

4.4. Previous results

Figure 4.4 shows the integrated elliptic azimuthal anisotropy as a function of the center-of-mass energy per colliding nucleon pair. The ALICE result is obtained from a data sample of 20-30% central Pb-Pb collisions at $\sqrt{s_{\rm NN}}$ = 2.76 TeV and the other results are obtained from lower energies at similar centrality classes.

An increase of approximately 30% in the ALICE result is observed with respect to the RHIC measurement in Au-Au collisions at $\sqrt{s_{\rm NN}}$ = 0.2 TeV [71]. The positive elliptic azimuthal anisotropy at very low energies (FOPI) is understood as due to the bounced-off phenomenon, and the negative value at low energies is understood as due to the shadowing by spectator nucleons, which elongates the particle azimuthal distribution in the direction perpendicular to the reaction plane.

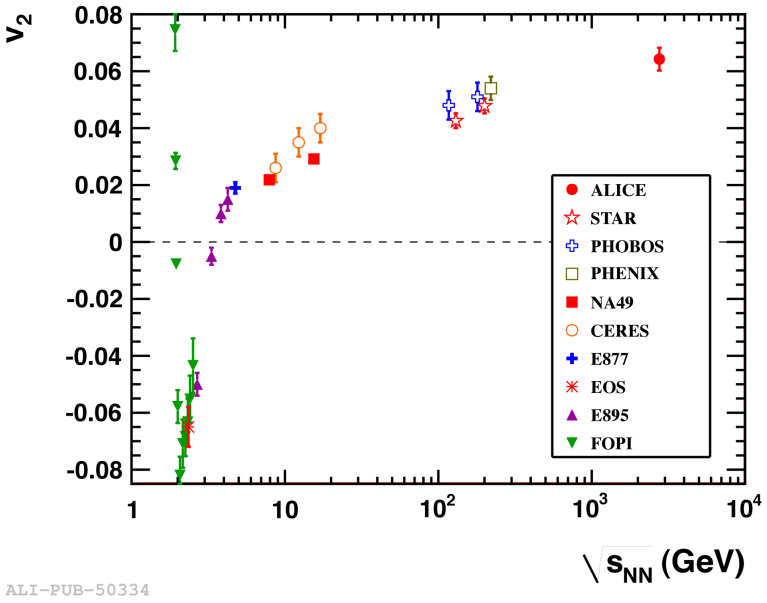

Figure 4.4.: Integrated elliptic azimuthal anisotropy as a function of the center-of-mass energy per colliding nucleon pair [71].

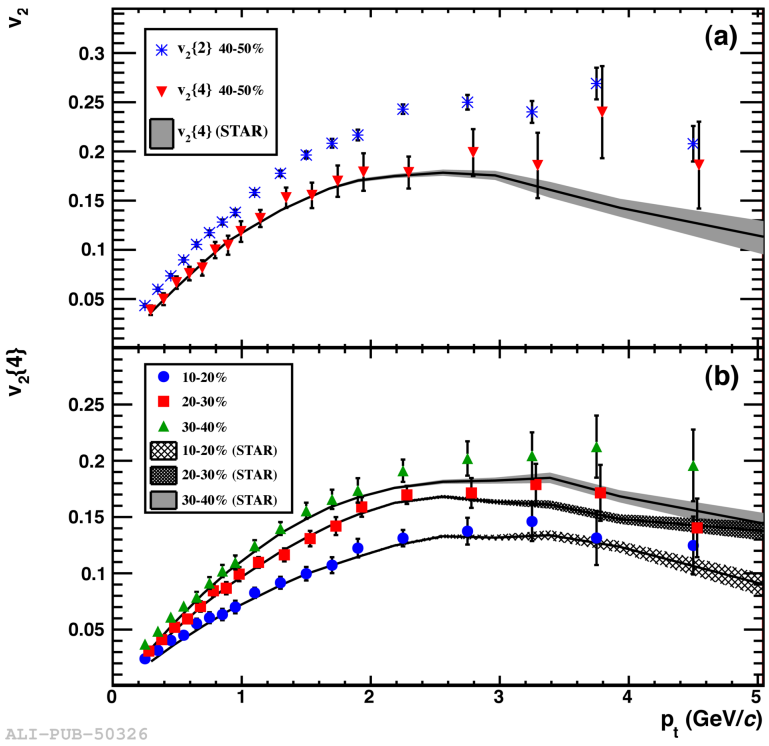

Figure 4.5.: Elliptic azimuthal anisotropy of charged particles as a function of p_T measured in Pb-Pb collisions at $\sqrt{s_{\mathrm{NN}}}$ = 2.76 TeV with ALICE and in Au-Au collisions at $\sqrt{s_{\mathrm{NN}}}$ = 0.2 TeV with STAR. (a) v_2 is obtained with 2- and 4-particle cumulant methods in 40-50% centrality class. (b) v_2 is obtained with 4-particle cumulant method in different centrality classes [71].

Figure 4.5 shows the elliptic azimuthal anisotropy of charged particles measured in Pb-Pb collisions

at $\sqrt{s_{\mathrm{NN}}}$ = 2.76 TeV with ALICE and in Au-Au collisions at $\sqrt{s_{\mathrm{NN}}}$ = 0.2 TeV with STAR [71]. The upper panel shows v_2 as a function of p_T obtained with 2- and 4-particle cumulant methods, $v_2\{2\}$ and $v_2\{4\}$, respectively, in 40-50% centrality class. It is observed that $v_2\{2\}$ is larger than $v_2\{4\}$, which is understood as due to the flow fluctuations, as discussed in Section 4.2.4. The last panel shows v_2 as a function of p_T obtained with 4-particle cumulant method in different centrality classes. It is observed that $v_2\{4\}$ increases with the centrality, which is explained by the increasing of the elliptic anisotropy in peripheral collisions. Results of ALICE and STAR experiments obtained with the same method in the same centrality class are compatible within uncertainties.

Figure 4.6 shows elliptic azimuthal anisotropy of charged particle as a function of pseudorapidity in Au-Au collisions at $\sqrt{s_{\mathrm{NN}}}$ = 130 GeV with PHOBOS. It is observed that v_2 has a maximum value at mid-rapidity ($|\eta| \approx 0$) and decreases at forward rapidity, which corresponds to the fragmentation region.

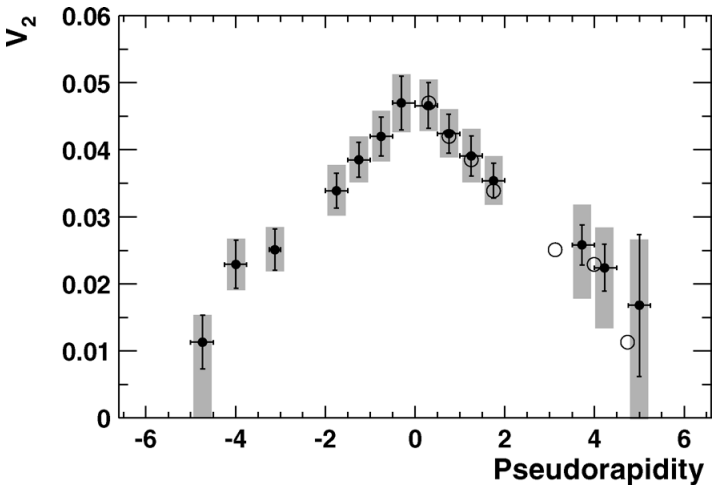

Figure 4.6.: Elliptic azimuthal anisotropy of charged particle as a function of pseudorapidity in Au-Au collisions at $\sqrt{s_{\mathrm{NN}}}$ = 130 GeV with PHOBOS [27].

Figure 4.7 shows v_2/n_q as a function of p_T/n_q, where n_q is the number of constituent quarks of hadrons, in Au-Au collisions at $\sqrt{s_{\mathrm{NN}}}$ = 0.2 TeV. The observed scaling of v_2 with the number of constituent quarks, $v_2^{hadron}/n_q(p_T) = v_2^{quark}(p_T/n_q)$, at low p_T indicates that the anisotropy occurs in the deconfined phase.

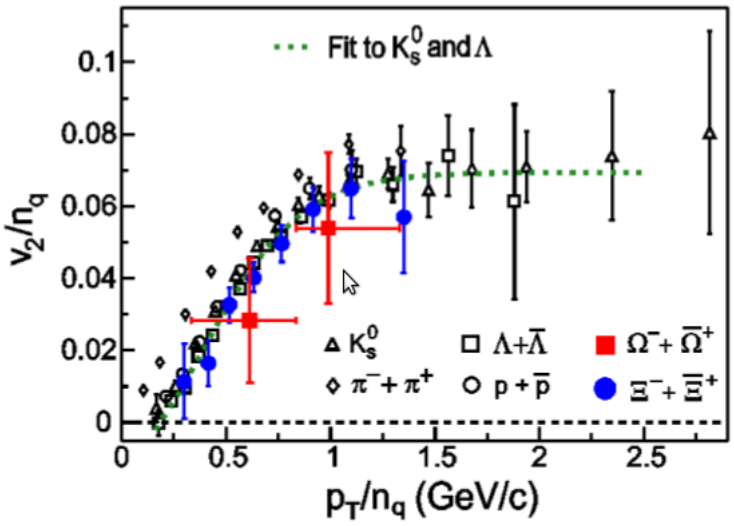

Figure 4.7.: v_2/n_q as a function of p_T/n_q, where n_q is the number of constituent quarks of hadrons, in Au-Au collisions at $\sqrt{s_{NN}}$ = 0.2 TeV [27].

The elliptic azimuthal anisotropy can be connected to the entropy of the medium created in heavy-ion collisions at high energy. Figure 4.8 shows the elliptic azimuthal anisotropy of charged particles as a function of transverse momentum in Au-Au collisions at $\sqrt{s_{NN}}$ = 0.2 TeV. Results represented by square symbols, which have an estimated correction for nonflow and fluctuations effects, are compatible, within uncertainties, with the minimum value of shear viscosity to entropy ratio ($\eta/s = 1/4\pi$).

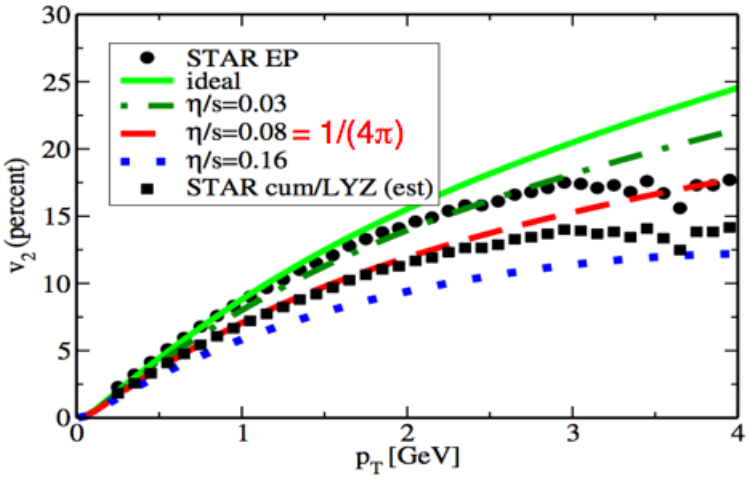

Figure 4.8.: Elliptic azimuthal anisotropy of charged particles as a function of transverse momentum in Au-Au collisions at $\sqrt{s_{NN}}$ = 0.2 TeV. Measurement is compared with viscous hydro calculations [58].

Figure 4.9 shows the elliptic azimuthal anisotropy of the average of D mesons from charm decays, called prompt D mesons, and charged particles as a function of transverse momentum in 30-50% cen-

tral Pb-Pb collisions at $\sqrt{s_{\mathrm{NN}}}$ = 2.76 TeV. Non zero prompt D meson v_2 is observed at low transverse momentum, which indicates collective motion of charm in the medium.

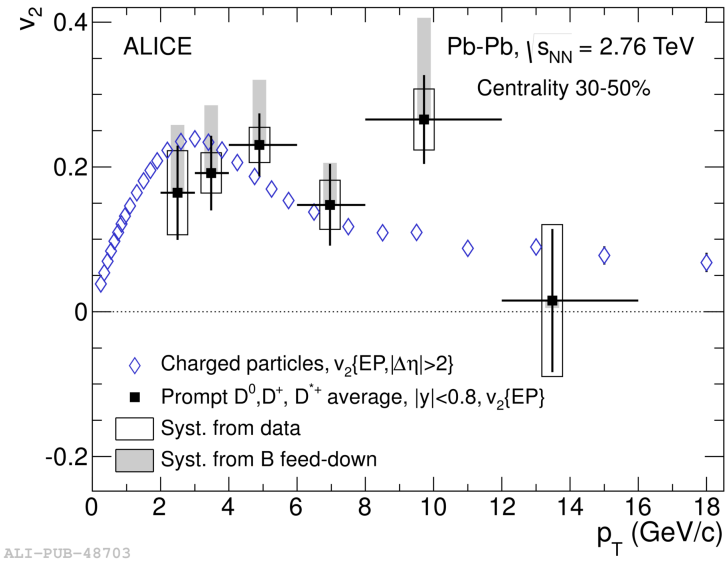

Figure 4.9.: Elliptic azimuthal anisotropy of prompt D meson average and charged particles as a function of transverse momentum in 30-50% central Pb-Pb collisions at $\sqrt{s_{\mathrm{NN}}}$ = 2.76 TeV [72].

5

A Large Ion Collider Experiment

Particles are detected in colliders through their characteristic interactions with the detector material. In order to translate the signals produced by particles in the detector into their observables (momentum, energy, energy loss per path length, spatial coordinates, etc), it is important to understand the detector operation and the interaction of particles with matter.

In this chapter, the main aspects of the experiment will be summarized. The Large Hadron Collider (LHC) will be introduced in Section 5.1 and a general view of the "A Large Ion Collider Experiment" (ALICE) will be presented in Section 5.2, with particular focus on the ALICE sub-systems used in the analysis.

5.1. The Large Hadron Collider (LHC)

The European Organization for Nuclear Research (CERN) includes the Large Hadron Collider (LHC) [73], a hadron accelerator composed of two rings installed in a tunnel with 26.7 Km of circumference.

The LHC was designed to provide collisions of Pb-Pb and p-Pb at $\sqrt{s_{\mathrm{NN}}}$ = 5.5 TeV and pp collisions at $\sqrt{s}$ = 14 TeV. However the LHC operated with half of maximum collision energy in the first years of operation (2010-2013).

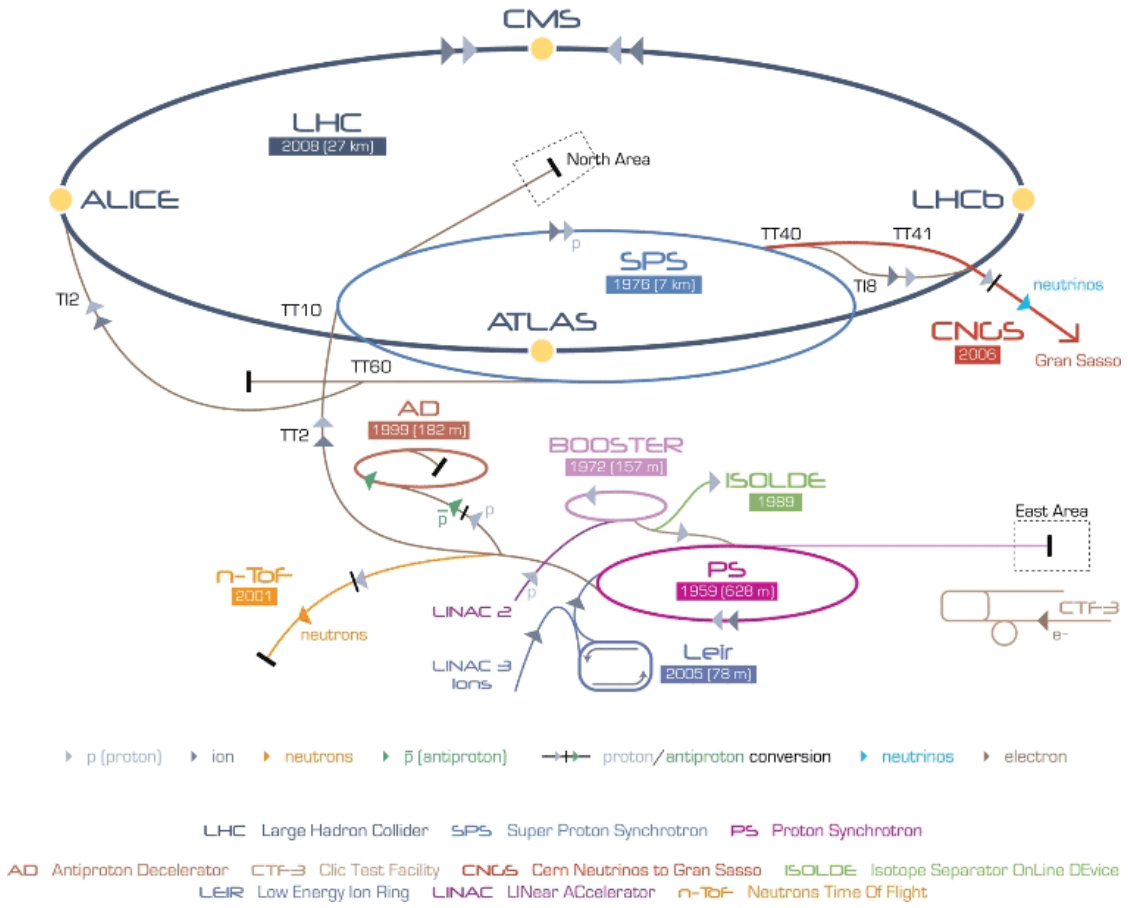

Figure 5.1.: Illustration of the CERN accelerators and LHC detectors [74].

Figure 5.1 shows a scheme of the CERN accelerators and the LHC detectors. Initially the particle beams are accelerated in linear (LINAC) and synchrotron (PSB, PS, and SPS) accelerators and then they are injected into the LHC, where they travel inside beam pipes in opposite directions guided by magnetic fields provided by superconducting electromagnets. The particle beam collisions occur in specific points of the LHC, where the experiments are installed, namely A Large Ion Collider Experiment (ALICE), A Toroidal LHC Apparatus (ATLAS), Compact Muon Solenoid (CMS), and Large Hadron Collider beauty (LHCb).

The ALICE detector [75, 76, 77, 78, 79, 80] is used in this project and it will be discussed in more details in the following sections.

5.2. A Large Ion Collider Experiment (ALICE)

The ALICE [75] is the LHC experiment dedicated to study heavy-ion collisions at high energy. It provides identification of hadrons, leptons, photons, and jets over a wide range of momentum in collisions with high quantity of produced particles. The detector, as illustrated in Fig. 5.2, consists of a central barrel composed of several detectors used to identify charged particles at mid-rapidity (-0.9 $< \eta <$ 0.9). The central barrel is located inside a solenoidal magnet capable to provide up to a 0.5 T magnetic field oriented along the beam direction, which is used to curve charged particle trajectories allowing precise measurement of their momenta.

The ALICE also includes a muon spectrometer (-4.0 $< \eta <$ - 2.5) and several forward detectors for trigger and event characterization purposes.

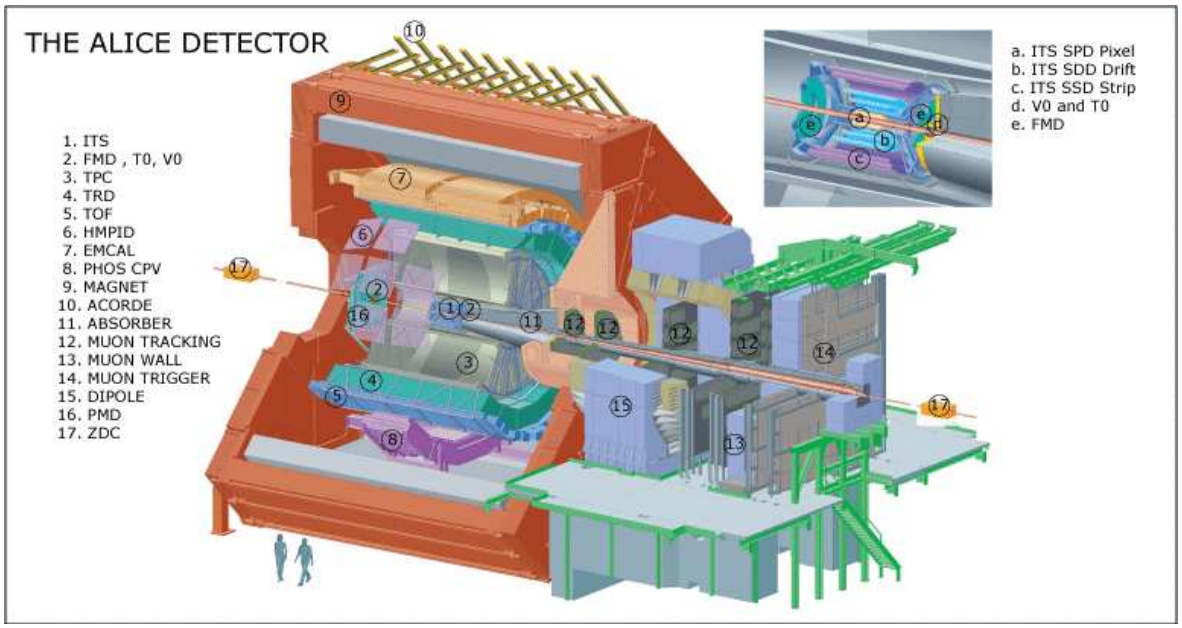

Figure 5.2.: ALICE detector[75].

The central barrel includes the Inner Tracking System (ITS), the Time-Projection Chamber (TPC), the Transition-Radiation Detector (TRD), the Time-of-Flight (TOF) detector, and High-Momentum Particle Identification Detector (HMPID).

The ITS is the closest detector to the interaction point and it is responsible for identifying particles with very low momentum (lower than 100 MeV/c) and measuring the primary vertex. The external detector is the TPC, which is responsible for identifying particles with momentum greater than 100 MeV/c. The ITS and TCP are also used to measure the position of secondary vertex, which is essential

for the impact parameter determination. The TRD is used to identify electrons with momentum greater than 1 GeV/c, the TOF detector is responsible for identifying particles with momentum from 0.2 GeV/c up to 2.5 GeV/c, and the HMPID is used to identify particles with higher momenta.

The T0 detector generates a signal to the TOF detector, which corresponds to the real time of the collision unless a fixed delay. Moreover this detector measures the primary vertex and multiplicity. The V0 detector measures the multiplicity, which is used to obtain the luminosity and centrality in p-Pb and Pb-Pb collisions.

The Photon Spectrometer (PHOS) is responsible for identifying photons. The Zero-Degree Calorimeter (ZDC) is used for event selection and the Electromagnetic Calorimeter (EMCal) is used to measure energy of electrons, photons, neutral hadrons, and jets. The EMCal and ZCD also serve as trigger detectors.

The ALICE detector also includes the Photon Multiplicity Detector (PMD), which is a photon counter, the Forward Multiplicity Detector (FMD), which measures the multiplicity of the particles, and A Cosmic Ray Detector (ACORDE), which measures cosmic ray with energy between 10^{15} and 10^{17} eV.

A full description of the ALICE can be found in the reference [75]. The sub-systems of the ALICE detector used in the analysis will be presented in more details in the following subsections.

5.2.1. Inner Tracking System (ITS)

The Inner Tracking System (ITS) [75, 81, 82], the innermost detector of the ALICE, covers $|\eta| < 0.9$ and full azimuth. The ITS consists of six cylindrical layers of silicon detector grouped in three groups of two layers with different technologies: Silicon Pixel Detector (SPD), Silicon Drift Detector (SDD), and Silicon Strip Detector (SSD). The schematic layout of the ITS layers is shown in Fig. 5.3 and the main characteristics of the detector are presented in Table 5.1.

The charged particles pass through the silicon detector and produce a set of electron-hole pairs along their tracks. The energy loss is related to the number of electron-hole pairs and, since it depends on the mass and momentum of the incident particle, this information is used to identify charged particles [83, 84, 85]. The silicon detector is indicated to be positioned close to the interaction point since the detector has high capability to measure particles at low momentum with fast response.

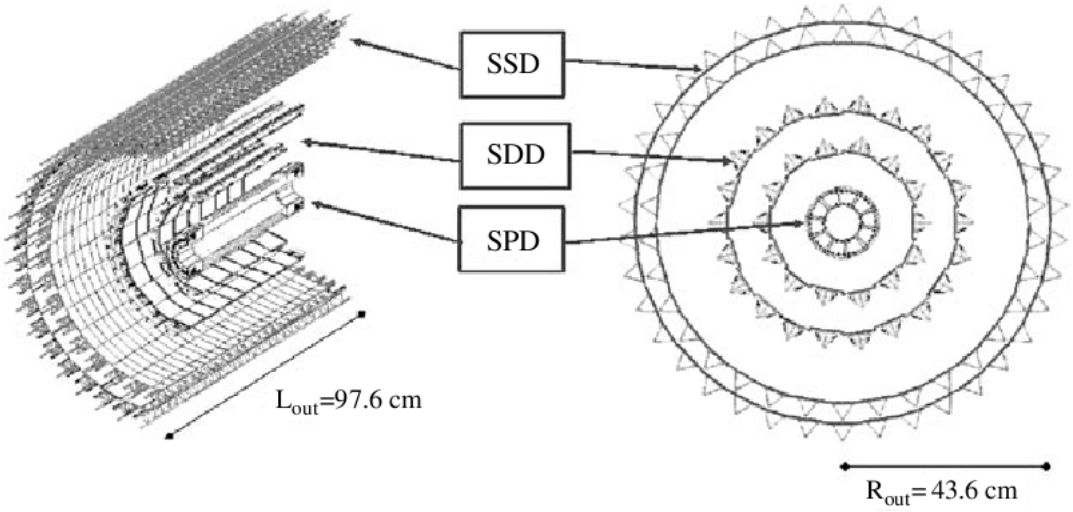

Figure 5.3.: ITS schematic layout[75].

layer	technology	r (cm)	± z (cm)	modules
1	pixel	3.9	14.1	80
2	pixel	7.6	14.1	160
3	drift	15.0	22.2	84
4	drift	23.9	29.7	176
5	strip	38.0	43.1	748
6	strip	43.0	48.9	950

Table 5.1.: Characteristics of the ITS layers [75].

The main tasks of the ITS detector are listed below:

- reconstruction of the primary vertex with high resolution (better than 100 μm);
- reconstruction of secondary vertices from hyperon decays and especially from D and B meson decays;
- identification of particles with very low momentum (lower than 100 MeV/c);
- improvement of the momentum and azimuthal angle resolution due to the high capability of the detector to separate tracks.

5.2.2. Time-Projection Chamber (TPC)

The Time-Projection Chamber (TPC) [75, 86, 87] is the the main tracking detector of the ALICE. The detector consists of two concentric cylinders with radii of, approximately, 85 cm and 2.5 m, and

length along the beam direction of 5.1 m (see schematic layout in Figure 5.4)[75]. Two parallel plates divided in 18 sectors are installed on each side of the detector. The TPC detector covers $|\eta| < 0.9$ and full azimuth.

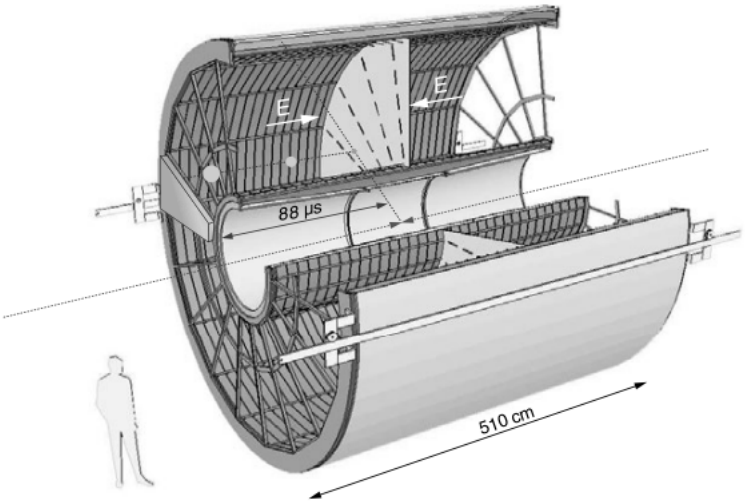

Figure 5.4.: TPC schematic layout[75].

The TPC is a gas detector filled with 90% of Ne and 10% of CO_2. Charged particles passing through the detector ionize the gas and the liberated electrons drift toward the end-plates. The drift time information is used to determine the z coordinate, and the r and φ coordinates are obtained from the position in the end plates.

The energy loss per path length (dE/dx) of the particle in the gas detector, which depends on the mass and momentum of the particle, is used to identify charged particles [83, 84, 85]. More details of the particle identification with the TPC will be presented in Section 6.6.1.

The main tasks of the TPC detector are listed below:

- reconstruction of tracks;
- measurement of momentum;
- identification of charged particles in the transverse momentum range $0.1 < p_T < 100$ GeV/c.

5.2.3. Electromagnetic Calorimeter (EMCal)

The building block of the Electromagnetic Calorimeter (EMCal) [75, 88, 89, 90, 91] is the module, which contains $2 \times 2 = 4$ towers of lead-scintillator layers based on the Shashlik technology[75, 89].

The modules are grouped into full super module, which contains 12 $\times$ 24 = 288 modules and covers $\Delta\eta$ = 0.7 and $\Delta\varphi$ = 20°, or one-third super module, which contains 4 $\times$ 24 = 96 modules and covers $\Delta\eta$ = 0.7 and $\Delta\varphi$ = 7°. Figure 5.5 shows the array of super modules of the EMCal. The total coverage of the detector is $|\eta| < 0.7$ and $80° < \varphi < 180°$.

The measurement principle of the EMCal is the absorption of the particle energy in the lead layer followed by the measurement of the deposited energy with the scintillator layer [83, 84, 85]. The EMCal was designed to absorb the total energy of electrons and the energy information is used to identify them. More details of the electron identification with the EMCal will be presented in Section 6.6.2.

The main tasks of the EMCal are listed below:

- measurement of electrons, photons, neutral hadrons (π^0, η, etc) and jets.
- Level-0 and level-1 trigger [92, 93, 92, 94] in order to enhance events with particles and jets with high energy.

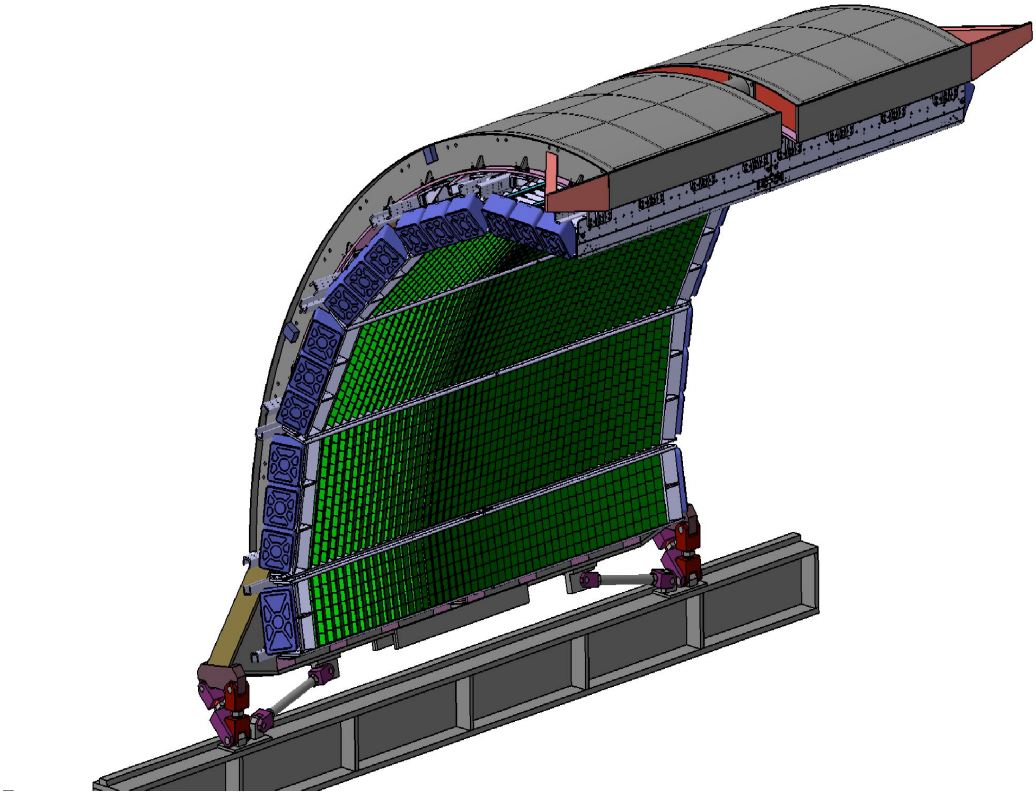

Figure 5.5.: EMCal schematic layout[89].

5.2.4. V0

The V0 detector [75, 95, 96, 97, 98] consists of 2 plastic scintillator counters, called V0A and V0C detectors, positioned on each side of the collision vertex (see schematic layout in Figure 5.6). The V0A detector is positioned on the positive beam direction at a distance of 340 cm from the vertex and the V0C detector is positioned on the opposite side at a distance of 90 cm from the vertex. The two V0 detectors cover full azimuth, but the V0A detector has $2.8 < \eta < 5.1$ pseudorapidity range and the V0C detector has $-3.7 < \eta < -1.7$ pseudorapidity range.

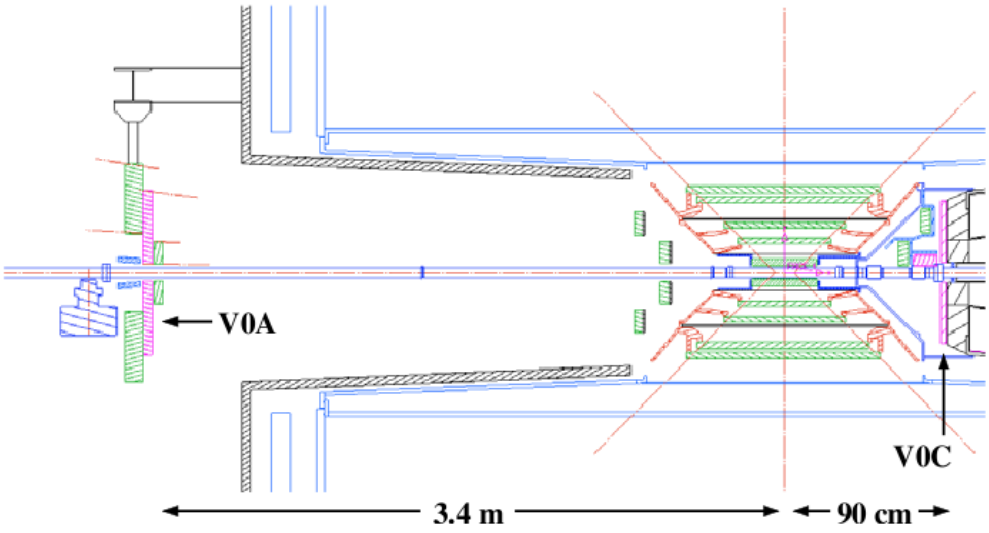

Figure 5.6.: Schematic cross–section of the V0 detector[75].

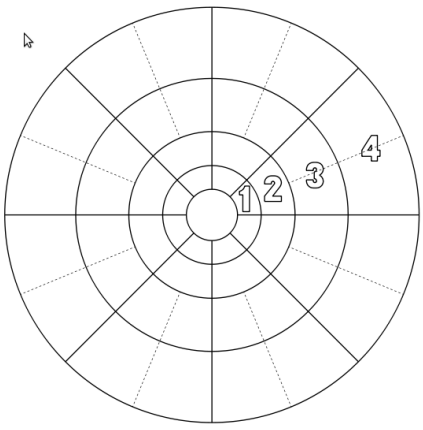

Figure 5.7.: V0 segmentation [75].

The segmentation of the V0A and V0C detectors is shown in Fig. 5.7 and in Table 5.2. Both detectors

are segmented into 4 rings and each ring is divided into 8 sectors, such that each ring covers 0.5-0.6 pseudorapidity range and each sectors covers 45°.

Ring	V0A η_{max}/η_{min}	V0A $\varphi_{min}/\varphi_{max}$	V0C η_{max}/η_{min}	V0C $(\pi-\varphi)_{min}/(\pi-\varphi)_{max}$
1	5.1/4.5	0.7/1.3	-3.7/-3.2	2.8/4.7
2	4.5/3.9	1.3/2.3	-3.2/-2.7	4.7/7.7
3	3.9/3.4	2.3/3.8	-2.7/-2.2	7.7/12.5
4	3.4/2.8	3.8/6.9	-2.2/-1.7	12.5/20.1

Table 5.2.: V0 segmentation [75].

Charged particles pass through the scintillator and deposit their energy in the detector. The light emitted by the scintillator after energy deposition is shifted to lower frequency by wavelength shifting fibers in order improve the detector sensitivity. Finally, the scintillation lights are read out by photomultipliers that produce pulses whose heights are proportional to the energy deposition in each segment of the V0 detector [83, 84, 85].

The main tasks of the V0 detector are listed below:

- measurement of the multiplicity of p-Pb and Pb-Pb collisions, which is needed to extract the centrality and luminosity [99];
- Level-0 minimum-bias trigger for all collisions and level-0 centrality trigger for heavy-ion collisions [100].

6

Data reduction

In this chapter it will be presented how the informations provided with the ALICE sub-systems are used to characterize the collisions and particles in the experiment. The determination of the centrality in heavy-ion collisions with the V0 detector will be presented in Section 6.1. The trigger systems composed by the V0 and EMCal detectors, which are used to enhance events of interest, will be presented in Section 6.2. Section 6.3 is dedicated to explain the determination of the charged particle momentum in the ALICE central barrel. The reconstruction of the charged particle tracks with the ITS and TPC detectors will be presented in Section 6.4 as well as the matching of the reconstructed tracks to the EMCal clusters. The reconstruction of the event-plane angle with the TPC and V0 detectors will be explained in Section 6.5 with particular focus on the flattening procedure used in the event-plane angle determination with the V0 detector. Section 6.6 is dedicated to the electron identification with the TPC and EMCal detectors. Some techniques used for particle identification will be presented in this section.

6.1. Centrality determination

The collision geometry is often used to describe the number of interactions in nucleus-nucleus collisions. When the collision is central, a large number of nucleons participate in the collision and consequently high number of particles are produced. On the other hand, peripheral collisions have a smaller number of participant nucleons and consequently a lower number of produced particles.

The impact parameter, which is defined as the vector between the centers of the collided nuclei, is used to characterize the centrality in nucleus-nucleus collisions. Central collisions have small impact parameter and a large overlap region and peripheral collisions have large impact parameter and small overlap region. The nucleons within the overlap region, see Fig. 6.1, are called *participants* and the nucleons outside the overlap region are called *spectators*.

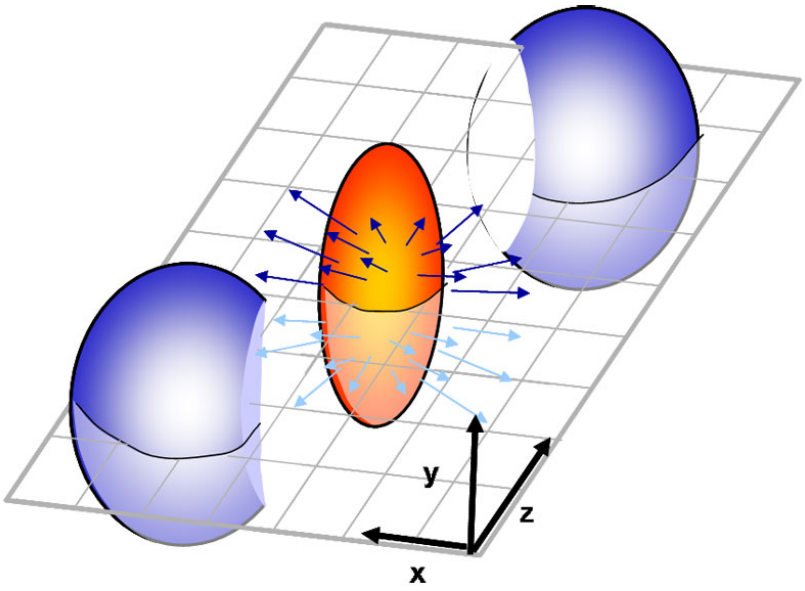

Figure 6.1.: Participant and spectator nucleons in nucleus-nucleus collisions [101].

Experimentally, centrality in heavy-ion collisions is expressed in terms of percentiles of the cross section. By convention, the most central collision has 0% centrality class and the most peripheral collision has 100% centrality class.

The centrality in this analysis is determined by the multiplicity measured with the V0 detector. The distribution of the summed amplitudes in the V0 scintillator tiles (see Fig. 6.2) is parametrized with a Glauber model calculation in order to determine an anchor point at 90% of the total cross section. Then centrality classes are determined as a function of the fitted distribution.

The Glauber model [102] uses geometrical description of nucleus-nucleus collisions to determine the

number of participant nucleons. In this model, the number of collisions is defined as the number of incoherent nucleon-nucleon collisions.

The number of produced particles in each source is described using a negative binomial distribution:

$$P_{\mu,k}(N) = \frac{\Gamma(N+k)}{\Gamma(N+1)\Gamma(k)} \frac{(\mu/k)^N}{(\mu/k+1)^{N+k}}, \tag{6.1}$$

where μ is the mean multiplicity per source and k is related to the multiplicity tail.

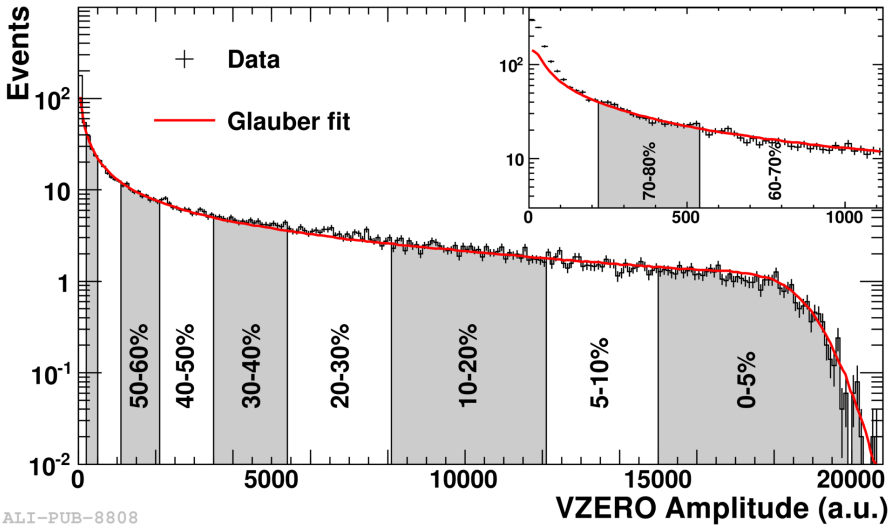

Figure 6.2.: Centrality dependence of the multiplicity density of charged primary particles at central rapidity in Pb-Pb collisions at $\sqrt{s_{NN}}$ = 2.76 TeV measured with ALICE. [103]

6.2. Triggers

Trigger systems are used during the data taking to increase the relevant event rate with respect to the background rate. Two level triggers are used in this analysis:

- Level 0 (L0): event selection is done by hardware
- Level 1 (L1): event selection is done by hardware and software

The triggers used in the analysis are presented in more details in the following subsections.

6.2.1. Minimum-bias trigger

Minimum bias is the trigger without requirement on the final state. The events selected with this trigger are mostly non-diffractive, which is the dominant process in inelastic collisions, and consequently, particles with low transverse momentum and collisions with low multiplicity are dominant.

One of the detectors used to select minimum-bias events at the ALICE experiment is the V0 detector. Events with at least one hit simultaneously measured with the V0A and V0C detectors are defined as minimum bias[95]. Since the V0A and V0C detectors are asymmetrically positioned with respect to the interaction point, a delay is applied to the time measured with the V0C detector.

The interaction between the particle beam and the residual gas in the beam pipe before the collision also produces a signal in the V0 detector, but this signal can be distinguished with the expected time and then rejected in the triggering process. After the time when the bunches cross the interaction point (t_0), the particles coming from the collision will reach the V0C detector at approximately 3 ns and the V0A detector at approximately 11 ns (see Figure 6.3). However particles coming from beam-gas interactions behind the V0C detector will reach the V0C detector about 3 ns before t_0 and the V0A detector about 11 ns after t_0. Likewise particles coming from beam-gas interaction behind the V0A detector will reach the V0A detector about 11 ns before t_0 and the V0C detector about 3 ns after t_0.

In order to reject beam-gas interactions, the trigger is based on logical combinations of the windows: `BBA` = t_0+11 ns, `BBC` = t_0+3 ns, `BGA` = t_0-11 ns, and `BGC` = t_0-3 ns, where A and C are related to the V0A and V0C detectors, respectively, BB means beam-beam interaction and BG means beam–background interaction.

The combination of the channels depends on the experiment and also other detectors can be used to trigger minimum-bias events, but a minimum-bias trigger based only on the V0 detector could be:

`BBA=TRUE` and `BBC=TRUE` and `BGA=FALSE` and `BGC=FALSE` .

In general, the SPD detector [104] is combined with the V0 detector to select minimum-bias events because these detectors are positioned in different acceptances. In this case, the minumum-bias events are the ones with at least one hit simultaneously detected by the V0A and V0C detectors and at least one hit in each SPD layer.

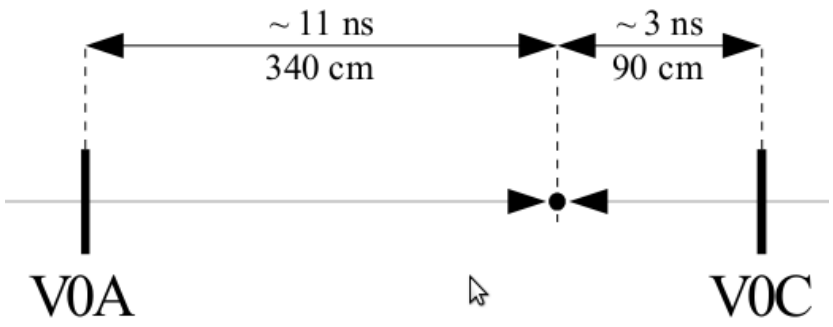

Figure 6.3.: Schematic view of the different arrival time of particles at the V0A and V0C detectors[95].

6.2.2. Centrality trigger

The centrality trigger selects events within a specified centrality class, which is determined by the multiplicity measured with the V0 detector between two thresholds[95, 100]. Currently, there are three centrality triggers at ALICE experiment as shown in Table 6.1.

trigger	centrality range
central	0-10%
semi-central	10-60%
peripheral	60-90%

Table 6.1.: Centrality triggers at ALICE experiment.

Figure 6.4 shows the number of events selected with the semi-central trigger system as a function of centrality. The distribution is obtained from a data sample of Pb-Pb collisions at $\sqrt{s_{NN}}$ = 2.76 TeV collected in 2011.

The semi-central trigger is useful since the rate of events with certain centrality class is increased and, despite of the multiplicity selection, this trigger selects minimum-bias events.

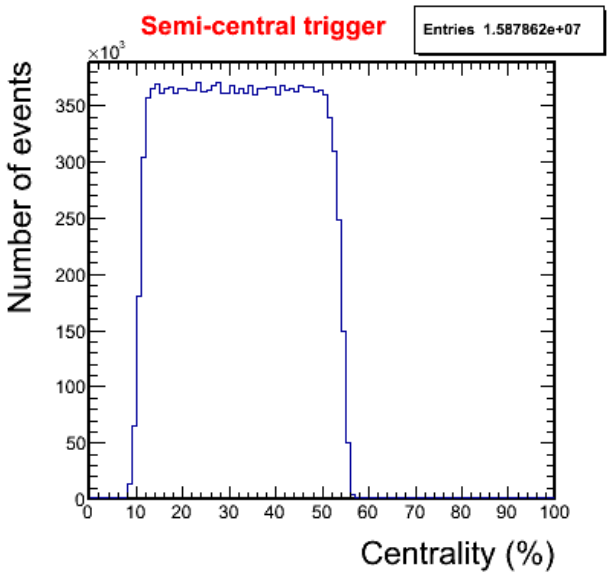

Figure 6.4.: Number of events selected with the semi-central trigger system as a function of centrality.

6.2.3. Single-shower and jet triggers

The L1 single-shower (or photon) and L1 jet trigger systems are performed with the EMCal [92, 93, 92]. The single-shower trigger is designed to enhance events with photons and electrons at high energy, while the jet trigger is designed to enhance events with jets.

The triggering principle consists on selecting events in which the energy summed over a window is greater than a previous determined threshold. The single-shower trigger system uses a sliding time window of 4×4 towers and the jet trigger system uses a window of 16×16 towers, as illustrated in Fig. 6.5.

The trigger systems use centrality information from the V0 detector to apply an online centrality dependent energy threshold, which is computed event-by-event according to the funtion[92]:

$$\text{L1 trigger threshold} = A \times V0_{\text{count}}^2 + B \times V0_{\text{count}} + C \,, \tag{6.2}$$

where $V0_{\text{count}}$ is the total charge provided by the V0 detector and A, B, C are threshold parameters. The centrality dependent threshold is used to uniform the distribution of the number of events as a function of centrality in peripheral centralities, since these EMCal trigger systems with a fixed threshold induce a centrality bias.

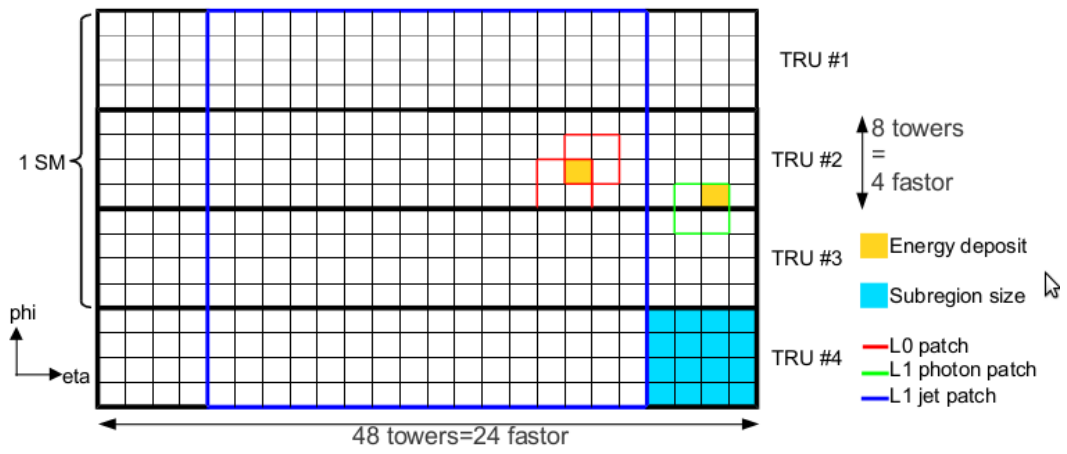

Figure 6.5.: Illustration of the L1 single-shower (photon) and L1 jet trigger windows of the EMCal surface [92].

Figure 6.8 shows the number of events as a function of centrality in events selected with the single-shower and jet trigger systems. The distribution is obtained from a data sample of Pb-Pb collisions at $\sqrt{s_{NN}}$ = 2.76 TeV collected in 2011.

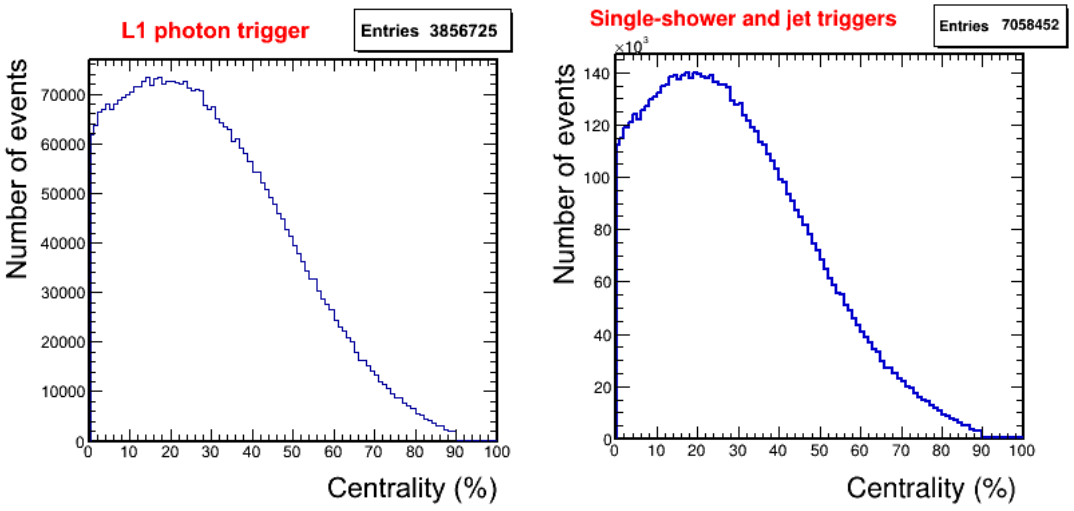

Figure 6.6.: Number of events as a function of centrality in events selected with the single-shower trigger system (left panel), and single-shower and jet trigger systems (right panel).

6.3. Momentum measurement

As discussed in Section 5.2, the central barrel is located inside a 0.5 T magnetic field oriented along the beam direction (z axis). The deflection of the charged particles in the azimuthal plane (xy plane) due

to the magnetic field is used to obtain the momentum of such particles.

In order to obtain the particle momentum, the spatial coordinates of the charged particle track are given with respect to a helix parametrization (see the projections of a helix in the xy and sz planes in Fig. 6.7) [105]:

$$\begin{aligned} x(s) &= x_0 + \frac{1}{k}\left[\cos\left(\Phi_0 + hsk\cos\lambda\right) - \cos\Phi_0\right] \\ y(s) &= y_0 + \frac{1}{k}\left[\sin\left(\Phi_0 + hsk\cos\lambda\right) - \sin\Phi_0\right] \\ z(s) &= x_0 + s\sin\lambda\,, \end{aligned} \tag{6.3}$$

where: s is the path length of the track along the helix and when $s = 0$, which is defined as s_0, the Cartesian coordinates are x_0, y_0, and z_0; $k = 1/R$ is the helix curvature, where R is the radius of curvature; λ is the dip angle; $h = \pm 1$ is the sense of rotation of the helix in the azimuthal plane; $\Phi_0 = \Psi - h\pi/2$ is the azimuthal angle of the s_0 point with respect to the helix axis; and Ψ is the azimuthal angle of the track at the s_0 point.

In the helix parametrization, the components of the momentum of the charged particles in [GeV/c] are given by:

$$\begin{aligned} p_T &= cqB/k \\ p_z &= p_T\tan\lambda \\ p &= \sqrt{p_T^2 + p_z^2}\,, \end{aligned} \tag{6.4}$$

where p_T and p_z are the transverse and longitudinal components of the momentum, respectively, p is the total momentum, B is the magnetic field in [T], c is the speed of light in [m/ns], and q is the charge of the particle.

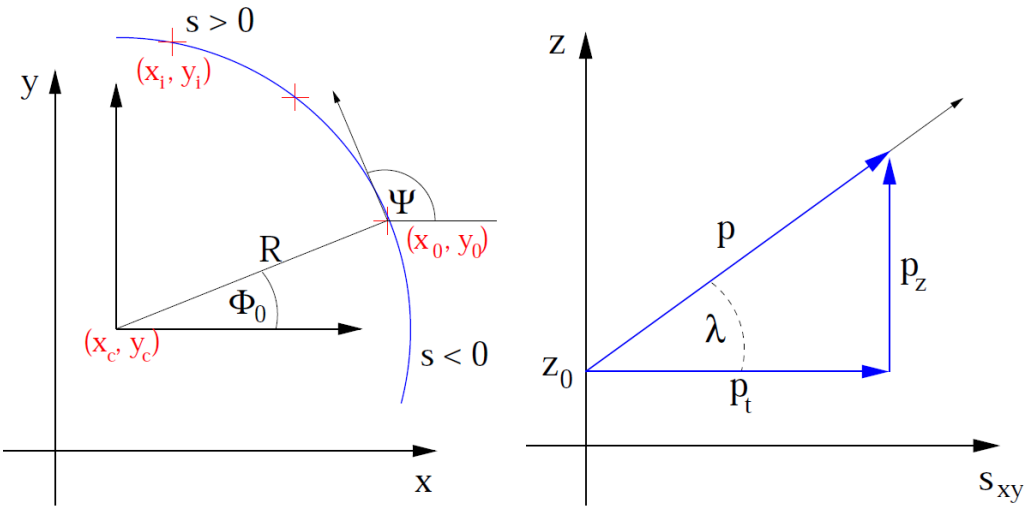

Figure 6.7.: Projections of a helix on the *xy* (left panel) and *sz* (right panel) planes [105].

6.4. Track reconstruction and EMCal cluster matching

When charged particle passes through the tracking detector, a set of adjacent digits, called cluster, is hit and all clusters generated by the same particle form the particle track in the detector.

The track reconstruction is performed with the ITS and TPC detectors and it is based on Kalman filter algorithm[75]. First the primary vertex is measured with the SPD detector and this information is used as seed in the track finding. Since the density of tracks decreases with the radial coordinate, the track reconstruction starts from the outer radius of the TPC detector toward the inner radius of the TPC. Then the track is propagated to the ITS detector toward the innermost layer as close as possible to the the primary vertex.

In addition, the track reconstruction starts from the ITS toward to the TPC and the reconstructed tracks are refitted again toward the ITS. The primary vertex is recalculated with track information in order to improve the resolution.

Figure 6.8 shows the reconstructed tracks with the ITS and TPC detectors. The tracks in white are reconstructed with the ITS detector and the tracks in red are reconstructed with the TPC detector. The result is obtained from a data sample of Pb-Pb collisions at $\sqrt{s_{NN}}$ = 2.76 TeV collected in 2011.

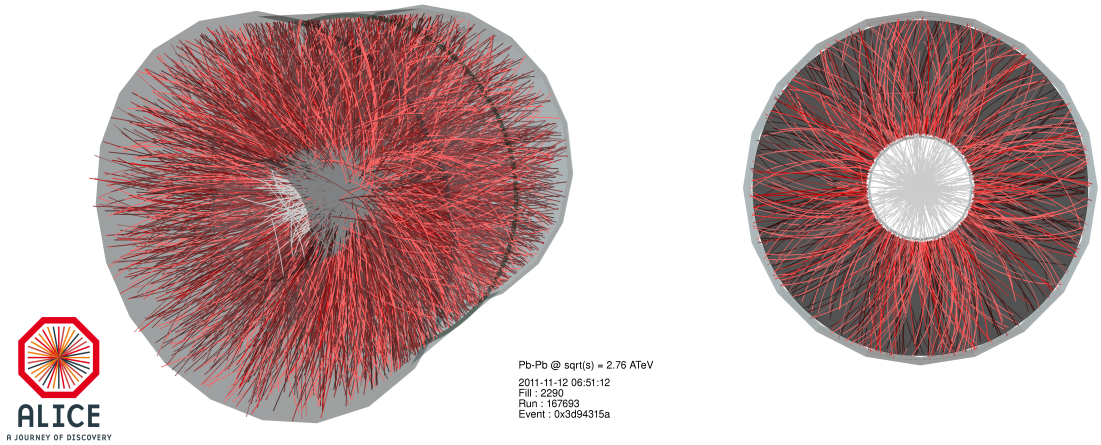

Figure 6.8.: Tracks in the ITS (white lines) and TPC (red lines) obtained in a sample of Pb-Pb collisions at $\sqrt{s_{NN}}$ = 2.76 TeV collected in 2011.

Finally the reconstructed track is extrapolated to the EMCal surface based on informations from the helix parametrization of the tracks. Then the extrapolated track is matched to the closest EMCal cluster based on cuts on the distances in the $\eta\varphi$ plane of the EMCal surface: $\Delta\eta = |\eta^{\text{cluster}} - \eta^{\text{track}}| < 0.025$ and $\Delta\varphi = |\varphi^{\text{cluster}} - \varphi^{\text{track}}| < 0.05$.

6.5. Event-plane angle determination

The event-plane angles (see Eq. 4.5) can be determined using the sum over the azimuthal angles of tracks reconstructed with the TPC or using the sum over the segments of the detectors with azimuthal segmentation (V0, FMD, ZDC, and PMD detectors).

The event-plane angles determined with the TPC and V0 detectors, which are used in the analysis, are presented in more details in the following subsections.

6.5.1. Determination with the TPC detector

In order to obtain the event-plane angle, the Q vector (see Eq. 4.7) is determined with the azimuthal angle of the tracks reconstructed with the TPC detector. Selection criteria of tracks and events are used to improve the quality of the event-plane angle determination. Only events with at least 4 accepted tracks at the TPC pseudorapidity coverage ($|\eta| < 0.8$) are used to determine the event-plane angle. Moreover

only tracks that passed the following requirements are accepted to determine the event-plane angle:

- at least 50 TPC clusters (the maximum value is 160);
- χ^2 to TPC cluster ratio lower than 4;
- distance of the closest approach to the primary vertex lower than 3.2 cm in the z direction and 2.4 cm in the xy plane;
- transverse momentum from 0.15 GeV/c up to 4 GeV/c.

Electron candidates identified with the $70 < dE/dx\ (a.u.) < 90$ requirement are removed from the event-plane angle determination to avoid autocorrelation (the identification strategy will be presented in more details in Section 6.6).

The standard p_T weight is used to improve the event-plane angle resolution. Since the resolution is proportional to v_n (see Equations 4.9 and 4.10) and v_2 is proportional to p_T at low p_T, the used weight has a p_T dependence:

$$\omega_{p_T} = \begin{cases} p_T & \text{if } p_T < 2 \text{ GeV/c} \\ 2 & \text{if } p_T \geq 2 \text{ GeV/c} . \end{cases} \tag{6.5}$$

In addition, the φ weight is used to correct possible non-uniformity of the particle azimuthal angle distribution caused by dead zones in the TPC detector. The used φ weight is given by:

$$\omega_\varphi = \frac{\langle N_\varphi \rangle}{N_\varphi} , \tag{6.6}$$

where $\langle N_\varphi \rangle$ is the average number of particles per φ bin in the particle azimuthal angle distribution and N_φ is the number of the particles in the considered φ bin.

The total weight is given by:

$$\omega(p_T, \varphi) = \omega_{p_T}(p_T)\, \omega_\varphi(\varphi) . \tag{6.7}$$

Finally, the event-plane angle (see Eq. 4.5) is determined with the measured components of the Q vector.

Figure 6.9 shows the angle of the event plane reconstructed with the TPC detector as a function of the centrality in Pb-Pb collisions at $\sqrt{s_{NN}}$ = 2.76 TeV. The azimuthal angle distribution of the event

planes determined in events selected with the semi-central trigger system is uniform in, approximately, 12-52% centrality class. However the azimuthal angle distribution of the event planes determined in events selected with the EMCal trigger system is biased. The non-uniformity of the event-plane angle distribution will be discussed in Section 7.4.

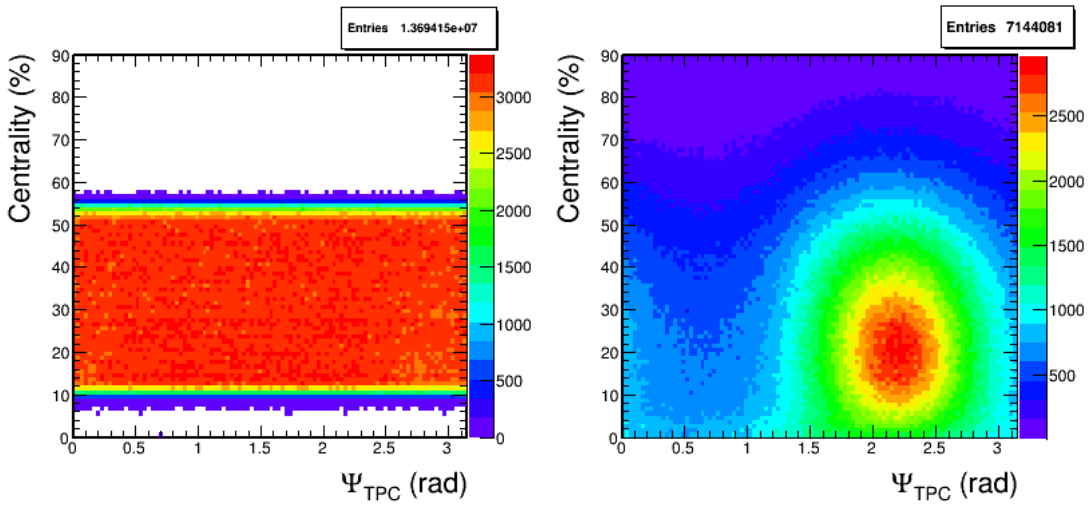

Figure 6.9.: Angle of the event plane reconstructed with the TPC detector as a function of the centrality in Pb-Pb collisions at $\sqrt{s_{NN}}$ = 2.76 TeV. Left panel: events selected with the semi-central trigger. Right panel: events selected with the single-shower and jet trigger systems.

6.5.2. Determination with the V0 detector

The emission of particles with high momenta in heavy-ion collisions at high energy is larger toward the in-plane direction due to the pressure gradient created in early stage of collisions. Therefore the energy deposition is increased in the segments of the V0 detector aligned with the reaction plane. In order to calculate the Q vector (see Eq. 4.7), the weight is given by the cell multiplicity and φ is obtained by the azimuthal angle of the cell, which is identified by the following equation:

$$\varphi = \frac{\pi}{4}\left(\frac{1}{2} + \text{cell}_{\text{ID}}\%8\right) , \tag{6.8}$$

where $\text{cell}_{\text{ID}} = 1, \ldots, 32$ is the cell index and % represents the reminder after division.

The event-plane angle (see Eq. 4.5) is determined with the measured components of the Q vector. However the distribution of the event-plane angle must be flattened due to the non-uniform acceptance of the V0 detector.

The first step of the flattening is the *multiplicity equalization* in each channel of the V0 detector. This

procedure is important since the weight used in the Q-vector measurement is given by the cell multiplicity and non-uniformity in the cell multiplicity distribution can bias the event-plane angle determination.

The second step is the *re-centering* of the Q-vector components, which should be centered at zero in absence of detector acceptance effects. In this procedure, the distributions of the Q_x and Q_y components are parametrized with a Gaussian function in order to obtain the mean and width of the distributions. Then the components of the Q vector in all events are re-centered [66]:

$$Q_x = \frac{Q_x - \langle Q_x \rangle}{\sigma_{Q_x}} , \tag{6.9}$$

and

$$Q_y = \frac{Q_y - \langle Q_y \rangle}{\sigma_{Q_y}} , \tag{6.10}$$

where the angle brackets indicate the average over all events, and σ_{Q_x} and σ_{Q_x} are the widths of the Q_x and Q_y distributions, respectively.

The following correction based on cumulants is also applied to the Q-vector components [66]:

$$Q_{x,n} = \langle Q_{x,n} \rangle + A^{+} \left[\cos(n\Psi_n) + \Delta^{+} \sin(n\Psi_n) \right] , \tag{6.11}$$

and

$$Q_{y,n} = \langle Q_{y,n} \rangle + A^{-} \left[\cos(n\Psi_n) + \Delta^{-} \sin(n\Psi_n) \right] , \tag{6.12}$$

where $A^{\pm}$ and $\Delta^{\pm}$ are extracted with the $\langle Q^2_{x,n} \rangle$, $\langle Q^2_{y,n} \rangle$ and $\langle Q_{x,n} Q_{x,n} \rangle$ measurements.

Finally the *Fourier flattening technique* [106] is used to correct the event-plane angle for the remaining non-flatness caused by the detector acceptance effects. The correction is given by [106]:

$$\Psi_n = \Psi_n^{\mathrm{corr}} + \Delta\Psi_n , \tag{6.13}$$

where Ψ_n^{corr} is the corrected event-plane angle, and $\Delta\Psi_n$ is given by [106]:

$$\Delta\Psi_n = \sum_{k=1}^{k_{max}} \left[A_k \cos(nk\Psi_n^{\mathrm{corr}}) + B_k \sin(nk\Psi_n^{\mathrm{corr}}) \right] , \tag{6.14}$$

where A_k and B_k coefficients, given by Eqs. 6.15 and 6.16, respectively, are obtained with the re-

quirement $\langle \cos(nk\Psi_n) \rangle = 0$ and $\langle \sin(nk\Psi_n) \rangle = 0$, which assumes the uniformity of the event plane distribution.

$$A_k = -\frac{2}{k} \langle \sin(nk\Psi_n^{\text{corr}}) \rangle \ , \tag{6.15}$$

and

$$B_k = \frac{2}{k} \langle \cos(nk\Psi_n^{\text{corr}}) \rangle \ . \tag{6.16}$$

The components of the Q vector reconstructed with the V0 detector is then corrected up to 4-th Fourier momentum (k_{max}=4).

Figures 6.10 and 6.11 show the angle of the event planes reconstructed with the V0A and V0C detectors, respectively, as a function of the centrality in Pb-Pb collisions at $\sqrt{s_{NN}}$ = 2.76 TeV. The azimuthal angle distribution of the event planes determined in events selected with the semi-central trigger system is uniform in, approximately, 12-52% centrality class. However the azimuthal angle distribution of the event planes determined in events selected with the EMCal trigger system is biased. The non-uniformity of the event-plane angle distribution will be discussed in Section 7.4.

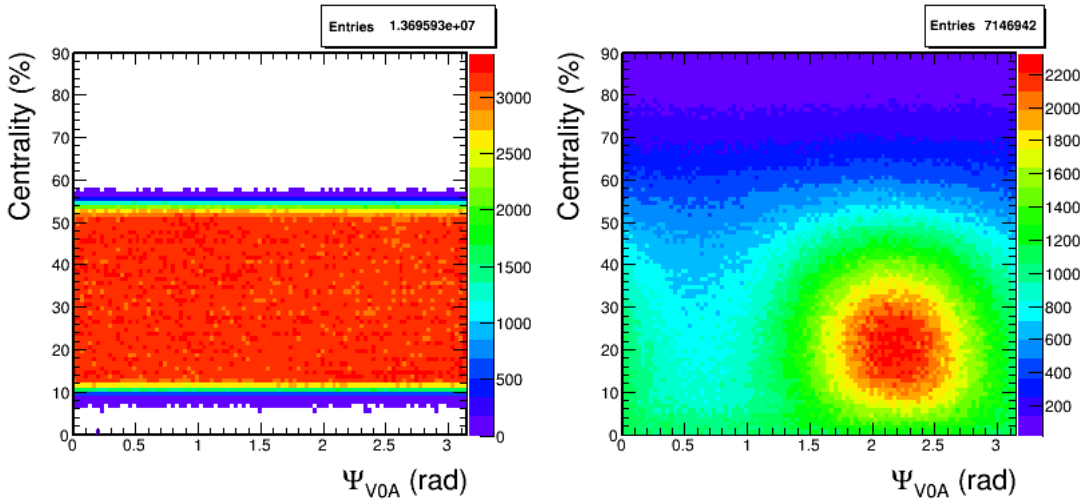

Figure 6.10.: Angle of the event plane reconstructed with the V0A detector as a function of the centrality in Pb-Pb collisions at $\sqrt{s_{NN}}$ = 2.76 TeV. Left panel: events selected with the semi-central trigger. Right panel: events selected with the single-shower and jet trigger systems.

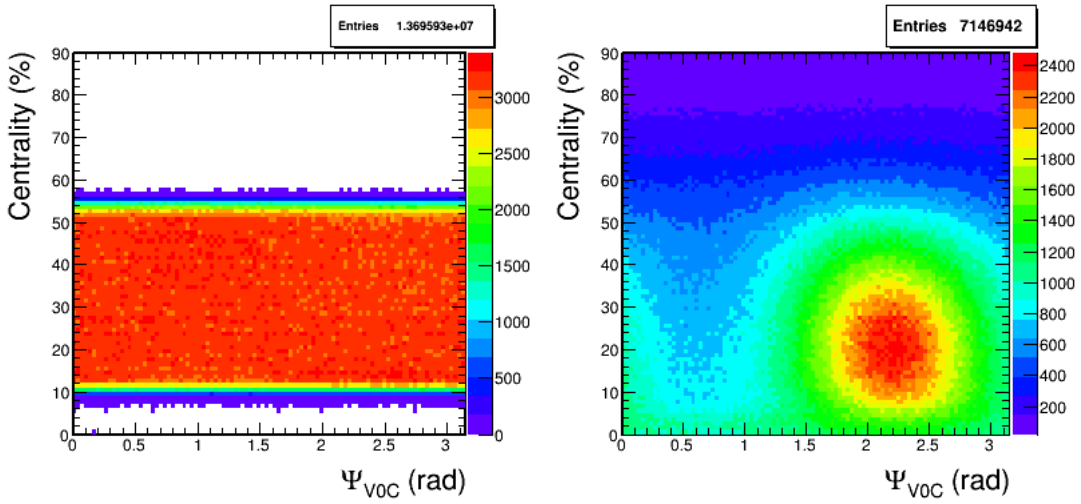

Figure 6.11.: Angle of the event plane reconstructed with the V0C detector as a function of the centrality in Pb-Pb collisions at $\sqrt{s_{NN}}$ = 2.76 TeV. Left panel: events selected with the semi-central trigger. Right panel: events selected with the single-shower and jet trigger systems.

Figures 6.12 and 6.13 show the distributions of the event-plane angle reconstructed with the V0A detector in events selected with the semi-central and EMCal triggers respectively. The results are obtained from a data sample of 20-40% and 30-50% central Pb-Pb collisions at $\sqrt{s_{NN}}$ = 2.76 TeV.

The non-uniformity of the event plane distributions measured in events selected with the EMCal trigger systems will be discussed in details in Section 7.4.

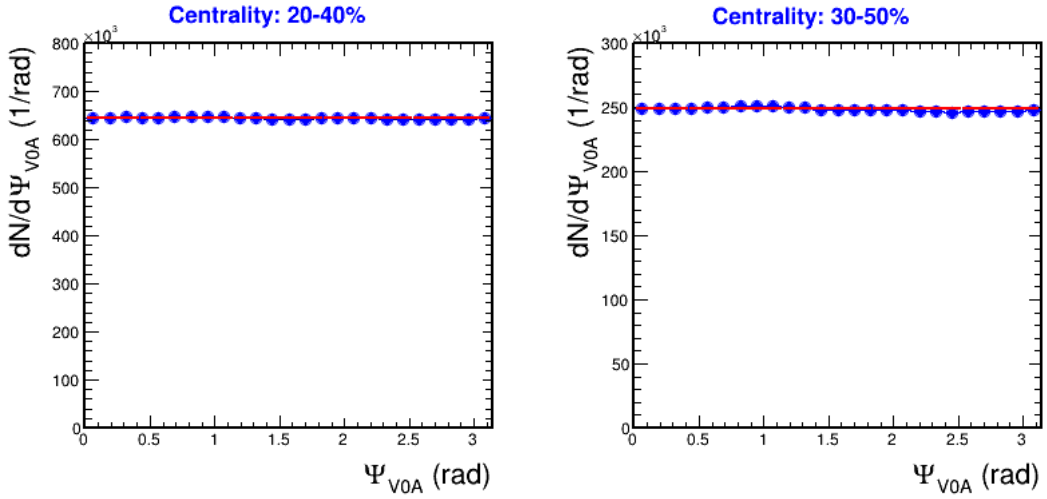

Figure 6.12.: Distribution of the angle of the event plane reconstructed with the V0A detector in 20-40% and 30-50% central Pb-Pb collisions at $\sqrt{s_{NN}}$ = 2.76 TeV. Events are selected with the semi-central trigger system.

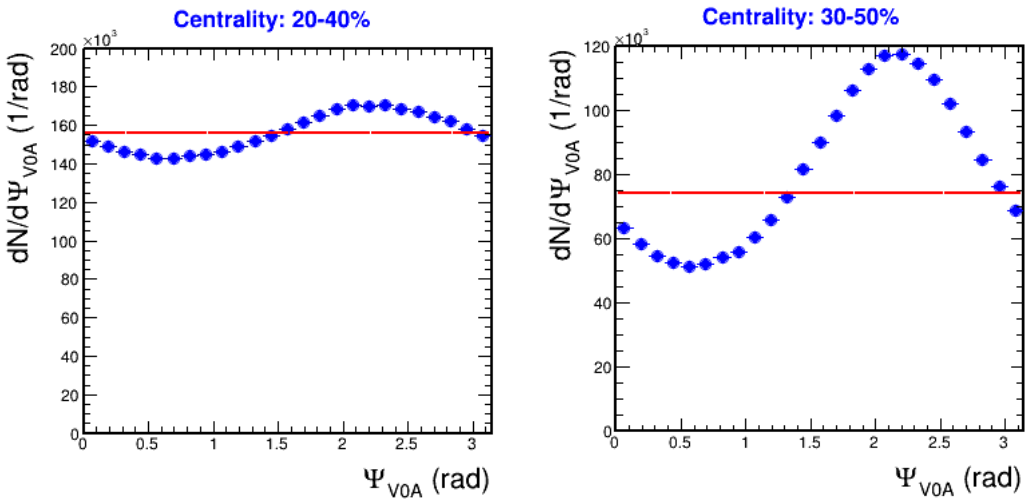

Figure 6.13.: Distribution of the angle of the event plane reconstructed with the V0A detector in 20-40% and 30-50% central Pb-Pb collisions at $\sqrt{s_{NN}}$ = 2.76 TeV. Events are selected in 20-40% centrality class with the single-shower trigger and in 30-50% centrality class with the single-shower and jet trigger systems.

Figure 6.14 shows the correction for the event-plane resolution of the event-plane angle reconstructed with the V0A detector as a function of centrality in events selected with the semi-central and single-shower triggered systems. The results are obtained from a data sample of Pb-Pb collisions at $\sqrt{s_{NN}}$ = 2.76 TeV collected in 2011. The correction for the event-plane resolution is obtained with the three event method (Section 4.2.1). Event-plane angles reconstructed with the TPC, V0A and V0C detectors are correlated according to Eq. 4.14.

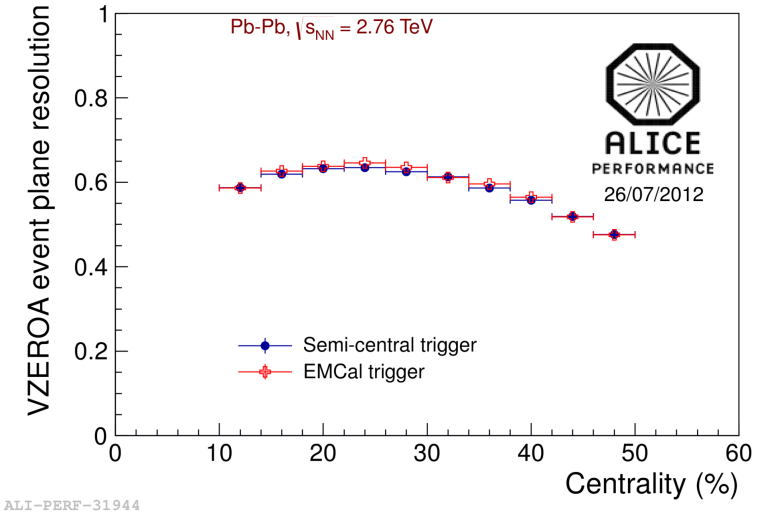

Figure 6.14.: Correction for the event-plane angle resolution of the event-plane angle reconstructed with the V0A detector as a function of centrality in semi-central and single-shower triggered events in Pb-Pb collisions at $\sqrt{s_{NN}}$ = 2.76 TeV.

6.6. Electron identification

In this section, some strategies of the electron identification with the TPC and EMCal detectors will be presented. The electron identification with the TPC detector is based on the specific energy loss per path length (dE/dx), whereas the electron identification with the EMCal is based on the measured energy and shower shape of the particles.

6.6.1. Energy loss per path length

The particles pass through the TPC detector, interact with the gas and lose energy mainly by ionization. The energy loss per path length is described by the Bethe-Block formula, which is given by [76]:

$$\left\langle \frac{dE}{dx} \right\rangle = \frac{c_1}{\beta^2} \left[\ln\left(c_2 \beta^2 \gamma^2\right) - \gamma^2 + c_3 \right] , \tag{6.17}$$

$\gamma = 1/\sqrt{1-\beta^2}$, where $\beta = v/c$, and c_1, c_2 and c_3 are parameters that depend on the material detector.

Figure 6.15 shows the calculated dE/dx using the TPC parameters as a function of the total momentum of the particle. Since the energy loss dE/dx depends on the mass and momentum of the particle (see Eq. 6.17), cuts on the specific dE/dx as a function of momentum can be applied in order to identify charged particles.

The parameter often used to select particles with the TPC is the energy loss expressed as a deviation of the measured dE/dx from the parametrized Bethe-Bloch line and divided by the energy loss resolution:

$$\sigma = \frac{dE/dx - \langle dE/dx \rangle_{part}}{\sigma_{dE/dx}} . \tag{6.18}$$

Figure 6.16 shows the measured dE/dx against the expectation for electrons in units of sigma as a function of momentum in 20-40% central Pb-Pb collisions at $\sqrt{s}$ = 2.76 TeV.

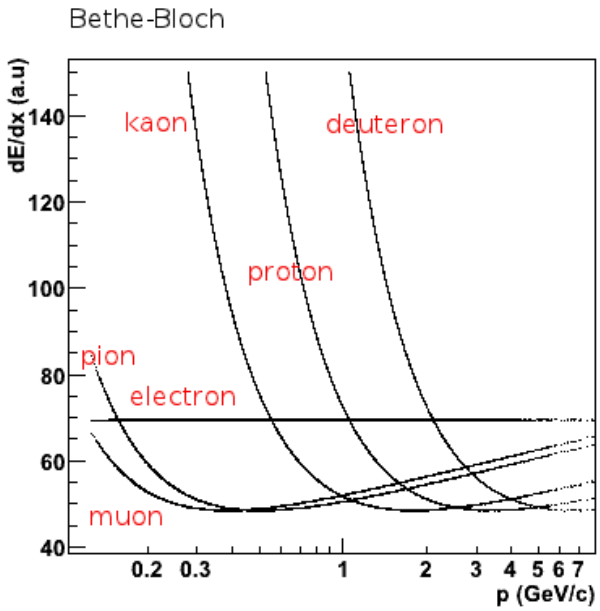

Figure 6.15.: Energy loss per path length as a function of momentum.

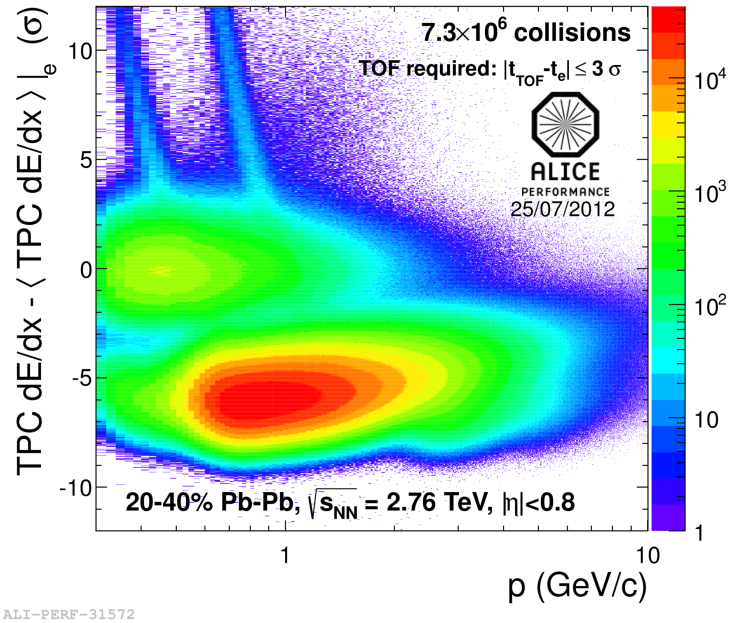

Figure 6.16.: Measured dE/dx against the expectation for electrons in units of sigma as a function of momentum in 20-40% central Pb-Pb collisions at $\sqrt{s} = 2.76$ TeV [107].

6.6.2. E/p

Electron identification with the EMCal is based on the E/p distribution, where E is the energy of the particle, which is measured with the EMCal, and p is the total momentum of the particle. The E/p distribution of electrons is around unity, since the EMCal was designed to absorb the total energy of electrons and the electron mass is negligible if compared to its momentum in experiments of heavy-ion collisions at high energy.

Figure 7.2 shows the E/p distribution in 20-40% central Pb-Pb collisions at $\sqrt{s_{NN}}$ = 2.76 TeV.

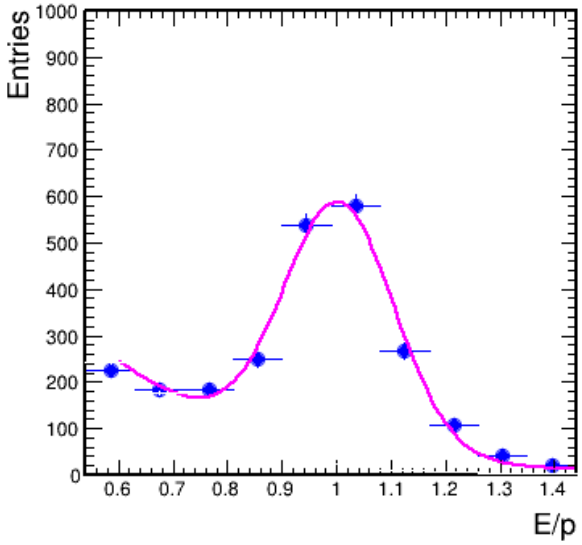

Figure 6.17.: Example of the E/p distribution in 20-40% central Pb-Pb collisions at $\sqrt{s_{NN}}$ = 2.76 TeV.

6.6.3. Shower shape

Electrons can also be identified with the EMCal by comparing the shower shapes of hadrons and electrons, which are formed by the interaction of the particles with the detector material. Electrons have a shower shape more collimated when compared to the shower shape of hadrons.

The shower shape can be verified on the ηφ plane of the EMCal surface (see Figure 6.18) by calculating the parameters M02, M20, and dispersion.

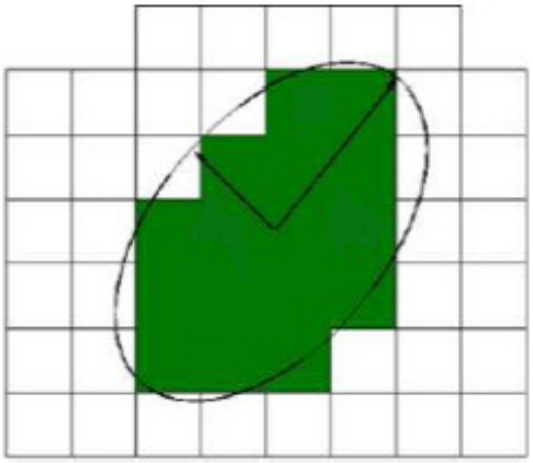

Figure 6.18.: Shower shape

The M02 and M20 parameters are defined by the equations:

$$M_{02} = \frac{d\eta\eta + d\varphi\varphi}{2} + \sqrt{\left(\frac{d\eta\eta - d\varphi\varphi}{2}\right)^2 + (d\eta\varphi)^2}\,, \tag{6.19}$$

and

$$M_{20} = \frac{d\eta\eta + d\varphi\varphi}{2} - \sqrt{\left(\frac{d\eta\eta - d\varphi\varphi}{2}\right)^2 + (d\eta\varphi)^2}\,, \tag{6.20}$$

where $d\eta\eta$, $d\varphi\varphi$ and $d\eta\varphi$ are the variances normalized to the cell weight:

$$d\eta\eta = \frac{\sum_k w_k \eta_k^2}{\sum_k w_k} - \frac{\left[\sum_k (w_k \eta_k)\right]^2}{\left(\sum_k w_k\right)^2}\,, \tag{6.21}$$

$$d\varphi\varphi = \frac{\sum_k w_k \varphi_k^2}{\sum_k w_k} - \frac{\left[\sum_k (w_k \varphi_k)\right]^2}{\left(\sum_k w_k\right)^2}\,, \tag{6.22}$$

and

$$d\eta\varphi = \frac{\sum_k w_k \eta_k \varphi_k}{\sum_k w_k} - \frac{\sum_k (w_k \eta_k) \sum_k (w_k \varphi_k)}{\left(\sum_k w_k\right)^2}\,, \tag{6.23}$$

η_k and φ_k are the local coordinates of the k-th cell cluster and w_k is the cell weight that is given by:

$$w_k = w_{0_k} + \log\left(\frac{E_k}{\sum_k E_k}\right)\,, \tag{6.24}$$

where E_k is the energy in the k-th cell. However, $w_k = 0$ if $\left[w_{0_k} + \log\left(\frac{E_k}{\sum_k E_k}\right)\right] < 0$.

The dispersion of the shower shape is given by:

$$d = \sqrt{\frac{\sum_k w_k \left[(\eta_k - \bar{\eta})^2 + (\varphi_k - \bar{\varphi})^2\right]}{\sum_k w_k}} , \tag{6.25}$$

where $\bar{\eta}$ and $\bar{\varphi}$ are the average values normalized to the cell weight:

$$\bar{\eta} = \frac{\sum_k w_k \eta_k}{\sum_k w_k} , \tag{6.26}$$

and

$$\bar{\varphi} = \frac{\sum_k w_k \varphi_k}{\sum_k w_k} . \tag{6.27}$$

Figures 6.19, 6.20, and 6.21 show results from Monte Carlo simulation of the M02, M20 and dispersion parameters, respectively, of electrons and hadrons.

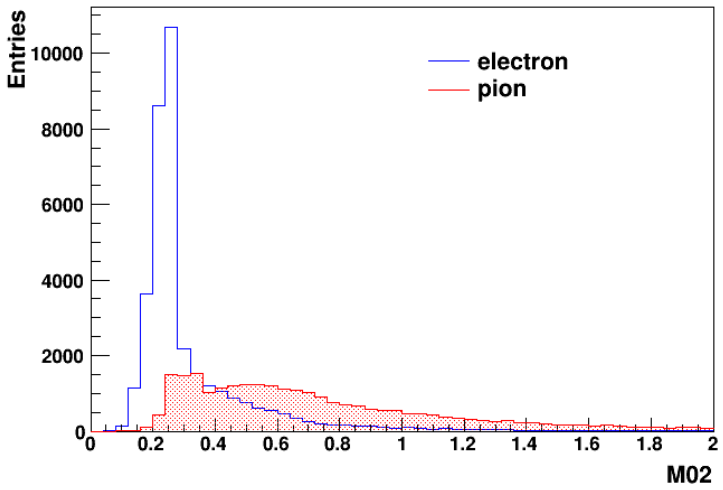

Figure 6.19.: Simulation of M02 distributions of electrons and hadrons.

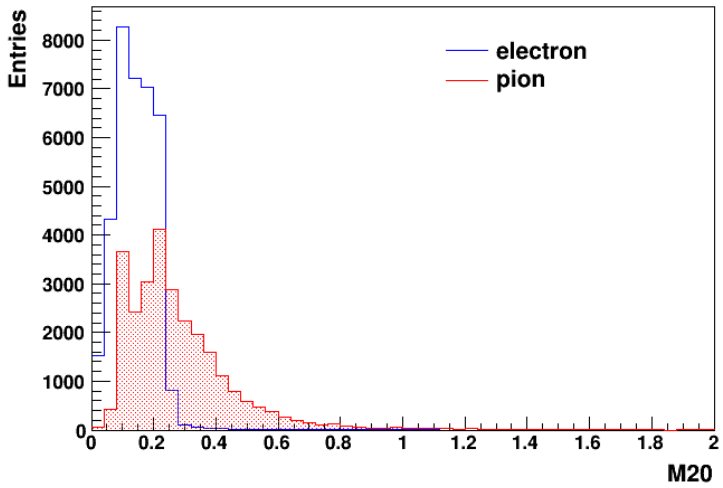

Figure 6.20.: Simulation of M20 distributions of electrons and hadrons.

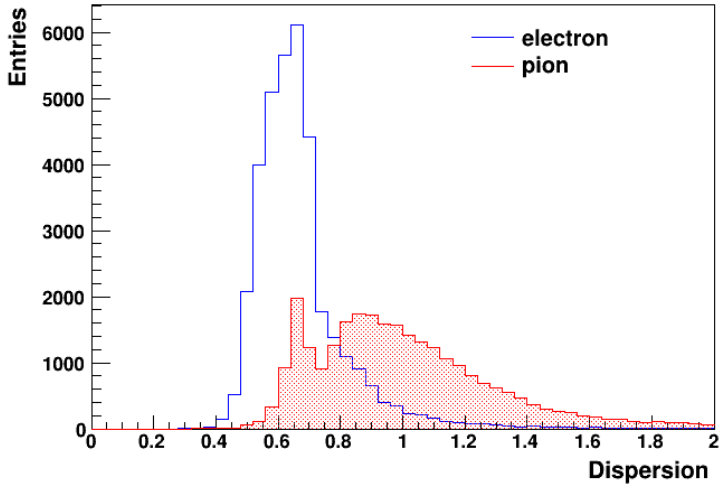

Figure 6.21.: Simulation of dispersion distributions of electrons and hadrons.

7 Analysis

The results shown in this thesis are obtained from a data sample of Pb-Pb collisions at $\sqrt{s_{\rm NN}}$ = 2.76 TeV collected in 2011. The analysis starts with the selection of events and tracks of interest (Section 7.1). Then inclusive electrons are identified at mid-rapidity (-0.7 $< \eta <$ 0.7) based on informations from the TPC and EMCal detectors (Section 7.2). The identification with the TPC is based on the specific energy loss as a function of momentum and the electron identification with the EMCal is based on the distribution of the energy to momentum ratio, which is around unity for electrons.

Inclusive electrons are counted in p_T intervals and $\Delta\varphi = \varphi - \Psi_{EP}^{V0A}$ ranges, where φ is the azimuthal angle of the inclusive electrons and Ψ_{EP}^{V0A} is the event-plane angle reconstructed with the V0A detector. A fit to the function $dN/d\Delta\varphi = k[1 + 2v_2 cos(2\Delta\varphi)]$ is used to obtain the v_2 of inclusive electrons as a function of the transverse momentum (Section 7.3). The v_2 of inclusive electrons identified in events selected with the EMCal trigger systems are corrected for the trigger effects on the v_2 measurement (Section 7.4).

The contribution of non-heavy flavour electron v_2 is evaluated with a simulation using a Monte Carlo

event generator, which uses the measured p_T distribution and v_2 of pions and kaons as an input to compute the v_2 of electrons from photon conversions and neutral meson decays (Section 7.5). This contribution is then subtracted from the inclusive electron v_2 using as weight the heavy-flavour decay electron to background ratio (Section 7.6) in order to obtain the elliptic azimuthal anisotropy of electrons from heavy-flavour decays in 20-40% and 30-50% central Pb-Pb collisions at $\sqrt{s_{\rm NN}} = 2.76$ TeV (Section 7.7). The systematic uncertainties of the analysis are discussed in Section 7.8.

Preliminary measurements of the elliptic azimuthal anisotropy of electrons from charm and beauty decays in 30-50% central Pb-Pb collisions at $\sqrt{s_{\rm NN}}$ = 2.76 TeV are shown in sections 7.9 and 7.10, respectively.

7.1. Event selection and track cuts

The events of interest are selected with the convenient trigger systems:

- semi-central trigger in order to enhance events within 20-50% centrality class,
- L1 single-shower and L1 jet triggers in order to enhance events with high-momentum electrons.

The selected events pass by an additional requirement of primary vertex within $\pm$ 10 cm in the beam direction to minimize edge effects at the limit of the central barrel acceptance. Then the remaining events are divided into two groups of 20-40% and 30-50% centrality classes, as listed in Table 7.1. Note that the jet trigger system is used only in 30-50% central events.

Centrality	Trigger	Number of events
20-40%	semi central	7275549
	single shower	1327039
30-50%	semi central	6288075
	single shower and jet	2038467

Table 7.1.: Number of analyzed events.

The particle tracks of the selected events pass by the following topological and kinematic criteria in order to suppress the background and to correct the data sample for detector effects, such as p_T interval, geometric range, etc:

- $|\eta| < 0.7$;

- no kink daughter or mother;
- $p_T > 2$ GeV/c;
- ITS requirements:
  - ITS refit status;
  - At least 3 hits on the ITS layers;
  - One hit on the first pixel layer;
- TPC requirements:
  - TPC refit status;
  - At least 100 attached TPC clusters (the total number of the TPC clusters is 160);
  - The ratio of TPC found clusters / findable TPC clusters ≥ 0.6.

The mid-rapidity cut is used to limit the acceptance of the tracks according to the acceptance of the detectors used to select electrons (TPC and EMCal). The requirement of high number of TPC clusters improves the purity of the electron sample since reconstructed electrons have, in general, more TPC clusters attached to their tracks if compared to pions due to larger energy loss of electrons in the TPC. The p_T requirement is related to the EMCal identification efficiency, which is low for $p_T < 2$ GeV/c, and the other cuts are standard quality ones used in heavy-flavour analyses.

7.2. Inclusive electron identification

Electrons at low transverse momentum are identified in events selected with the single-shower trigger, while electrons at high transverse momentum are identified in events selected with the appropriate single-shower and jet trigger systems. Table 7.2 shows the p_T interval of electrons identified in different events.

Electron candidates are first selected with the TPC detector by applying the $-1 < \sigma < 3$ requirement (see Equation 6.18). The cut is asymmetric since the hadron contamination is predominant in negative values of σ (see Fig. 6.16).

Figure 7.1 shows comparisons of the E/p distribution as a function of p_T before and after the $-1 < \sigma < 3$ requirement in events selected with the semi-central and single-shower trigger systems in 20-40% central

Centrality class	Trigger	p_T interval (GeV/c)
20-40%	semi central	2-8
	single shower	8-13
30-50%	semi central	2.5-7.5
	single shower and jet	7.5-10

Table 7.2.: p_T interval of electrons identified in events selected with different trigger systems.

Pb-Pb collisions at $\sqrt{s_{NN}}$ = 2.76 TeV. The peak of the energy to momentum ratio around unity, which corresponds predominantly to electrons, is more pronounced with the -1< σ <3 requirement.

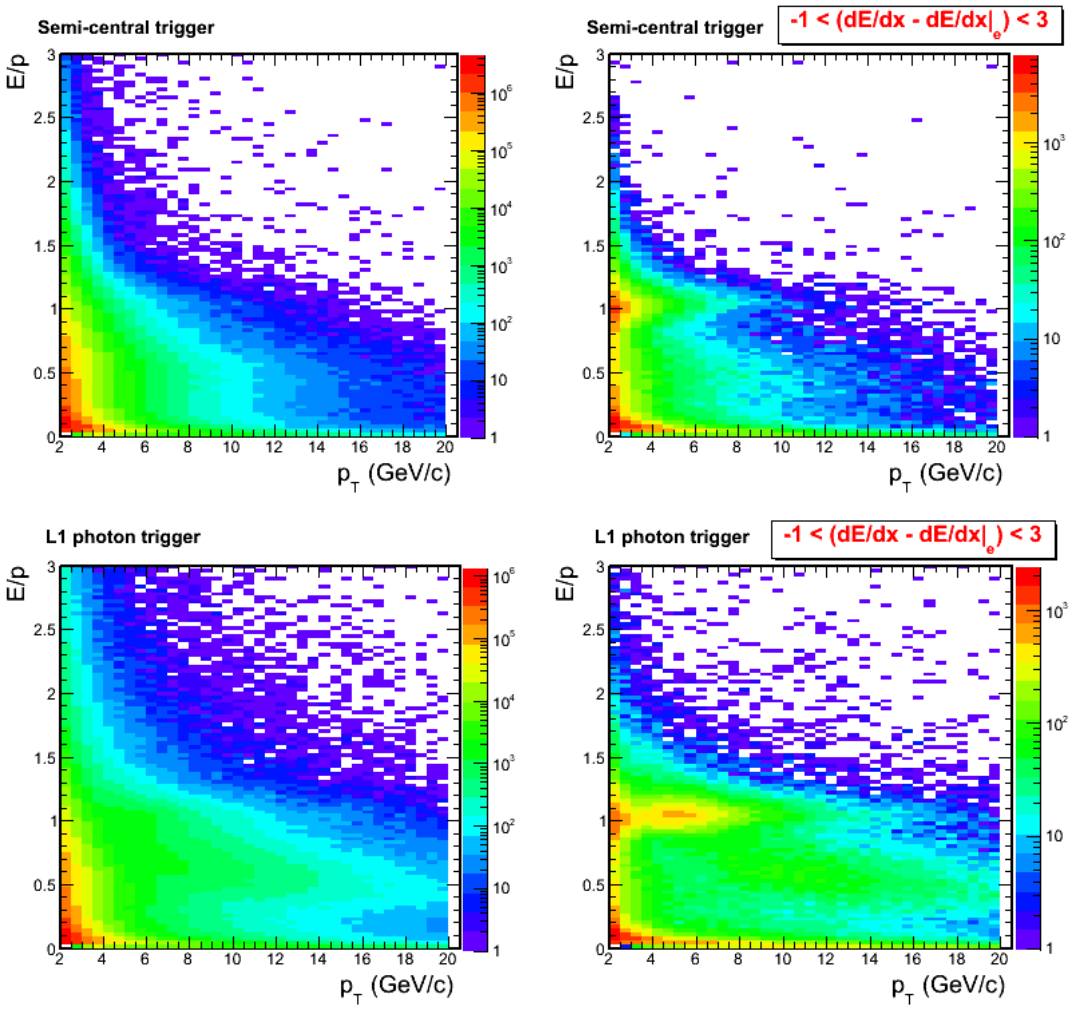

Figure 7.1.: E/p as a function of p_T before and after the -1< σ <3 requirement in events selected with the semi-central and single-shower (photon) trigger systems in 20-40% central Pb-Pb collisions at $\sqrt{s_{NN}}$ = 2.76 TeV.

In order to determine the hadron contamination, hadrons are selected with TPC detector by applying the -3.5< σ <-3.1 requirement. The E/p distributions of electron candidates with remaining hadron

background and hadrons are plotted in different p_T intervals and $\Delta\varphi = \varphi - \Psi_{EP}^{V0A}$ ranges, where φ is the azimuthal angle of electron candidates and Ψ_{EP}^{V0A} is the event plane reconstructed with the V0A detector. Once the E/p distributions of electrons and hadrons have different number of entries, a normalization is applied with the reasonable assumption that the $0.4 < E/p < 0.8$ region contains only hadrons, so the areas of the E/p distributions are the same in this region. This assumption may decrease the efficiency of the electron identification, but the purity is not affected.

An example of the E/p distribution of electrons with remaining hadron background and hadrons in 20-40% central Pb-Pb collisions at $\sqrt{s_{NN}}$ = 2.76 TeV is shown in Figure 7.2. The blue points correspond to the signal, which is obtained with the $-1 < \sigma < 3$ requirement, and the red points correspond to the hadron background, which is selected with the $-3.5 < \sigma < -3.1$ cut. The E/p distribution that corresponds to electron candidates is parametrized with the Exponential(K,x)+Gaussian(A,x_0 ,σ_0) function, which describes well the data, in order to obtain the mean and width of the distribution.

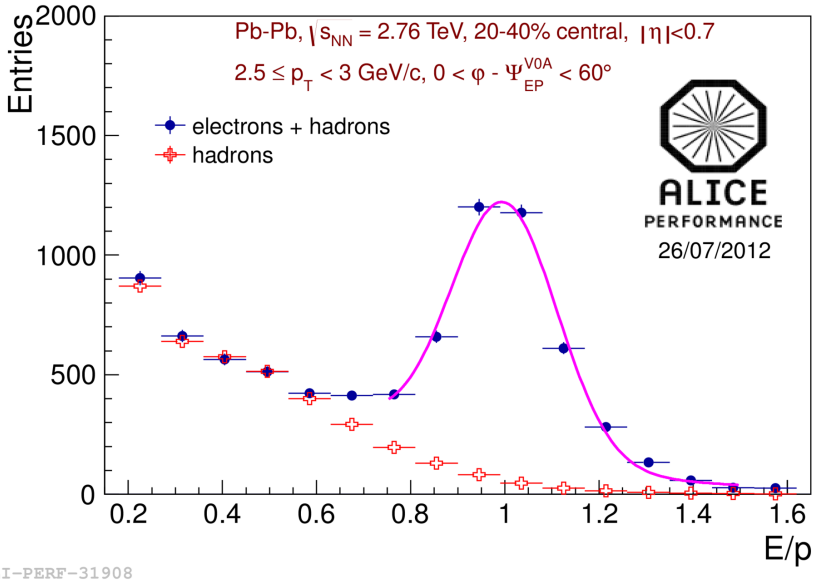

Figure 7.2.: Example of the E/p distribution in 20-40% central Pb-Pb collisions at $\sqrt{s_{NN}}$ = 2.76 TeV. The blue points correspond to the signal (electrons with remaining hadron background) and the red points correspond to the hadron background. The signal is parametrized with the Exponential(K,x) + Gaussian(A,x_0,σ_0) function. Vertical error bars are the statistical uncertainties, horizontal error bars indicate the bin widths.

Figure 7.3 shows an example of the mean and width of the E/p distribution of electron candidates with remaining hadron background obtained in events selected with the semi-central trigger in 20-40% central Pb-Pb collisions at $\sqrt{s_{NN}}$ = 2.76 TeV.

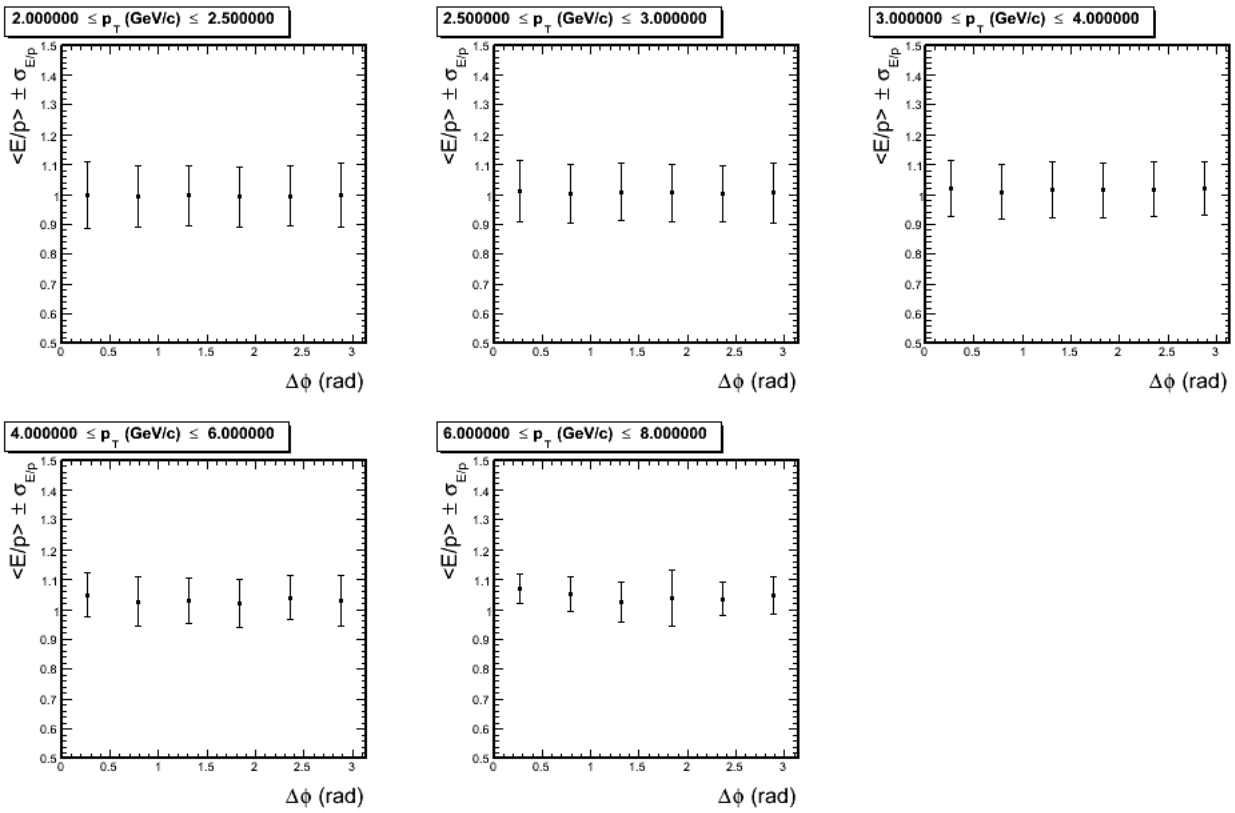

Figure 7.3.: Mean of the energy to momentum ratio of electron candidates in different p_T intervals and $\Delta\varphi = \varphi - \Psi_{EP}^{V0A}$ ranges, where φ is the azimuthal angle of electron candidates and Ψ_{EP}^{V0A} is the event plane reconstructed with the V0A detector, in events selected with the semi-central trigger in 20-40% central Pb-Pb collisions at $\sqrt{s_{NN}}$ = 2.76 TeV. Vertical bars depict the width of the energy to momentum distribution.

The E/p distribution of hadrons is subtracted from the E/p distribution of electron candidates with remaining hadron background. Then a pure sample of inclusive electrons is selected with the $\langle E/p\rangle < E/p < \langle E/p\rangle + 3\sigma_{E/p}$ requirement. The fraction of the hadron background that is subtracted in the $\langle E/p\rangle < E/p < \langle E/p\rangle + 3\sigma_{E/p}$ interval is of the order of 6%. As an example, Figure 7.4 shows the fraction of the subtracted hadron background in events selected with the semi-central trigger in 20-40% central Pb-Pb collisions at $\sqrt{s_{NN}}$ = 2.76 TeV.

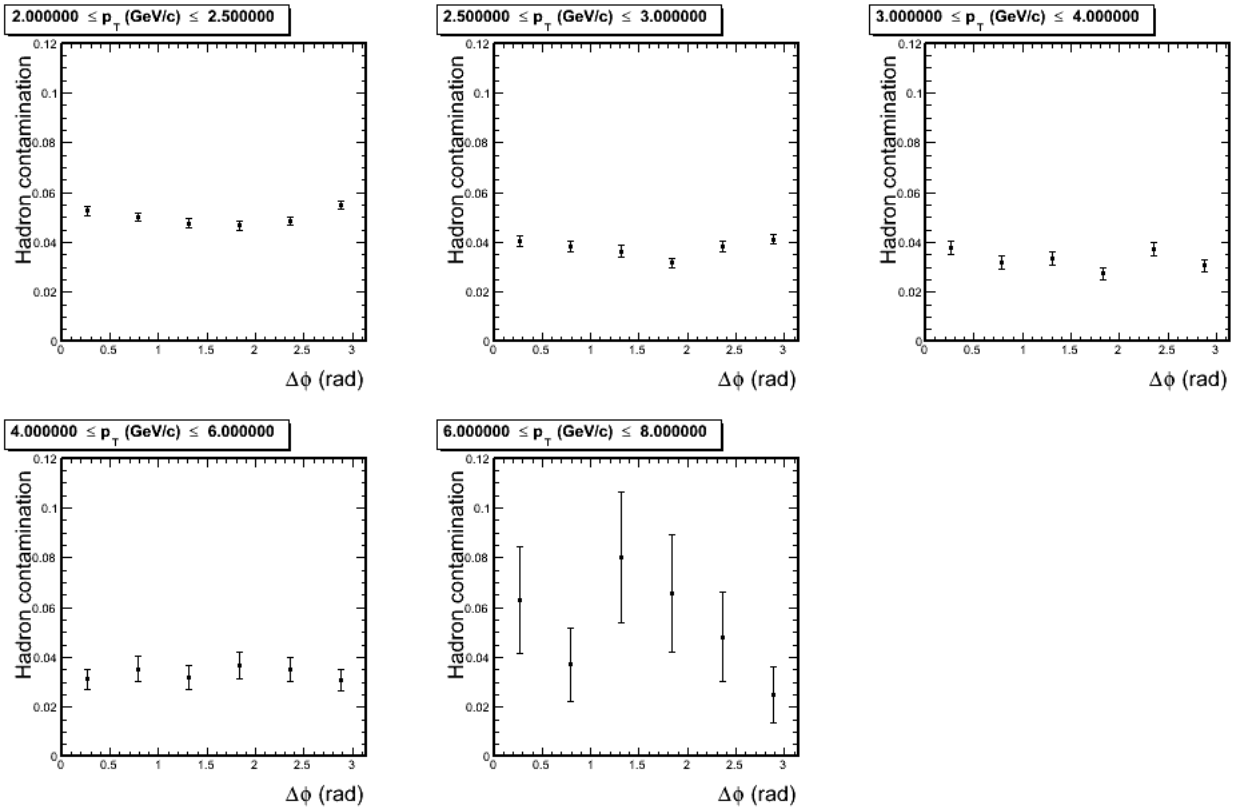

Figure 7.4.: Fraction of the subtracted hadron background in events selected with the semi-central trigger in 20-40% central Pb-Pb collisions at $\sqrt{s_{NN}}$ = 2.76 TeV. Vertical error bars are the statistical uncertainties.

7.3. Inclusive electron v_2

Inclusive electrons identified with the TPC and EMCal detectors are counted in different p_T intervals and $\Delta\varphi = \varphi - \Psi_{EP}^{V0A}$ ranges. The dN/d$\Delta\varphi$ distributions of inclusive electrons in different p_T ranges in 20-40% and 30-50% central Pb-Pb collisions at $\sqrt{s_{NN}}$ = 2.76 TeV are plotted in Figs. 7.5 and 7.6, respectively. The function 7.1 is used to fit the dN/d$\Delta\varphi$ distributions in order to obtain the v_2 coefficient in each p_T range:

$$\frac{dN}{d\Delta\varphi} = k[1 + 2v_2\cos(2\Delta\varphi)] \,, \tag{7.1}$$

where k is the amplitude of the distribution. It is assumed in Eq. 7.1 that v_2 is the dominant harmonic in the Fourier series, which is valid in non-central collisions. v_2 and χ^2/NDF values obtained from the fits shown in Figs. 7.5 and 7.6, are listed in Tables 7.3 and 7.4, respectively.

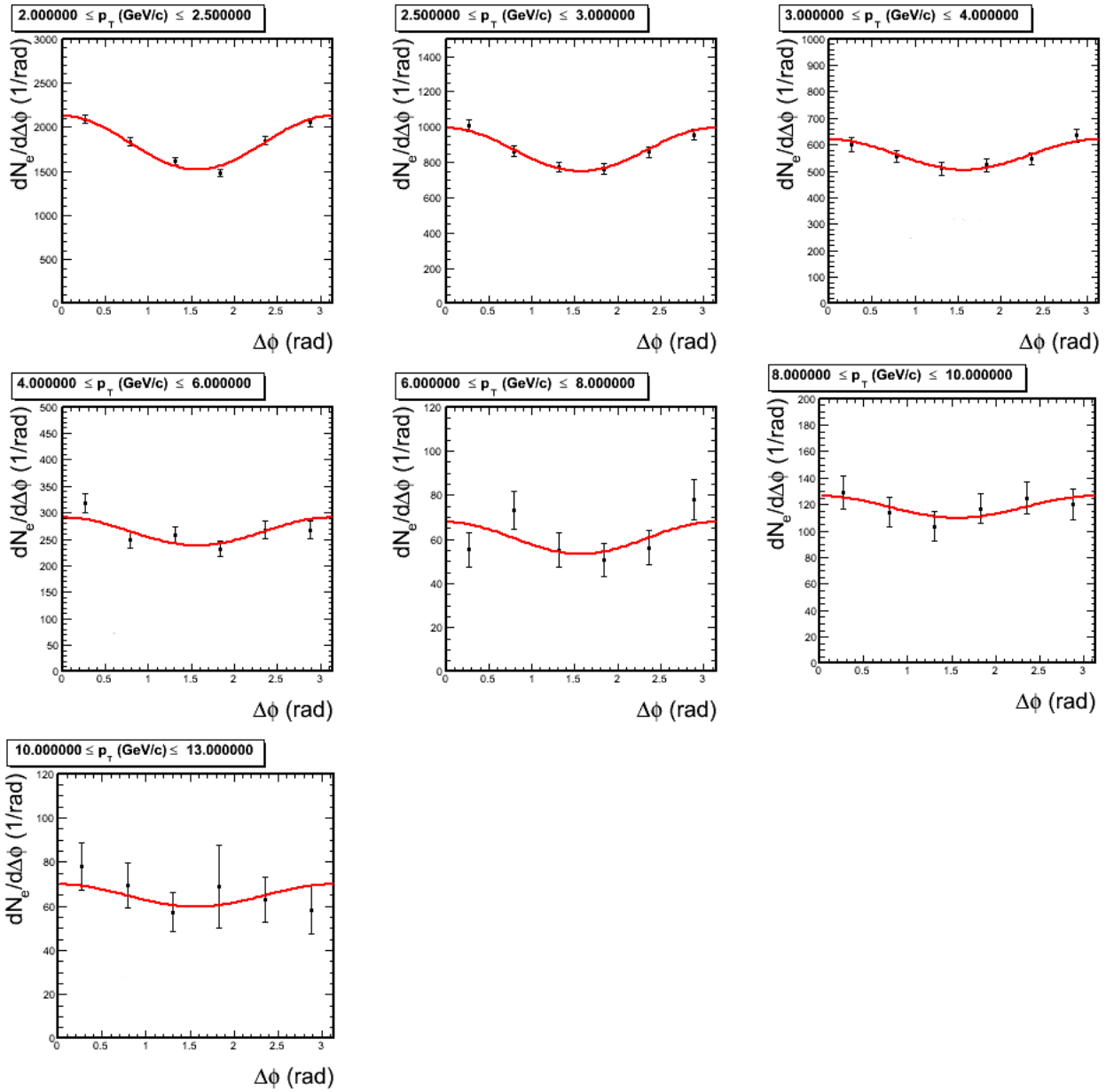

Figure 7.5.: dN/dΔφ distributions of inclusive electrons in 20-40% central Pb-Pb collisions at $\sqrt{s_{NN}}$ = 2.76 TeV. The points are parametrized with the equation 7.1. The vertical error bars are the statistical uncertainties.

p_T interval (GeV/c)	inclusive electron v_2	χ^2/NDF
2-2.5	0.0837 ± 0.0069	1.4
2.5-3	0.0707 ± 0.0099	0.4
3-4	0.051 ± 0.012	0.4
4-6	0.050 ± 0.018	1.6
6-8	0.060 ± 0.038	1.6
8-10	0.035 ± 0.028	0.3
10-13	0.039 ± 0.050	0.6

Table 7.3.: v_2 and χ^2/NDF values obtained from the fits shown in Fig. 7.5.

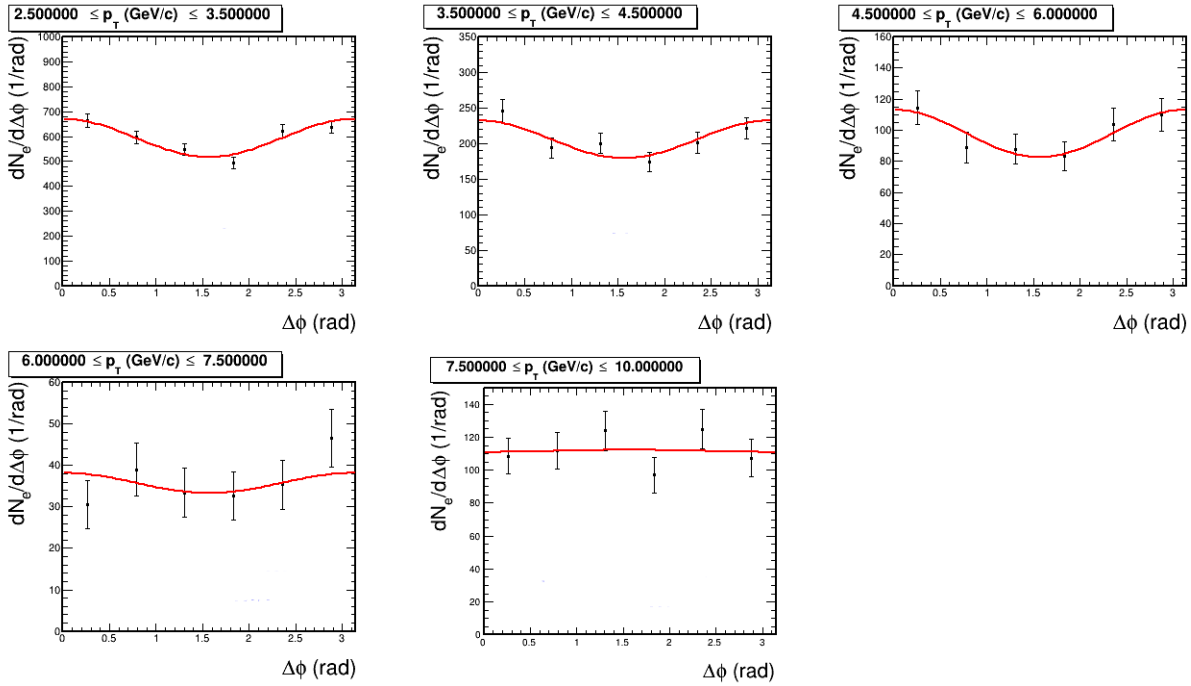

Figure 7.6.: dN/dΔφ distributions of inclusive electrons in 30-50% central Pb-Pb collisions at $\sqrt{s_{NN}}$ = 2.76 TeV. The points are parametrized with the equation 7.1. The vertical error bars are the statistical uncertainties.

p_T interval (GeV/c)	inclusive electron v_2	χ^2/NDF
2.5-3.5	0.065 $\pm$ 0.012	1.1
3.5-4.5	0.064 $\pm$ 0.020	1.0
4.5-6	0.078 $\pm$ 0.030	0.3
6-7.5	0.034 $\pm$ 0.049	0.9
7.5-10	-0.003 $\pm$ 0.029	1.1

Table 7.4.: v_2 and χ^2/NDF values obtained from the fits shown in Fig. 7.6.

The measurements of the inclusive electron v_2 as a function of transverse momentum in 20-40% and 30-50% centrality classes, respectively, in Pb-Pb collisions at $\sqrt{s_{NN}}$ = 2.76 TeV are shown in Figs. 7.7 and 7.8. Inclusive electrons at low p_T are identified in events selected with the semi-central trigger (red points), and inclusive electrons at high p_T are identified in events selected with the EMCal trigger systems (magenta points). The measurements of the inclusive electron v_2 in events selected with the EMCal triggers are affected by the nonflow and trigger issues. The correction for the trigger effects on the v_2 inclusive electron measurement is the focus of the following section.

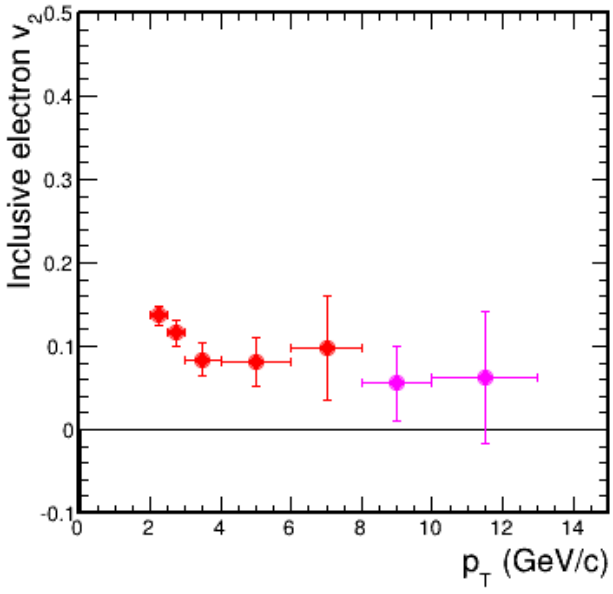

Figure 7.7.: Inclusive electron v_2 in 20-40% central Pb-Pb collisions at $\sqrt{s_{NN}}$ = 2.76 TeV. Inclusive electrons are measured with the TPC and EMCal detectors ($|\eta| < 0.7$) in events selected with the semi-central trigger (red points) and single-shower trigger (magenta points) systems. Vertical error bars are the statistical uncertainties.

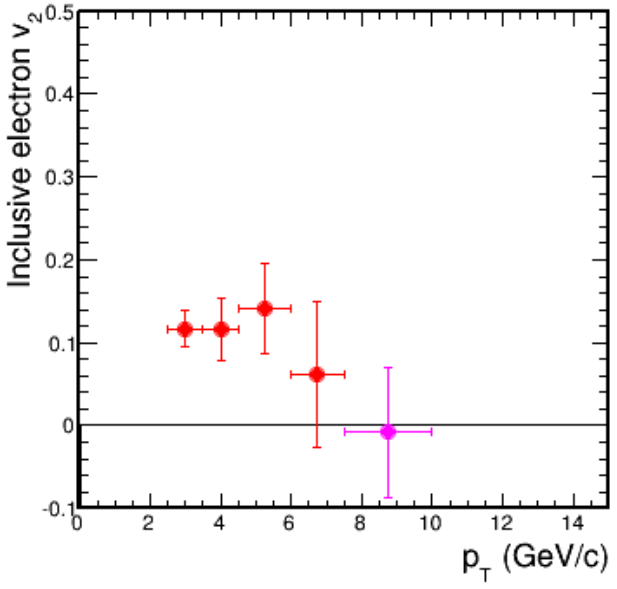

Figure 7.8.: Inclusive electron v_2 in 30-50% central Pb-Pb collisions at $\sqrt{s_{NN}}$ = 2.76 TeV. Inclusive electrons are measured with the TPC and EMCal detectors ($|\eta| < 0.7$) in events selected with the semi-central trigger (red points), and jet and single-shower trigger systems (magenta points) systems. Vertical error bars are the statistical uncertainties.

7.4. Correction for the trigger effects on the inclusive electron v_2

Jets are produced isotropically in azimuth and predominantly in central rapidity region. The contribution of nonflow due to jets is reduced in this analysis, since the event plane is reconstructed with the V0A detector at forward rapidity. However the event plane determination is biased if the v_2 measurement is done in events selected with the EMCal trigger systems, since the trigger detector (EMCal) has limited azimuthal coverage ($80^\circ < \varphi < 180^\circ$) so the rate of jets aligned to the EMCal direction is higher compared to the others directions. This problem also occurs with the single-shower trigger that might select jet as a single shower.

The *trigger effect on the event plane distribution* is investigated in events selected with the semi-central trigger in 20-40% central Pb-Pb collisions at $\sqrt{s_{NN}}$ = 2.76 TeV. The effect caused by the EMCal limited acceptance is not expected in events selected with the semi-central trigger, which is a minimum-bias trigger.

The events selected with the semi-central trigger are separated in three classes:

- No trigger: all events;
- TPC trigger: events with at least one track with total momentum greater than 3.5 GeV/c;
- EMCal trigger: events with at least one EMCal cluster with energy greater than 3.5 GeV/c^2.

Note that the TPC and EMCal trigger classes simulate trigger systems, whose trigger detector has full and limited azimuthal coverage, respectively.

Figure 7.9 shows the normalized event-plane angle distribution of the three event classes. The event plane distribution is not flat only in events selected with the detector with limited azimuthal coverage, which indicates that the non-flatness is due to the acceptance of the trigger detector. Additional flattening procedures can not be applied since there is no physical meaning or detector issue.

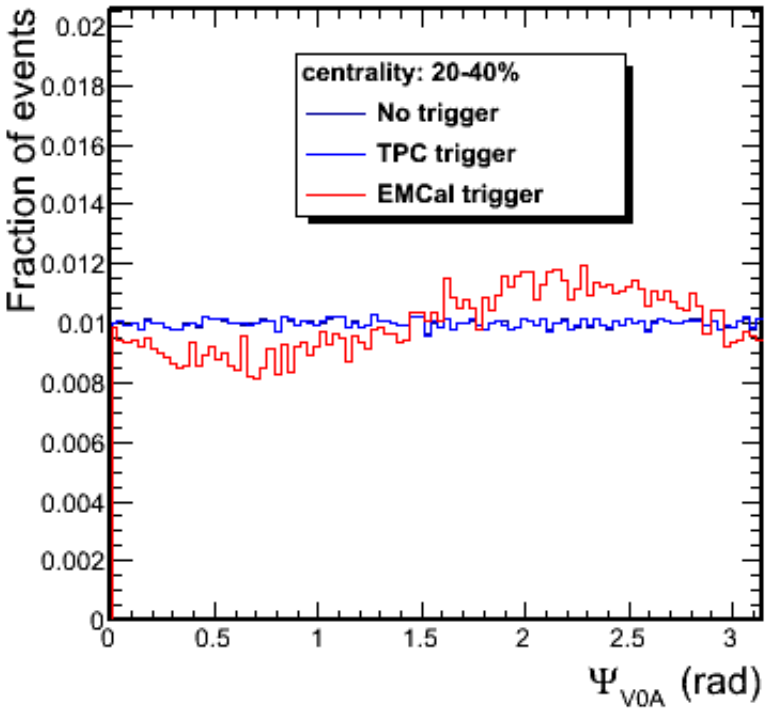

Figure 7.9.: Normalized event-plane angle distribution in events selected with the semi-central trigger in 20-40% central Pb-Pb collisions at $\sqrt{s_{NN}}$ = 2.76 TeV. No trigger corresponds to all events, TPC trigger corresponds to events with at least one track with total momentum greater than 3.5 GeV/c, and EMCal trigger corresponds to events with at least one EMCal cluster with energy greater than 3.5 GeV/c^2.

In order to verify the *trigger effect on the v_2 measurement*, the following analysis is done using unidentified charged particles in 20-40% central Pb-Pb collisions at $\sqrt{s_{NN}}$ = 2.76 TeV. The v_2 coefficient of unidentified charged particles is measured in events selected with the semi-central and single-shower trigger systems and also inside the EMCal azimuthal coverage and in full azimuth. The event plane in this analysis is reconstructed with the V0A detector.

Figure 7.10 shows v_2 of unidentified charged particles inside the EMCal acceptance in events selected with the semi-central and single-shower triggers. The measured v_2 in events selected with the single-shower trigger is higher than v_2 in events selected with the semi-central trigger at low transverse momentum and the difference is of the order of 20%. At high p_T, the ratio is compatible with unity.

Figures 7.11 and 7.12 show v_2 of unidentified charged particles in full azimuth and inside the EMCal acceptance in events selected with the semi-central and single-shower trigger systems, respectively. The difference in the v_2 ratio is of the order of 20% in events selected with the single-shower trigger and negligible in events selected with the semi-central trigger.

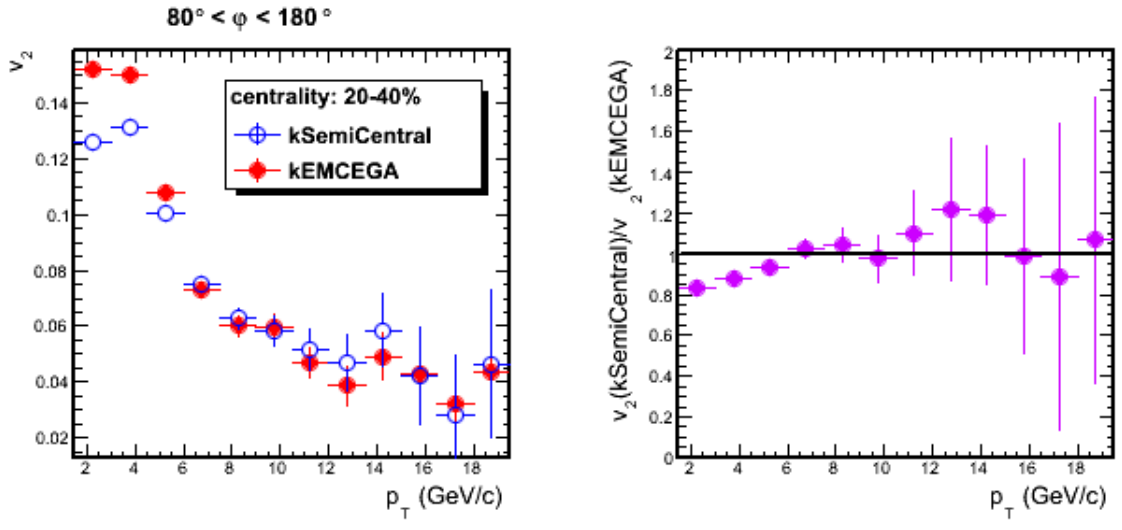

Figure 7.10.: Left panel: Unidentified charged particle v_2 in events selected with the semi-central (kSemiCentral) and single-shower (kEMCEGA) trigger systems inside the EMCal acceptance in 20-40% central Pb-Pb collisions at $\sqrt{s_{NN}}$ = 2.76 TeV. Right panel: Ratio of measured unidentified charged particle v_2. Vertical error bars are the statistical uncertainties.

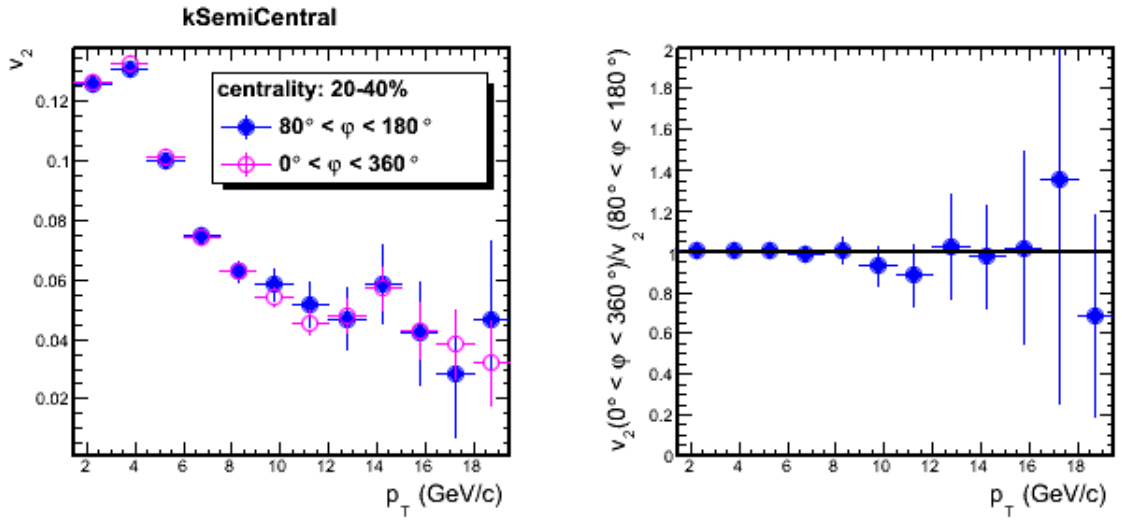

Figure 7.11.: Left panel: v_2 of unidentified charged particles inside the EMCal acceptance and in full azimuth in events selected with the semi-central trigger in 20-40% central Pb-Pb collisions at $\sqrt{s_{NN}}$ = 2.76 TeV. Right panel: Ratio of measured unidentified charged particle v_2. Vertical error bars are the statistical uncertainties.

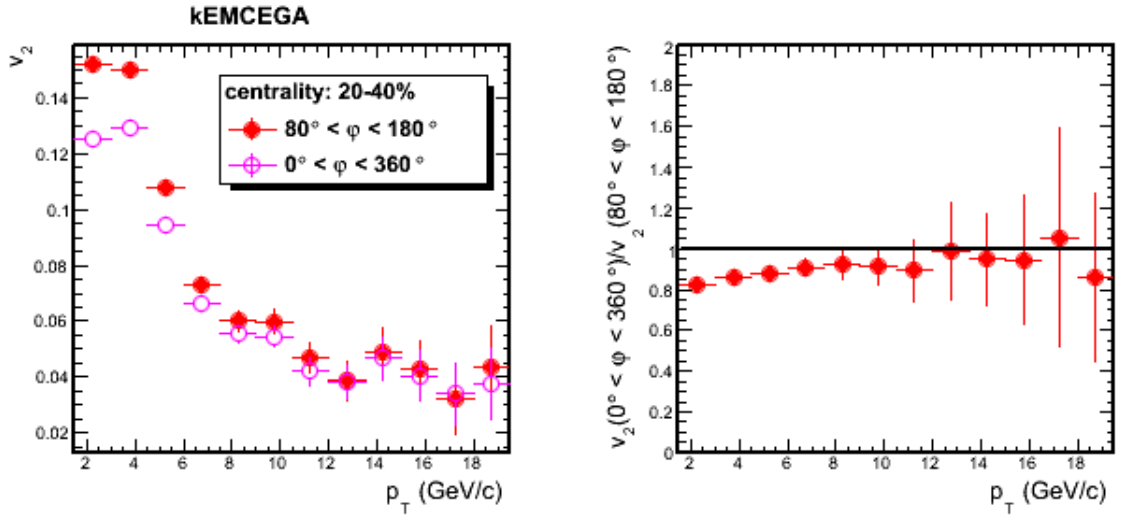

Figure 7.12.: Left panel: v_2 of unidentified charged particles inside the EMCal acceptance and in full azimuth in events selected with the single-shower trigger in 20-40% central Pb-Pb collisions at $\sqrt{s_{NN}}$ = 2.76 TeV. Right panel: Ratio of measured unidentified charged particle v_2. Vertical error bars are the statistical uncertainties.

Therefore two effects are observed in the v_2 measurement in events selected with the trigger system that is provided with a trigger detector with limited azimuthal coverage:

- v_2 is higher in events selected with trigger systems compared to minimum-bias events;

- v_2 is higher inside the trigger detector acceptance than in full azimuth.

The *non-uniformity of the distribution of events selected with the EMCal trigger systems* (see Figs. 6.10 and 6.11) is investigated in measurements of unidentified charged particle v_2 in Pb-Pb collisions at $\sqrt{s_{NN}}$ = 2.76 TeV. The measurement is done in integrated 20-40% centrality range and in four centrality bins (20-25%, 25-30%, 30-35%, and 35-40%).

The fractions of the events selected with the single-shower trigger in 20-40% central Pb-Pb collisions at $\sqrt{s_{NN}}$ = 2.76 TeV are listed in Table 7.5. The average of the v_2 measured in four centrality bins weighted by these fractions corresponds to the v_2 measured in integrated 20-40% centrality range, while the simple average (weight equal to 0.25) of the v_2 measured in four centrality bins corresponds to the case where the distribution of events is uniform.

Centrality class	Fraction of events
20-25%	0.31
25-30%	0.34
30-35%	0.18
35-40%	0.17

Table 7.5.: Fractions of the events selected with the single-shower trigger in 20-40% central Pb-Pb collisions at $\sqrt{s_{NN}}$ = 2.76 TeV.

The simple average of the unidentified charged particle v_2 measured in four centrality ranges is compared with the unidentified charged particle v_2 measured in integrated centrality range. It is not observed significant difference between the measurements, as shown in Fig. 7.13, since the ratio of both measurements is compatible with unity.

Equation 7.2 is the used to correct the unidentified charged particle v_2 measurement for the trigger effects. In this correction, the two effects mentioned previously are taken into account as well as the non-uniformity of the number of events as function of centrality, even if the last effect is not significant in the considered centrality class and p_T interval.

$$\text{Correction} = \frac{v_2(0 < \varphi < 360^\circ, \text{minimum-bias trigger})}{v_2(\text{EMCal acceptance}, \text{EMCal trigger})} \,. \tag{7.2}$$

Figure 7.14 shows the comparison of unidentified charged particle v_2 in 20-40% central Pb-Pb collisions at $\sqrt{s_{NN}}$ = 2.76 TeV inside the EMCal acceptance in events selected with the single-shower trigger system and unidentified charged particle v_2 in full azimuthal angle coverage in events selected with the

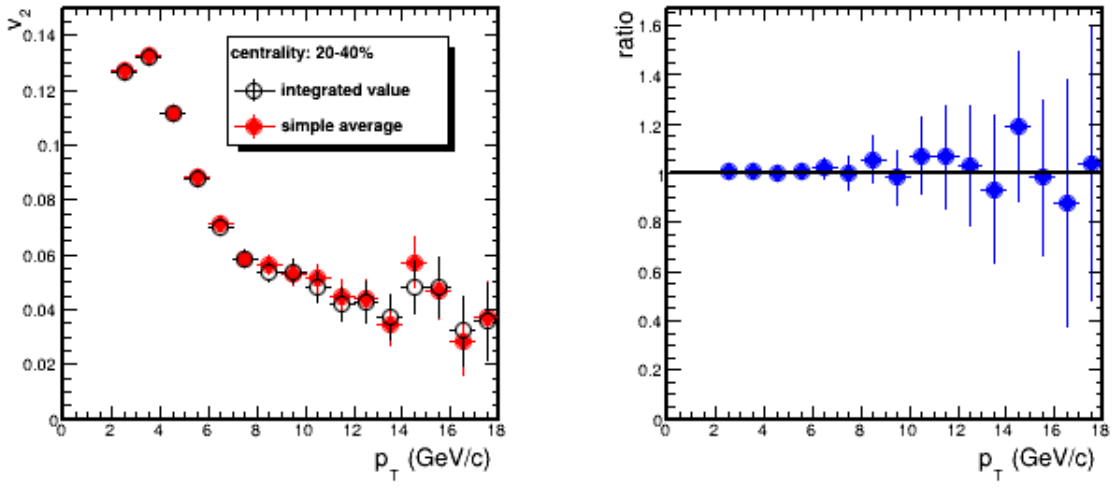

Figure 7.13.: Left panel: Comparison of the integrated value of unidentified charged particle v_2 in 20-40% central Pb-Pb collisions at $\sqrt{s_{NN}}$ = 2.76 TeV with simple average of v_2 measured in four centrality ranges (20-25%, 25-30%, 30-35% and 35-40%). Right panel: Ratio of measured unidentified charged particle v_2. Vertical error bars are the statistical uncertainties.

semi-central trigger system. The ratio of both measurements corresponds to the correction given by Eq. 7.2. The correction at low p_T is also of the order of 20% at low pt, which indicates that the effects are strongly correlated.

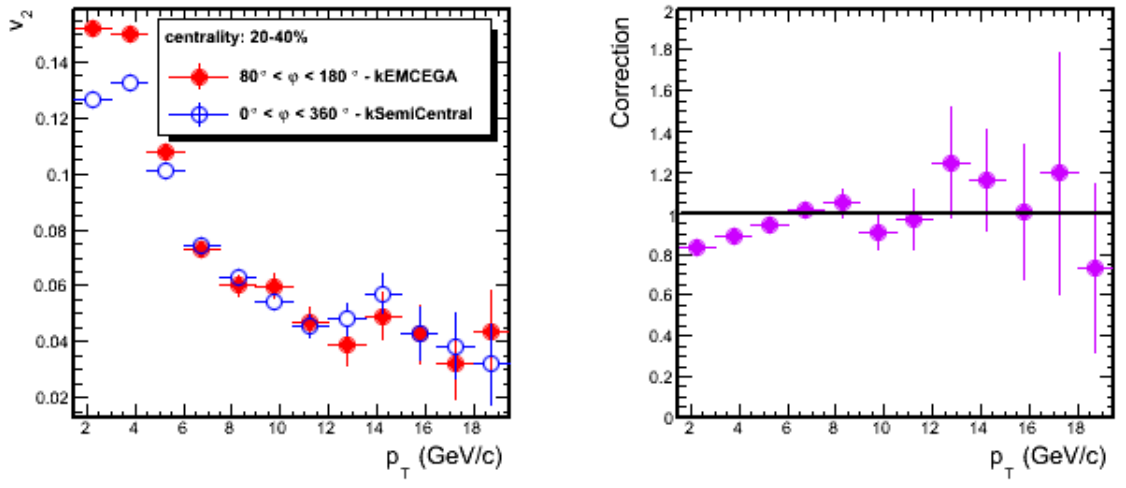

Figure 7.14.: Left panel: Comparison of unidentified charged particle v_2 in 20-40% central Pb-Pb collisions at $\sqrt{s_{NN}}$ = 2.76 TeV inside the EMCal acceptance in events selected with the single-shower trigger system and unidentified charged particle v_2 in full azimuthal angle coverage in events selected with the semi-central trigger system. Right panel: ratio of the mentioned measurements, which corresponds to the correction defined in Eq. 7.2. Vertical error bars are the statistical uncertainties.

In principle, the correction is applicable to the unidentified charged particle v_2, but it is used to correct the inclusive electron v_2 in this analysis. The corrections used in the inclusive electron v_2 measurement are shown in Table 7.6. Note that the correction in 30-50% central events is higher, since the events are selected with single-shower and jet trigger systems, and the bias caused by the jet trigger system is more pronounced (see Figure 6.10).

Centrality	p_T range (GeV/c)	Correction
20-40%	8-10	1.035(36)
	10-13	1.028(62)
30-50%	7.5-10	0.669(22)

Table 7.6.: Corrections for the trigger effect on the inclusive electron v_2 measured in 20-40% and 30-50% central Pb-Pb collisions at $\sqrt{s_{NN}}$ = 2.76 TeV.

7.5. Background electron v_2

As discussed in Section 4.3, the background electron v_2 must be evaluated and subtracted from the measured inclusive electron v_2 in order to obtain the heavy-flavour electron v_2.

The contribution of the background electron v_2 is accomplished by using the cocktail subtraction method, which uses the measured p_T distribution and v_2 of the main background sources as an input of the simulation using a Monte Carlo event generator.

Figure 7.15 shows the inclusive electron yield as function of p_T, which is corrected for efficiency and acceptance, in 20-40 % Pb-Pb collisions at $\sqrt{s_{NN}}$ = 2.76 TeV compared to a cocktail of known background electrons.

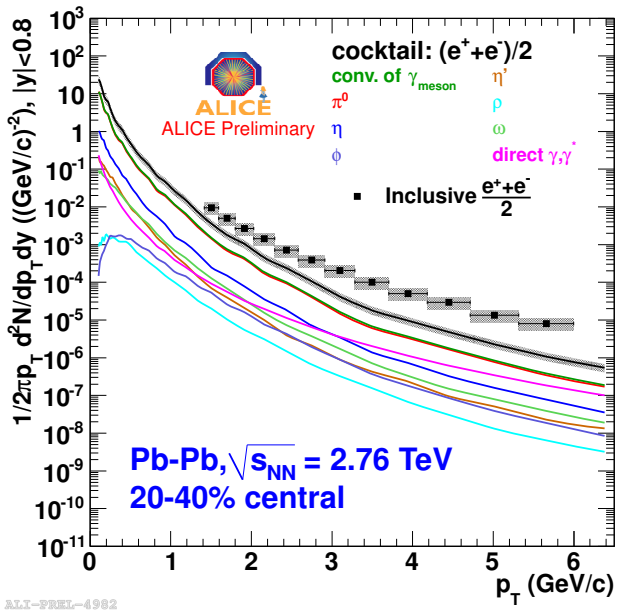

Figure 7.15.: Inclusive electron yield as a function of p_T in 20-40 % Pb-Pb collisions at $\sqrt{s_{NN}}$ = 2.76 TeV compared to a cocktail of known background electrons. Vertical error bars are the statistical uncertainties, horizontal error bars indicate the bin widths. Filled boxes are the total systematic uncertainties [107].

Figure 7.16 shows the relative contributions of the background electrons from the main sources as function of p_T.

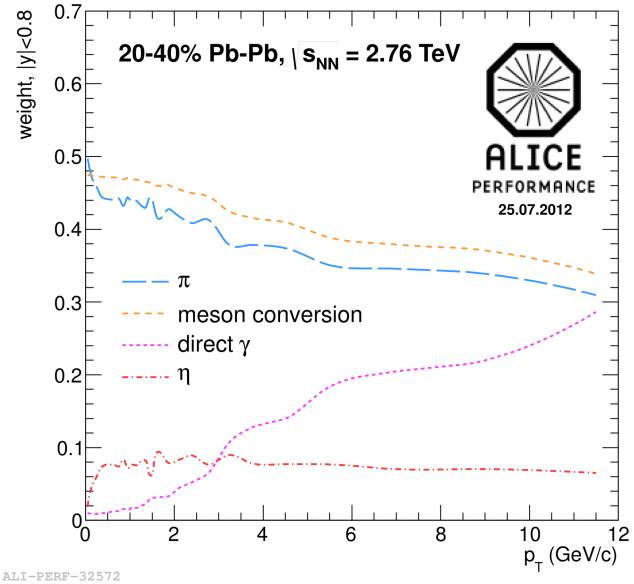

Figure 7.16.: Relative contributions of the background electrons used in the cocktail [107].

The background electron sources included in the cocktail used in the heavy-flavour electron v_2 analy-

sis are: π^0, η, and photons. The measured yields of pions and kaons are used as an input in the cocktail and it is assumed that $v_2^{\pi^\pm} = v_2^{\pi^0}$, $v_2^{\eta} = v_2^{K^\pm}$, and $v_2^{dir.\gamma} = 0$. Since there is no current measurement of the elliptic azimuthal anisotropy of η, it is used $v_2^{\eta} = v_2^{K^\pm}$, which assumes m_T scaling.

The v_2 of the electrons from the main background sources is evaluated with a Monte Carlo simulation and the contributions of the different background electron sources, i, are summed according to their relative weights, ω_i, which are shown in Figure 7.16. The cocktail v_2 is given by:

$$v_2^{\text{cocktail}} = \sum_i \omega_i v_{2_i}^e \, . \tag{7.3}$$

Figures 7.17 and 7.18 show the elliptic azimuthal anisotropy of background electrons estimated with the cocktail method in 20-40% and 20-50% central Pb-Pb collisions at $\sqrt{s_{NN}}$ = 2.76 TeV, respectively. Note that the cocktail evaluated in 20-40% centrality class has the same p_T interval as the inclusive electron v_2 measurement. The cocktail obtained in 20-50% centrality class is used as an estimate of the 30-50% centrality class. Since the p_T interval is different compare to the inclusive electron v_2 measurement, a polynomial function is used to parametrize the background electron v_2 in 20-50% centrality class in order to obtain the value in the same p_T interval used in the inclusive electron v_2 measurement.

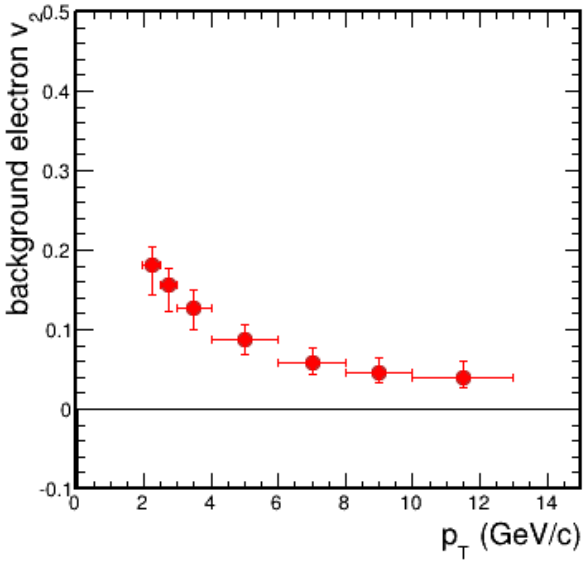

Figure 7.17.: Elliptic azimuthal anisotropy of background electrons estimated with the cocktail method in 20-40% central Pb-Pb collisions at $\sqrt{s_{NN}}$ = 2.76 TeV. Vertical error bars are the systematic uncertainties, horizontal error bars indicate the bin widths.

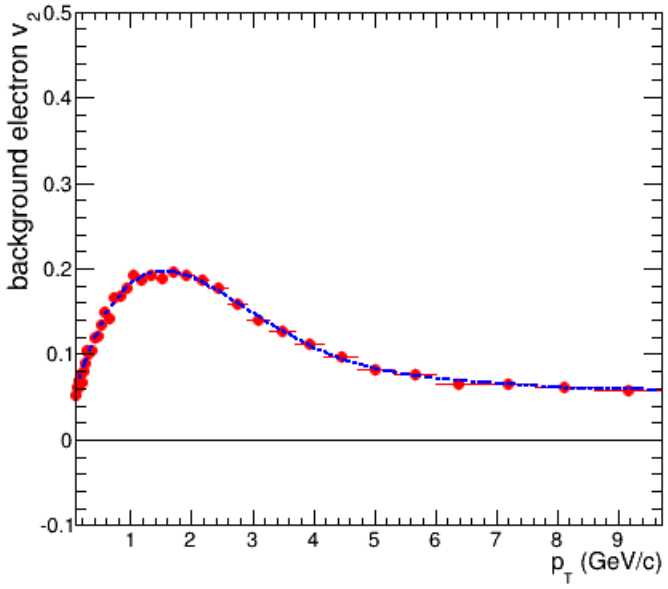

Figure 7.18.: Elliptic azimuthal anisotropy of background electrons estimated with the cocktail method in 20-50% central Pb-Pb collisions at $\sqrt{s_{NN}}$ = 2.76 TeV. Vertical error bars are the systematic uncertainties, horizontal error bars indicate the bin widths. Line indicates the polynomial function used to parametrize the background electron v_2 in order to obtain the value in the same p_T interval as the measured inclusive electron v_2.

7.6. Heavy-flavour electron to background electron ratio

As discussed in Section 4.3, the heavy-flavour electron to background electron ratio (R) is used in the subtraction of the background electron v_2 from the inclusive electron v_2 in order to obtain the heavy-flavour v_2. Experimentally, the ratio is obtained by:

$$R(p_T) = \frac{dN^{incl.elec.}/dp_T}{\varepsilon^{-1}\, dN^{backg.elec.}/dp_T} - 1 \,, \tag{7.4}$$

where ε is the efficiency of the background electron identification.

The efficiency of the background electron identification is estimated with a hadronic charm simulation in 20-40% central Pb-Pb collisions at $\sqrt{s_{NN}}$ = 2.76 TeV performed with Hijing 2012. The efficiency is evaluated by comparing the number of the background electrons reconstructed with the same identification cuts used in the data sample with respect to the total number of background electrons.

The simulation used in this analysis contains enhancements of π^0 and η that bias the background electron spectrum and, consequently, the efficiency of the background electron reconstruction. However,

weights of π^0 and η decays (Eq. 7.5) can be used to scale the background electron spectrum.

$$\text{weight} = \frac{dN^{gen.}/dp_T}{dN^{enh.}/dp_T}\,, \tag{7.5}$$

where $dN^{gen.}/dp_T$ corresponds to the yield of the generated sample and $dN^{enh.}/dp_T$ corresponds to the yield of the enhanced sample.

Figure 7.19 shows the simulation of the yield of total, generated and enhanced π^0 in 20-40% and 30-50% central Pb-Pb collisions at $\sqrt{s_{NN}}$ = 2.76 TeV.

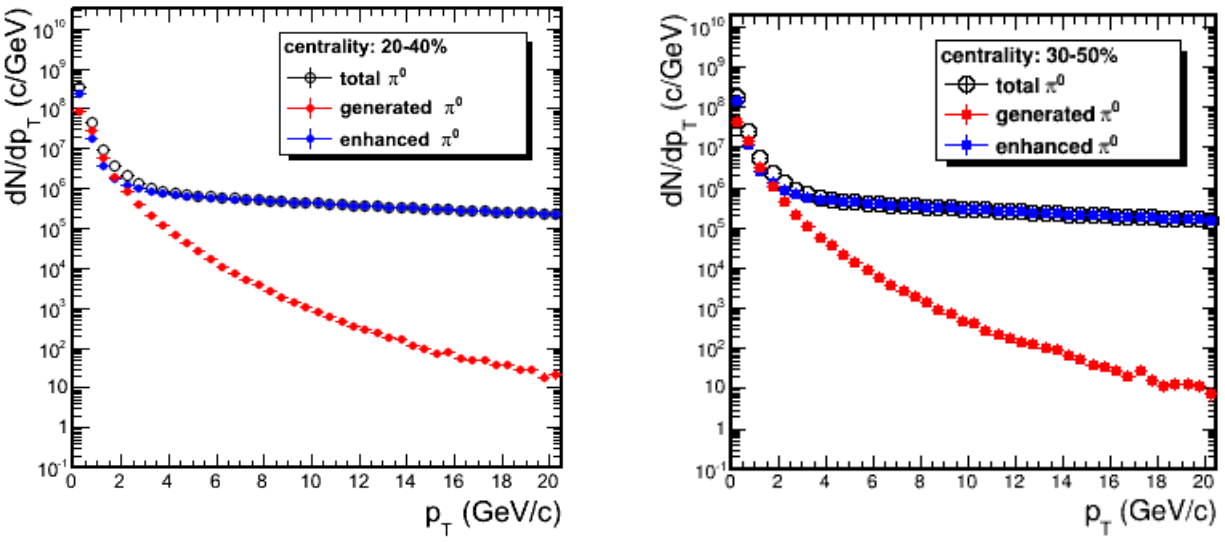

Figure 7.19.: Simulation of the π^0 yield in 20-40% and 30-50% central Pb-Pb collisions at $\sqrt{s_{NN}}$ = 2.76 TeV. Total, generated and enhanced samples of π^0 are shown.

Figure 7.20 shows the weight of π^0 decays in 20-40% and 30-50% central Pb-Pb collisions at $\sqrt{s_{NN}}$ = 2.76 TeV. The generated yield is parametrized by a modified Hagedorn function, which describes the pion production, and the enhanced yield is parametrized by the exponential function for $p_T < 5$ GeV/c and a constant for $p_T > 5$ GeV/c, which describe well the data. Therefore, the weight, which is given by Eq. 7.5, results in:

$$\pi^0 \text{ weight} = \begin{cases} \dfrac{k\ p_T}{\left(p_0+\frac{p_T}{p_1}\right)^n} \cdot e^{-x} & \text{if } p_T \leq 5 \text{ GeV/c} \\ \dfrac{k\ p_T}{\left(p_0+\frac{p_T}{p_1}\right)^n} & \text{if } p_T > 5 \text{ GeV/c}\,. \end{cases} \tag{7.6}$$

The parameters obtained from the fits shown in Fig. 7.20 are listed in Table 7.7.

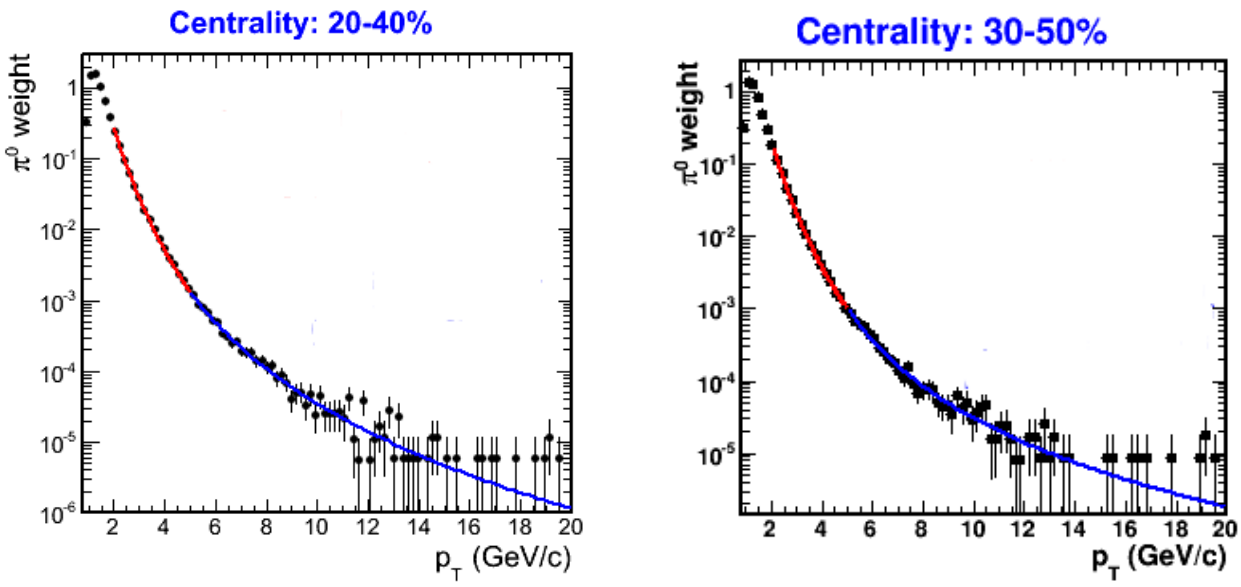

Figure 7.20.: Weights of the π^0 decays in 20-40% and 30-50% central Pb-Pb collisions at $\sqrt{s_{NN}}$ = 2.76 TeV.

centrality class	p_T interval (GeV/c)	χ^2/NDF	k	p_0	p_1	n
20-40%	$p_T \leq 5$	1.6	2.683 ± 0.053	0.7041 ± 0.0013	3.1922 ± 0.0073	17.337 ± 0.029
	$p_T > 5$	0.7	0.00040 ± 0.00011	-0.176 ± 0.053	3.99 ± 0.17	5.63 ± 0.20
30-50%	$p_T \leq 5$	1.3	2.392 ± 0.083	0.6888 ± 0.0024	3.005 ± 0.011	16.8812 ± 0.046
	$p_T > 5$	0.5	0.000186 ± 0.000071	-0.606 ± 0.095	3.16 ± 0.19	4.37 ± 0.25

Table 7.7.: Values of the parameters obtained from the fits shown in Fig. 7.20.

Figure 7.19 shows the simulation of the yield of total, generated and enhanced η in 20-40% and 30-50% central Pb-Pb collisions at $\sqrt{s_{NN}}$ = 2.76 TeV.

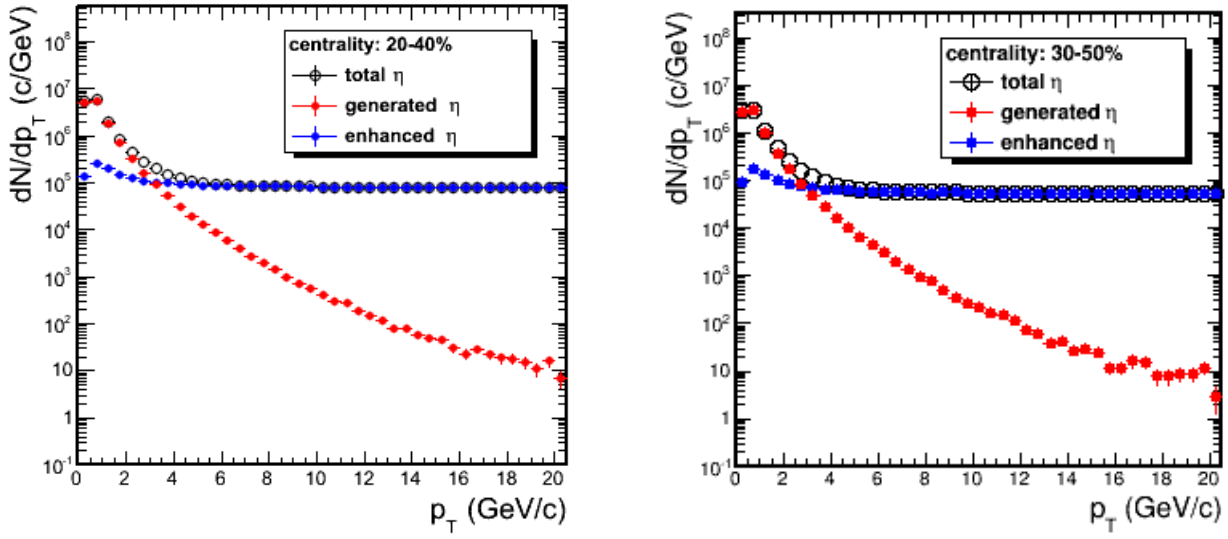

Figure 7.21.: Simulation of the η yield in 20-40% and 30-50% central Pb-Pb collisions at $\sqrt{s_{NN}}$ = 2.76 TeV. Total, generated and enhanced samples of η are shown.

Figure 7.22 shows the weight of η decays in 20-40% and 30-50% central Pb-Pb collisions at $\sqrt{s_{NN}}$ = 2.76 TeV. The generated yield is parametrized by a modified Hagedorn function, since the η/π^0 ratio is expected to be constant, and the enhanced yield is parametrized by a constant, which describe well the data. The weight, which is given by Eq. 7.5, results in:

$$\eta \text{ weight} = \frac{k\, p_T}{\left(p_0 + \frac{p_T}{p_1}\right)^n} \,. \tag{7.7}$$

The parameters obtained from the fits shown in Fig. 7.22 are listed in Table 7.8.

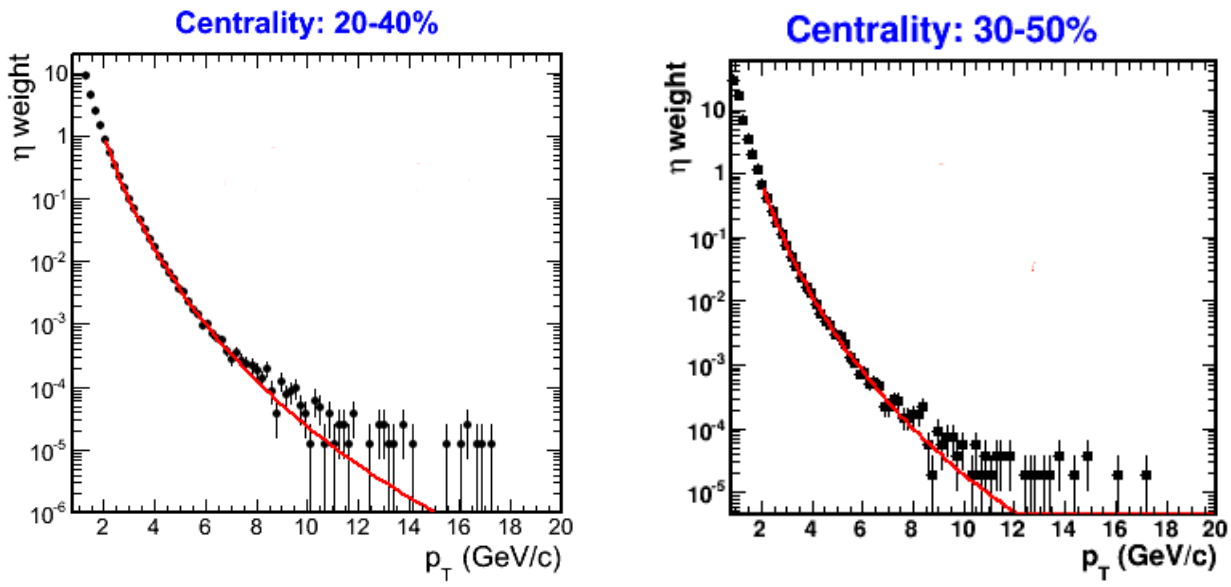

Figure 7.22.: Weights of the η decays in 20-40% and 30-50% central Pb-Pb collisions at $\sqrt{s_{NN}}$ = 2.76 TeV.

centrality class	χ^2/NDF	k	p_0	p_1	n
20-40%	1.2	16.33 ± 0.55	0.4916 ± 0.0042	2.100 ± 0.011	9.494 ± 0.032
30-50%	1.2	0.623 ± 0.029	0.3230 ± 0.0053	2.736 ± 0.019	9.180 ± 0.049

Table 7.8.: Values of the parameters obtained from the fits shown in Fig. 7.20.

The weights shown in Eqs. 7.7 and 7.6 with the parameters shown in Tables 7.7 and 7.8 are used to scale the background electron spectrum, which is used to obtain the efficiency of the background electron identification.

The background electron is obtained via invariant mass method, which basically consists of searching partner of electrons and positrons and, since the invariant mass of the photonic electrons is small, a cut in the invariant mass can be used to identify photonic electrons, which are the dominant background of electrons at low p_T.

For each tagged electron candidate passing the heavy-flavour electron cuts, the invariant mass with tracks identified as electron with looser cuts in the event is calculated. The difference between the unlike-sign (UL) and like-sign (LS) invariant mass spectrum gives the amount of identified background electrons.

The selection criteria required on the associated electron tracks are the following:

- $p_T > 0.5$ GeV/c;

- ITS refit status;
- TPC refit status;
- $|\eta| < 0.9$;
- TPC $\chi^2 < 3.5$;
- At least 100 of 160 TPC clusters.

The associated electrons are selected with the TPC detector by applying the $65 <$ dE/dx (a.u.) < 100 requirement and the invariant mass between the tagged and associated electron tracks is required to be smaller than 10 MeV/c^2. A maximum cut on the opening angle between the two tracks of 0.1 rad is also applied.

Figure 7.23 shows the invariant mass after the subtraction of the like-sign pairs from the unlike-sign pairs. The peak around zero corresponds to the photonic electrons.

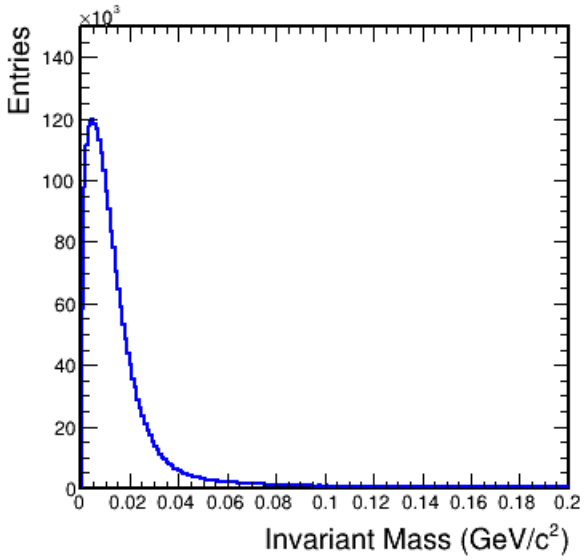

Figure 7.23.: Invariant mass after the subtraction of the like-sign pairs from the unlike-sign pairs. The peak around zero corresponds to the photonic electrons.

Figure 7.24 shows the efficiency of the background electron reconstruction as function of p_T in 20-40% and 30-50% central Pb-Pb collisions at $\sqrt{s_{NN}}$ = 2.76 TeV. The efficiencies are low since strong cuts are applied to identify background electrons with high purity.

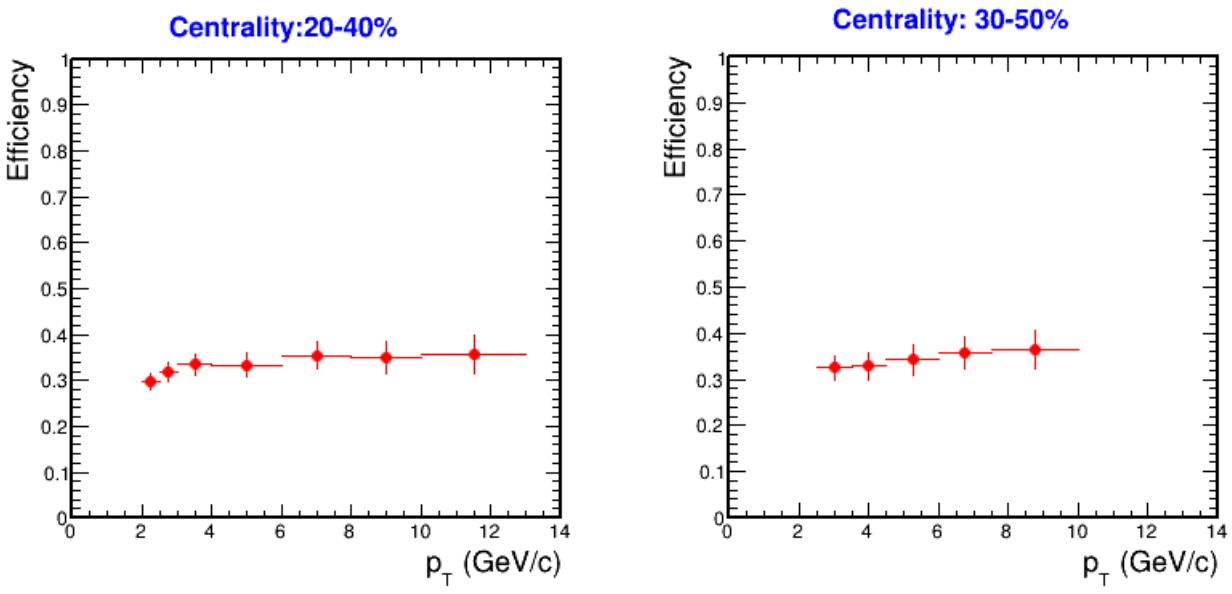

Figure 7.24.: Efficiency of the background electron reconstruction as a function of p_T in 20-40% and 30-50% central Pb-Pb collisions at $\sqrt{s_{NN}}$ = 2.76 TeV.

Figure 7.25 shows the heavy-flavour electron to background electron ratio in 20-40% and 30-50% central Pb-Pb collisions at $\sqrt{s_{NN}}$ = 2.76 TeV. The photonic electron background is dominant a low p_T, so the heavy-flavour electron to background electron ratio is expected to increase with the transverse momentum. However it is not possible to observe this behavior with the current uncertainties.

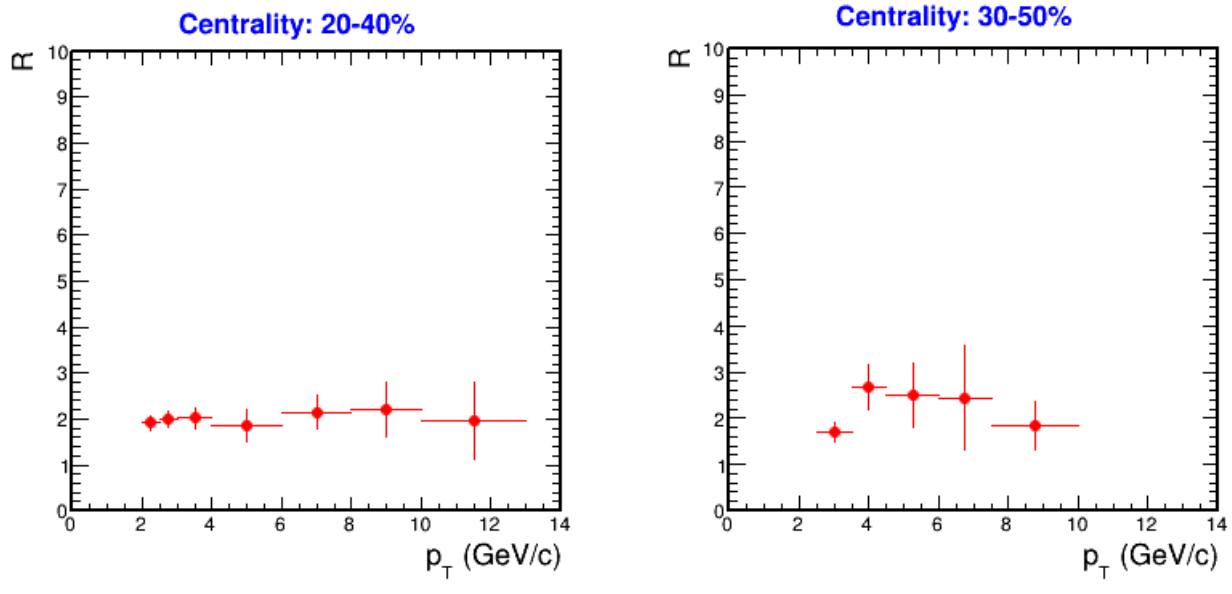

Figure 7.25.: Heavy-flavour electron to background electron ratio (Equation 7.4) as function of p_T in 20-40% and 30-50% central Pb-Pb collisions at $\sqrt{s_{NN}}$ = 2.76 TeV.

7.7. v_2 of electrons from heavy-flavour decays

The measurement of the elliptic azimuthal anisotropy of electrons from heavy-flavour decays in 20-40% central Pb-Pb collisions at $\sqrt{s_{NN}}$ = 2.76 TeV is shown in Fig. 7.26. The background electron v_2 is subtracted from the inclusive electron v_2 according to the equation 4.43. Another measurement of the heavy-flavour electron to background electron ratio is used to obtain this result, but it is compatible with the ratio shown in Fig. 7.25.

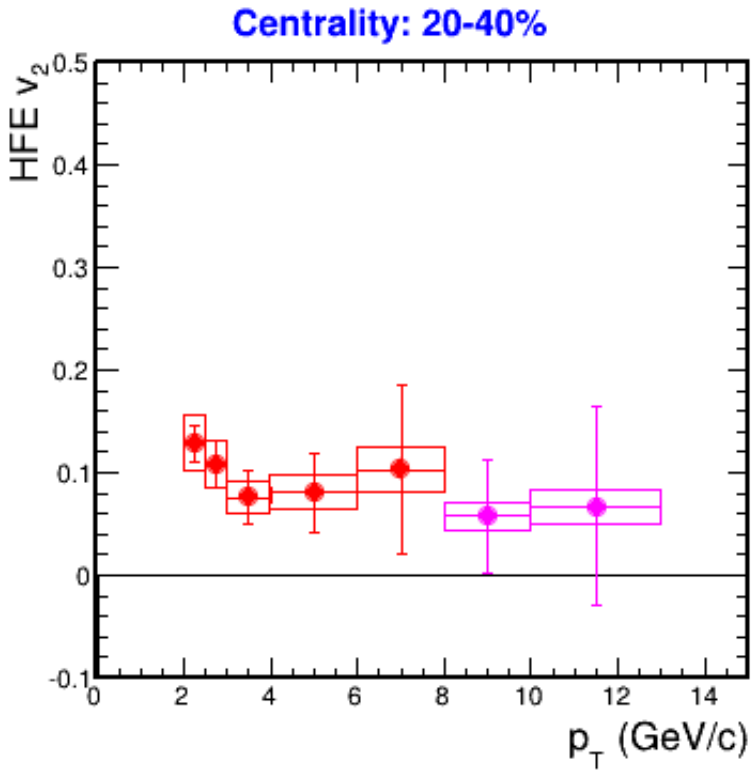

Figure 7.26.: Elliptic azimuthal anisotropy of electrons after subtraction of the background electrons estimated with the cocktail method in 20-40% central Pb-Pb collisions at $\sqrt{s_{NN}}$ = 2.76 TeV. Vertical error bars are the statistical uncertainties and horizontal error bars indicate the bin widths, and empty boxes are the total systematic uncertainties.

The preliminary result of the elliptic azimuthal anisotropy of electrons from heavy-flavour decays in 30-50% central Pb-Pb collisions at $\sqrt{s_{NN}}$ = 2.76 TeV is shown in Fig. 7.27.

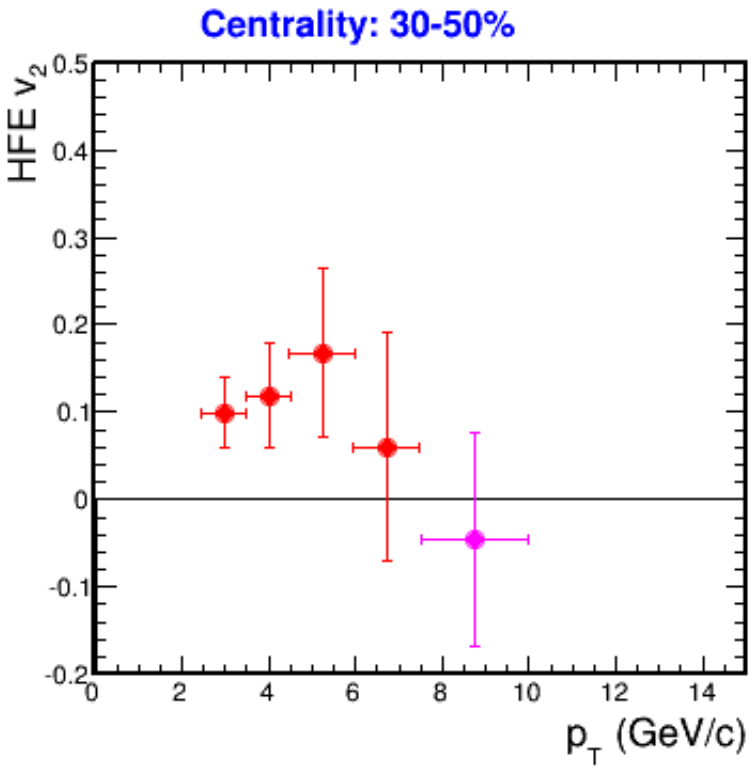

Figure 7.27.: Preliminary result of the elliptic azimuthal anisotropy of electrons from heavy-flavour decays in 30-50% central Pb-Pb collisions at $\sqrt{s_{NN}}$ = 2.76 TeV. Vertical error bars are the statistical uncertainties and horizontal error bars indicate the bin widths.

7.8. Systematic uncertainties

The relevant systematic uncertainty sources of the elliptic azimuthal anisotropy of electrons from heavy-flavour decays in 20-40% central Pb-Pb collisions at $\sqrt{s_{NN}}$ = 2.76 TeV are listed below:

- Electron identification

  The E/p and σ requirements used to identify inclusive electrons in the analysis are varied to strong cuts: $\langle E/p\rangle + 0.5\sigma_{E/p} < E/p < \langle E/p\rangle + 3\sigma_{E/p}$, and -0.5 $< \sigma <$ 3, respectively. The resulting fluctuations of the elliptic azimuthal anisotropy of electrons from heavy-flavour decays are taken as systematic uncertainties (see Figs. 7.28 and 7.29). Looser cuts are not applied on E/p and σ variables in order to verify the fluctuations, since they would affect the inclusive electron purity.

- Hadron contamination

  The hadron contamination is parametrized with the exponential function and the difference be-

tween the hadron determination with TPC σ requirement and with this fit in the heavy-flavour electron v_2 result (see Fig. 7.30) is taken as systematic uncertainty.

- Heavy-flavour electron to background electron ratio

  Variations are applied to the R parameter: $R \pm \sigma_R$, where σ_R is the statistical uncertainty of the R parameter measurement. The resulting fluctuation of the elliptic azimuthal anisotropy of electrons from heavy-flavour decays (see Fig. 7.31) is taken as systematic uncertainty.

- Correction for the event-plane resolution

  Variations of 2% are applied to the correction for the event-plane resolution and the resulting fluctuation of the elliptic azimuthal anisotropy of electrons from heavy-flavour decays (see Fig. 7.32) is taken as systematic uncertainty.

- Correction for the trigger effects on the inclusive electron v_2 measurement

  It is not possible to verify the differences between correction for charged particles and for electrons. Therefore a conservative number is taken as systematic uncertainty.

- Uniformity in the centrality distribution

  Systematic uncertainties are based on discussions in Section 7.4.

- Cocktail

  The electron background v_2 is varied according to the low and high limits of the cocktail systematic uncertainty (see Fig. 7.33), $\sigma_{low}^{cocktail}$ and $\sigma_{high}^{cocktail}$, respectively. The resulting fluctuation of the elliptic azimuthal anisotropy of electrons from heavy-flavour decays (see Fig. 7.34) is taken as systematic uncertainty.

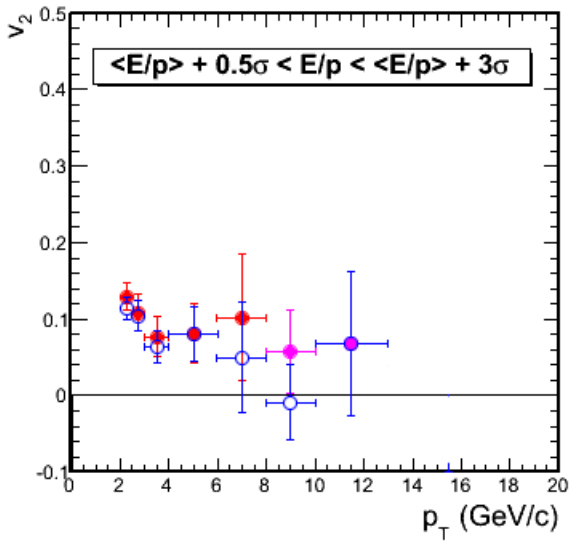

Figure 7.28.: Heavy-flavour electron v_2 as function of p_T in 20-40% central Pb-Pb collisions at $\sqrt{s_{NN}}$ = 2.76 TeV with the variation of the E/p cut. Blue points correspond to the measured v_2 after variation.

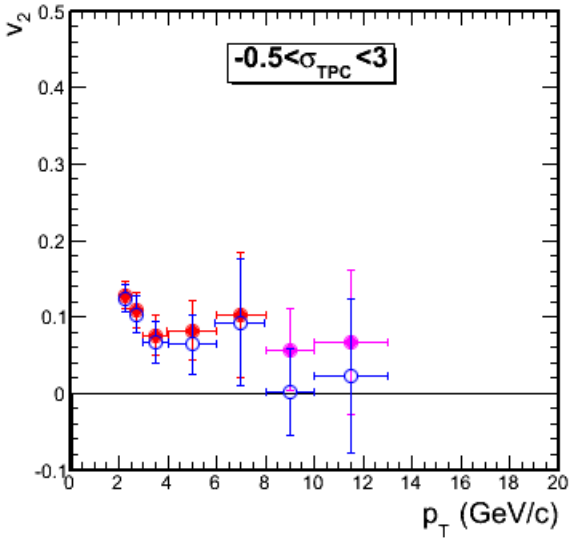

Figure 7.29.: Heavy-flavour electron v_2 as function of p_T in 20-40% central Pb-Pb collisions at $\sqrt{s_{NN}}$ = 2.76 TeV with the variation of the σ cut. Blue points correspond to the measured v_2 after variation.

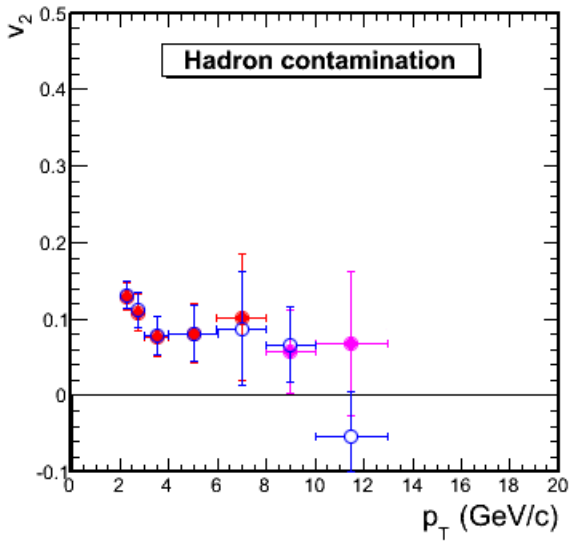

Figure 7.30.: Heavy-flavour electron v_2 as function of p_T in 20-40% central Pb-Pb collisions at $\sqrt{s_{NN}}$ = 2.76 TeV with the variation due to another procedure used to estimate the hadron contamination. Blue points correspond to the measured v_2 after variation.

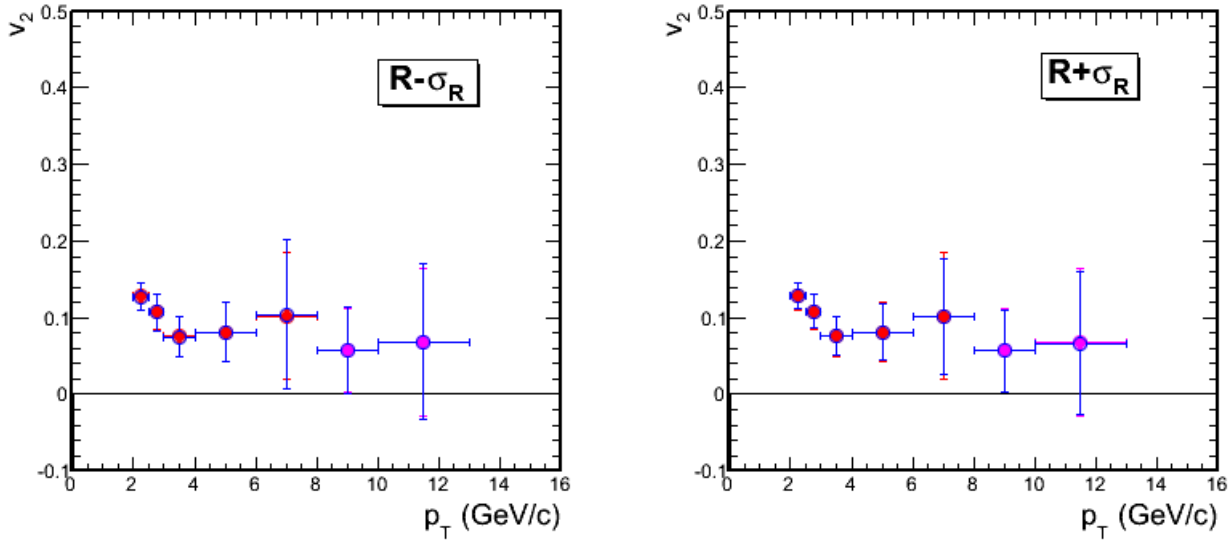

Figure 7.31.: Heavy-flavour electron v_2 as function of p_T in 20-40% central Pb-Pb collisions at $\sqrt{s_{NN}}$ = 2.76 TeV with the variation of the R parameter. Blue points correspond to the measured v_2 after variation.

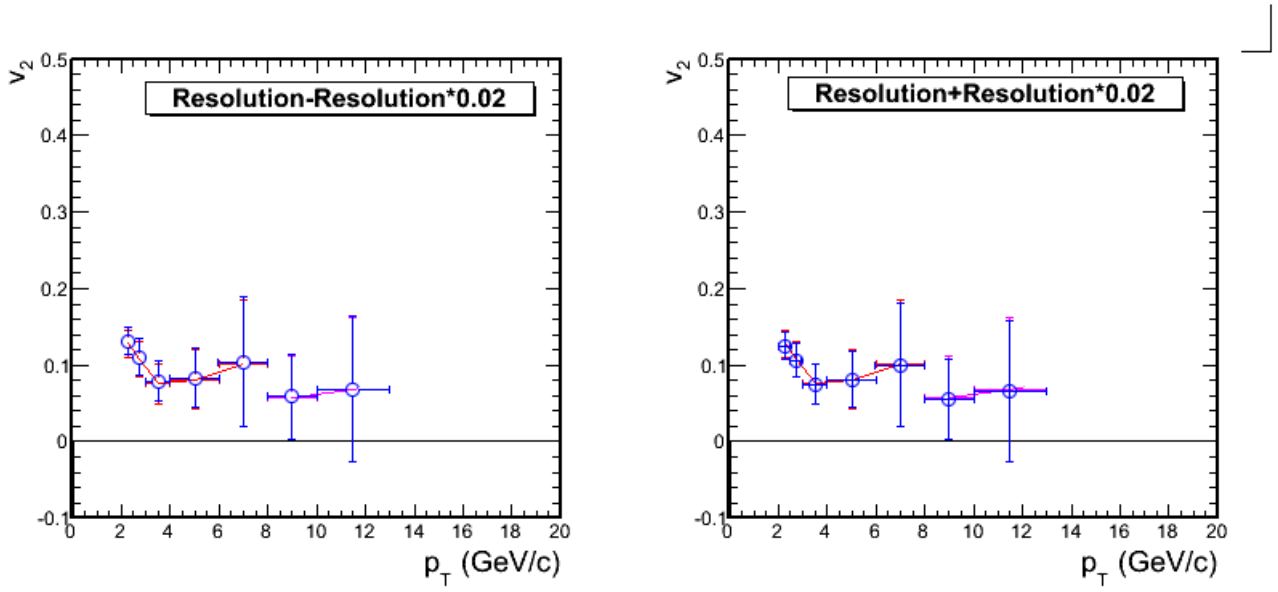

Figure 7.32.: Heavy-flavour electron v_2 as function of p_T in 20-40% central Pb-Pb collisions at $\sqrt{s_{NN}}$ = 2.76 TeV with the variation of the correction for the event plane resolution. Blue points correspond to the measured v_2 after variation.

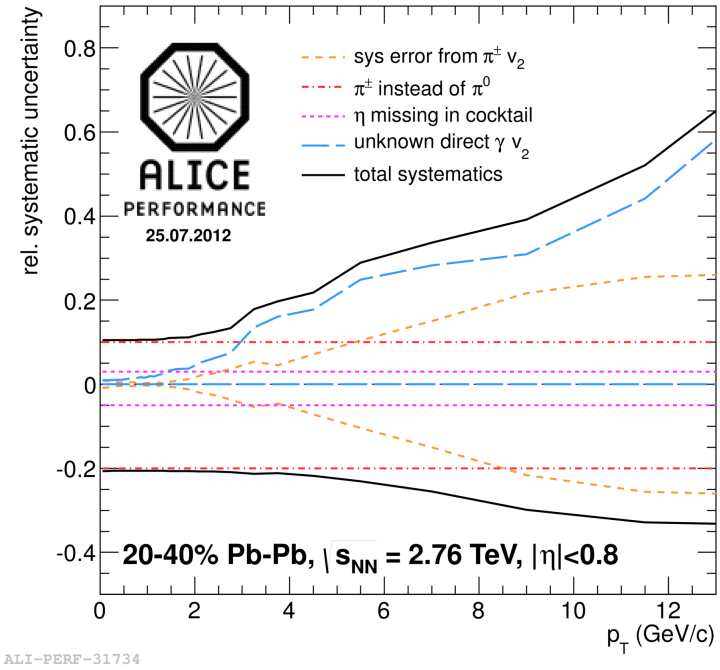

Figure 7.33.: Systematic uncertainty of the background electron v_2 in 20-40% central Pb-Pb collisions at $\sqrt{s_{NN}}$ = 2.76 TeV evaluated with the cocktail method [107].

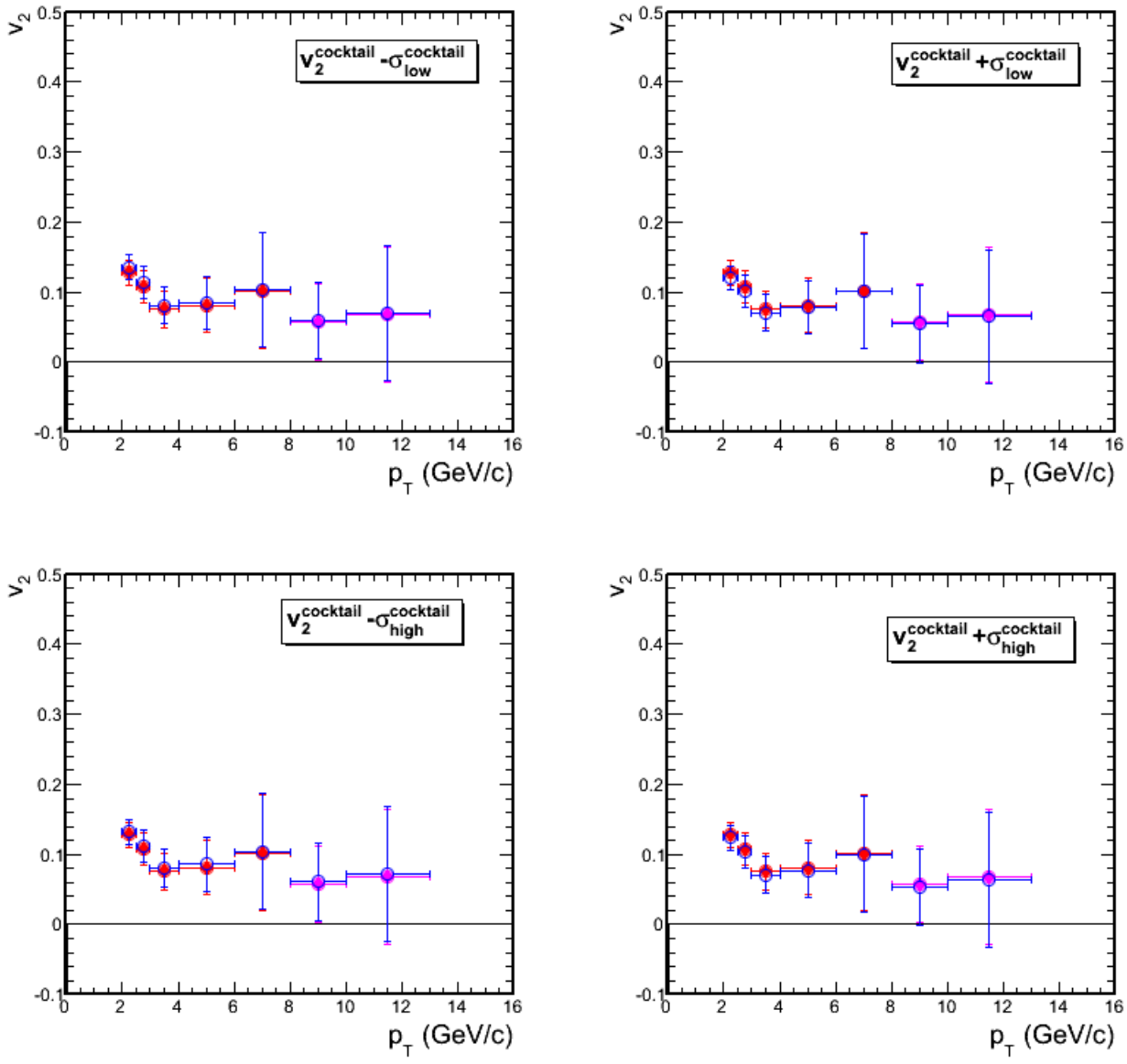

Figure 7.34.: Heavy-flavour electron v_2 as function of p_T in 20-40% central Pb-Pb collisions at $\sqrt{s_{NN}}$ = 2.76 TeV with the variation of the cocktail. Blue points correspond to the measured v_2 after variation.

The variations (see Table 7.9), which are considered constant in p_T range in order to disregard fluctuations due to statistics, are added in quadrature to obtain final systematic uncertainty.

Sources	Variation
E/p cut	10%
TPC σ cut	10%
Hadron contamination	3%
R parameter	12%
Event plane resolution	2%
Correction for trigger non-flow contribution (EMCal trigger)	12%
Centrality (semi-central trigger)	5%
Centrality (EMCal trigger)	2%
Cocktail	9%

Table 7.9.: Systematic uncertainties of the heavy-flavour electron v_2 as function of p_T measurement in 20-40% central Pb-Pb collisions at $\sqrt{s_{NN}}$ = 2.76 TeV.

7.9. v_2 of electrons from charm decays

The elliptic azimuthal anisotropy of electrons from charm decays in 30-50% central Pb-Pb collisions at $\sqrt{s_{\mathrm{NN}}}$ = 2.76 TeV is obtained from the elliptic azimuthal anisotropy of D mesons from charm decays, called prompt D meson, measured in the same centrality class (see Fig. 4.9) and hadronic charm simulation performed with Hijing 2012 and Geant 3.

The simulation used in this analysis contains enhancement of D mesons that biases the spectrum of electrons from D meson decays. The same procedure used to scale the spectrum of electrons from π^0 and η decays is applied to obtain the weight of the D meson p_T distribution (Eq. 7.5) and scale the spectrum of electrons from D meson decays.

Figure 7.35 shows the simulation of the p_T distribution of the total, generated and enhanced samples of D mesons (D^0, $D^{\pm}$ and integrated D meson species) in 30-50% and central Pb-Pb collisions at $\sqrt{s_{NN}}$ = 2.76 TeV.

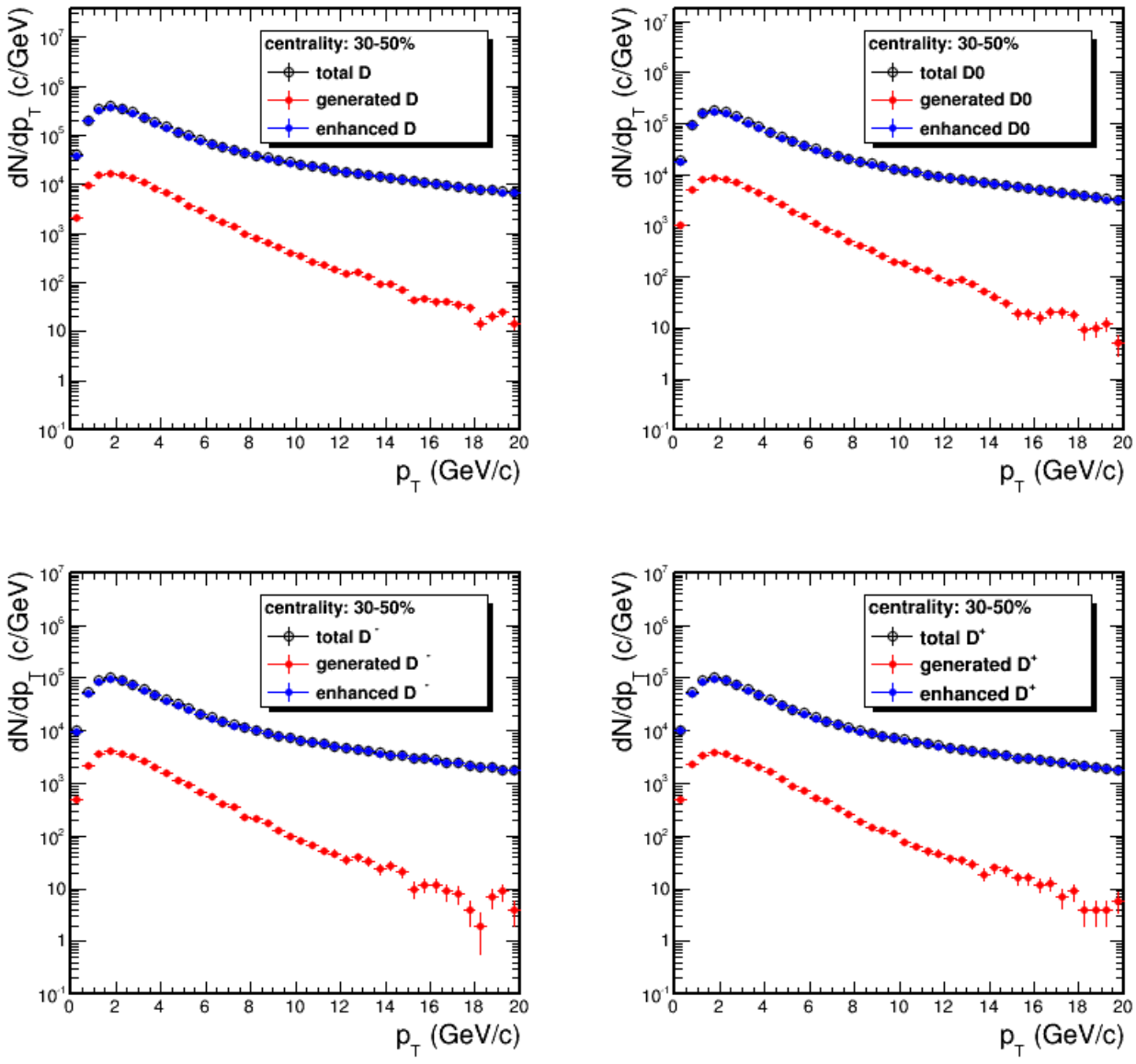

Figure 7.35.: Simulation of the D meson (D^0, $D^{\pm}$ and integrated D meson species) yield in 30-50% central Pb-Pb collisions at $\sqrt{s_{\rm NN}}$ = 2.76 TeV. Total, generated and enhanced samples of D mesons are shown.

Figure 7.36 shows the weight of D meson decays in 30-50% central Pb-Pb collisions at $\sqrt{s_{\rm NN}}$ = 2.76 TeV. The weight is parametrized by a Landau distribution (Eq. 7.8), which describes well the data.

$$\text{D meson weight}(p_T) = k\,\text{Landau}(MPV,\sigma)\ , \tag{7.8}$$

where k is the amplitude of the distribution, MPV is the most probable value and σ is a scale parameter. The parameters obtained from the fits shown in Fig. 7.36 are listed in Table 7.10.

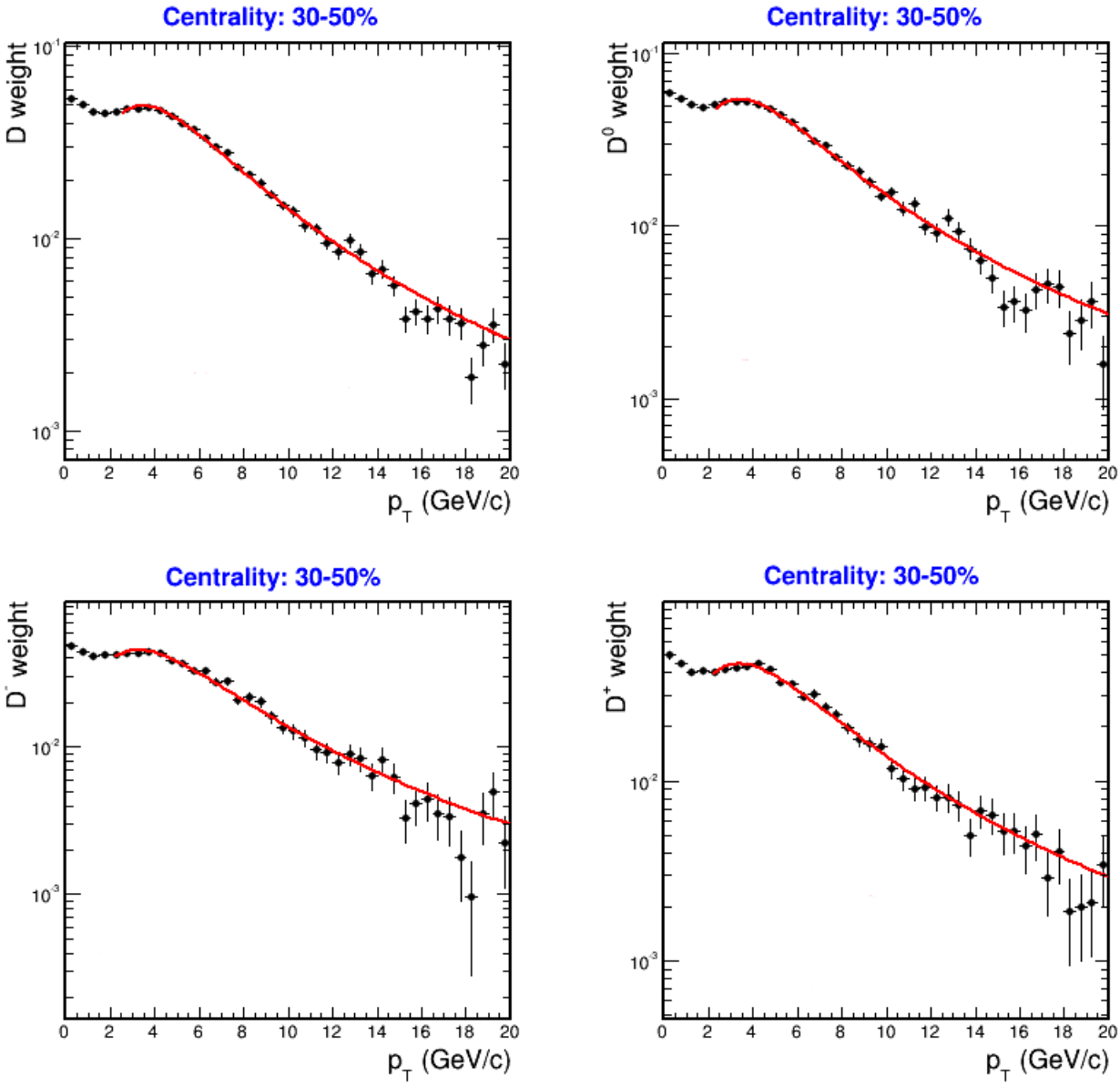

Figure 7.36.: Weights of the D meson (D^0, $D^\pm$ and integrated D meson species) decays in 30-50% central Pb-Pb collisions at $\sqrt{s_{\mathrm{NN}}}$ = 2.76 TeV.

meson	χ^2/NDF	k	MPV	σ
D	1.9	0.2716 ± 0.0014	3.807 ± 0.033	1.537 ± 0.019
D^0	1.7	0.3008 ± 0.0021	3.726 ± 0.048	1.497 ± 0.025
D^-	1.8	0.2494 ± 0.0023	3.611 ± 0.052	1.632 ± 0.035
D^+	1.4	0.2473 ± 0.0024	3.747 ± 0.045	1.608 ± 0.034

Table 7.10.: Values of the parameters obtained from the fits shown in Fig. 7.36.

The D weight (Eq. 7.8) with the parameters of the D meson shown in Table 7.10 is used to scale the spectrum of electron from D meson decays. $D^{*\pm}$ decay channels are not taken into account in the weight procedure, since $D^{*\pm}$ mesons decay into D^0 and $D^{\pm}$ mesons.

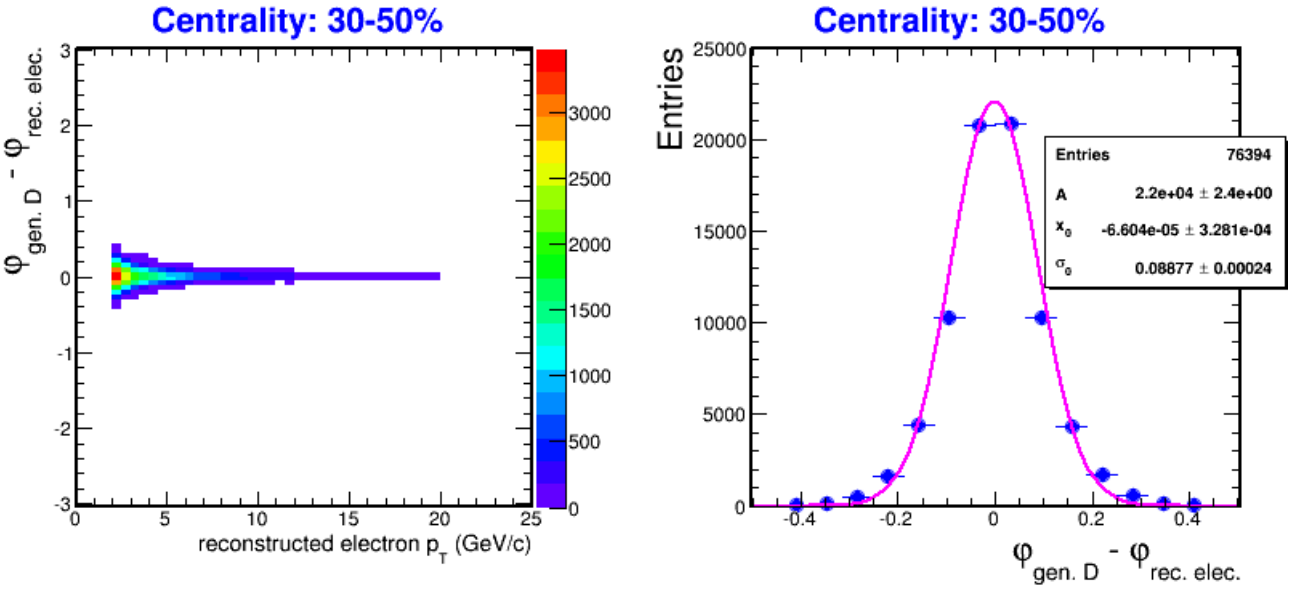

Figure 7.37.: Left panel: Difference between the azimuthal angle of the generated D meson and the azimuthal angle of the reconstructed electron from D meson decays as a function of the reconstructed electron p_T in 30-50% central Pb-Pb collisions at $\sqrt{s_{\rm NN}}$ = 2.76 TeV. Right panel: Projection of the azimuthal angle deviation integrated in transverse momentum.

The left panel of Fig. 7.37 shows the difference between the azimuthal angle of the generated D meson and the azimuthal angle of the reconstructed electron from D meson decays as a function of the reconstructed electron p_T in 30-50% central Pb-Pb collisions at $\sqrt{s_{\rm NN}}$ = 2.76 TeV. It is observed that the deviation is small and decreases with the transverse momentum of the reconstructed electrons. The right panel of 7.37 shows the projection of the azimuthal angle deviation integrated in transverse momentum. A Gaussian function is used to obtain the width of the distribution in order to quantify the deviation. The deviation obtained from the fit, which is approximately 0.089, corresponds to the highest value.

Therefore the cosine of the deviation of approximately 99.7% of the electrons ($\cos(3\sigma_0)$) is 0.965. Based on this observation, it is assumed that the deviation between D meson and electron from D meson decays is negligible:

$$\langle cos[2(\varphi_{e\leftarrow D} - \Psi)]\rangle = \langle cos[2(\varphi_D - \Psi)]\rangle. \tag{7.9}$$

Therefore the elliptic azimuthal anisotropy of D mesons and electrons from D meson decays can be considered to be the same, but with different transverse momentum, since electrons carry a fraction of the D meson p_T:

$$v_2^{e\leftarrow D}(elec.\ p_T) = v_2^D(D\ p_T)\ . \tag{7.10}$$

Consider D mesons with transverse momentum p_2, p_3, and so on, that decay into electrons with transverse momentum p_1. The azimuthal distribution of the electrons is given by:

$$\frac{dN^{e(p_1)}}{d\Delta\varphi} = \frac{dN^{e(p_1)\leftarrow D(p_2)}}{d\Delta\varphi} + \frac{dN^{e(p_1)\leftarrow D(p_3)}}{d\Delta\varphi} + \dots\ . \tag{7.11}$$

If it is assumed that the second harmonic v_2 is the dominant term in the Fourier series:

$$\frac{dN}{d\Delta\varphi} = k[1 + 2v_2\cos(2\Delta\varphi)]\ , \tag{7.12}$$

which is valid in non-central collisions, the v_2 of the electrons is given by:

$$v_2^{e(p_1)} = \frac{N^{e(p_1)\leftarrow D(p_2)}v_2^{e(p_1)} + N^{e(p_1)\leftarrow D(p_3)}v_2^{e(p_1)} + \dots}{N^{e(p_1)}}\ . \tag{7.13}$$

According to the Eq. 7.10, Equation 7.13 can be expressed as:

$$v_2^{e(p_1)} = \frac{N^{e(p_1)\leftarrow D(p_2)}v_2^{D(p_2)} + N^{e(p_1)\leftarrow D(p_3)}v_2^{D(p_3)} + \dots}{N^{e(p_1)}}\ , \tag{7.14}$$

where v_2^D is the measured elliptic azimuthal anisotropy of prompt D meson shown in Fig. 4.9, and N^e, which corresponds to the number of electrons in different p_T intervals from D meson decays in different p_T ranges, is shown in Fig. 7.38.

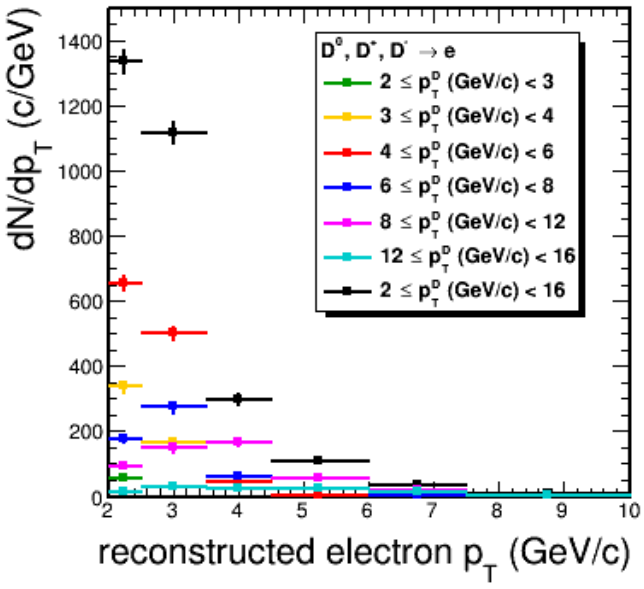

Figure 7.38.: Number of electrons in different p_T intervals from D meson decays in different p_T ranges. The simulation is performed in 30-50% central Pb-Pb collisions at $\sqrt{s_{\mathrm{NN}}}$ = 2.76 TeV.

Figure 7.38 shows the comparison of elliptic azimuthal anisotropy of electrons from heavy-flavour decays and preliminary measurement of the electrons from charm decays in 30-50% central Pb-Pb collisions at $\sqrt{s_{\mathrm{NN}}}$ = 2.76 TeV.

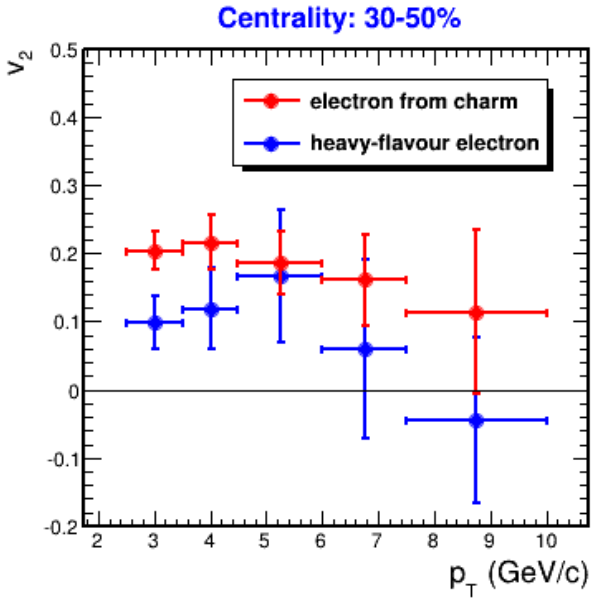

Figure 7.39.: Comparison of elliptic azimuthal anisotropy of electrons from heavy-flavour decays and preliminary measurement of the electrons from charm decays in 30-50% central Pb-Pb collisions at $\sqrt{s_{\mathrm{NN}}}$ = 2.76 TeV.

7.10. v_2 of electrons from beauty decays

Heavy-flavour electrons are composed by electrons from charm decays and electrons from beauty decays. Therefore the azimuthal distribution of heavy-flavour electrons is given by:

$$\frac{dN^{HFE}}{d\Delta\varphi} = \frac{dN^{e\leftarrow c}}{d\Delta\varphi} + \frac{dN^{e\leftarrow b}}{d\Delta\varphi} \,, \tag{7.15}$$

where N^{HFE} is the number of heavy-flavour electrons, $N^{e\leftarrow c}$ is the number of electrons from charm decays, and $N^{e\leftarrow b}$ is the number of electrons from beauty decays.

If it is assumed that the second harmonic v_2 is the dominant term in the Fourier series, the elliptic azimuthal anisotropy of electrons from beauty is expressed as:

$$v_2^{e\leftarrow b} = \frac{v_2^{HFE} - (1-R)v_2^{e\leftarrow c}}{R} \,, \tag{7.16}$$

where v_2^{HFE} is the elliptic azimuthal anisotropy of electrons from heavy flavour decays, $v_2^{e\leftarrow c}$ is the elliptic azimuthal anisotropy of electrons from charm decays, and R is the electron from beauty decay to heavy-flavour electron ratio. The current measurement of electron from beauty decays to heavy-flavour electron ratio is performed only in pp collisions at $\sqrt{s}$ = 2.76 TeV, as show in Fig 3.5.

The electron from beauty decay to heavy-flavour electron ratio is expected to be higher in Pb-Pb collisions than in pp collisions, since the energy loss of charm is larger than the energy loss of beauty in the medium created in heavy-ion collisions at high energy according to theoretical predictions (see Fig. 3.4). However, the minimum value of the ratio is the one obtained in pp collisions, since there is no quark energy loss in the medium, and the maximum value of the ratio must be 1. In this case, the v_2 of electron from beauty decays is equal to v_2 of electrons from heavy-flavour decays (see Eq. 7.16).

Therefore it is possible evaluate only the range of the v_2 of electrons from beauty decays with the current measurements. Figure 7.40 shows the preliminary measurement of the range of the elliptic azimuthal anisotropy of electrons from beauty decays in 30-50% central Pb-Pb collisions at $\sqrt{s_{\rm NN}}$ = 2.76 TeV.

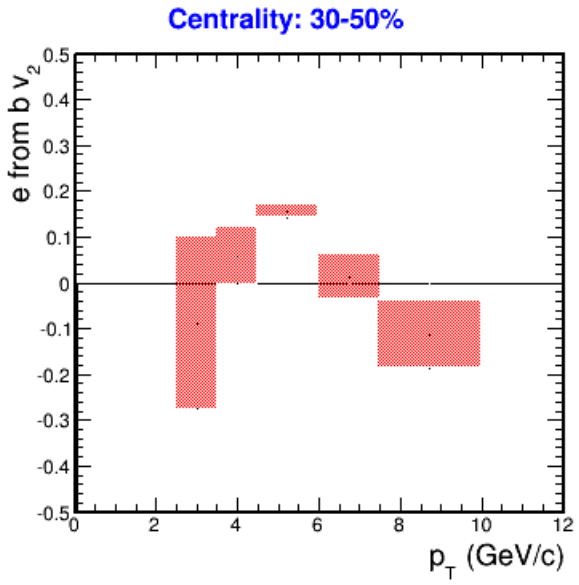

Figure 7.40.: Preliminary measurement of the range of the elliptic azimuthal anisotropy of electrons from beauty decays in 30-50% central Pb-Pb collisions at $\sqrt{s_{\mathrm{NN}}} = 2.76$ TeV. Statistical and systematic uncertainties are not shown.

8

Discussions

Figure 8.1 shows the elliptic azimuthal anisotropy of inclusive electrons in 20-40% central Pb-Pb collisions at $\sqrt{s_{NN}}$ = 2.76 TeV compared with the elliptic azimuthal anisotropy of background electrons estimated with the cocktail method. At low transverse momentum, the estimated non-heavy flavour electron v_2 is larger than the measured inclusive electron v_2, whereas at high transverse momentum, v_2 of inclusive electrons and non-heavy flavour electrons are similar.

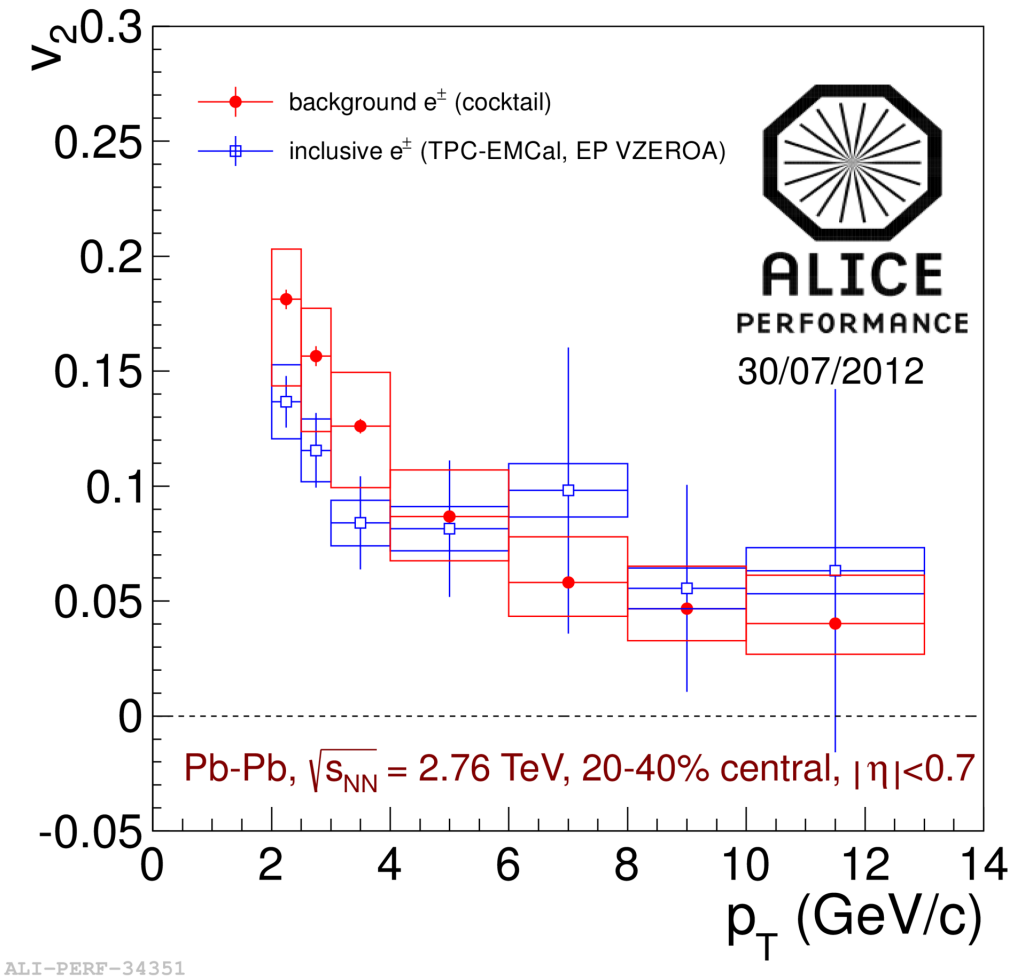

Figure 8.1.: Elliptic azimuthal anisotropy of inclusive electrons in 20-40% central Pb-Pb collisions at $\sqrt{s_{NN}}$ = 2.76 TeV compared with the elliptic azimuthal anisotropy of background electrons estimated with the cocktail method. Vertical error bars are the statistical uncertainties, horizontal error bars indicate the bin widths, and empty boxes are the total systematic uncertainties.

The measurement of the elliptic azimuthal anisotropy of electrons from heavy-flavour decays in 20-40% central Pb-Pb collisions at $\sqrt{s_{NN}}$ = 2.76 TeV is shown in Fig. 8.2. Another measurement of the heavy-flavour electron to background electron ratio is used to obtain this result, but it is compatible with the ratio shown in Fig. 7.25. The background electron v_2 is subtracted from the inclusive electron v_2 according to the equation 4.43.

The measurement is compared with another ALICE result, in which inclusive electrons are identified with the TPC and TOF detectors and the v_2 harmonic is obtained from the $\langle\cos(2\Delta\varphi)\rangle$ measurement. The final result is the weighted mean of both measurements in the common p_T range. The measured v_2 is larger than zero at low p_T , in particular with more than 3σ significance in the range 2 < pT < 3

GeV/c, which indicates that heavy quarks (charm and beauty) participate in the collective motion of the medium. The contribution from charm decays is dominant in the measured yield of heavy-flavour decay electrons at low p_T in pp collisions (see Figure 3.5).

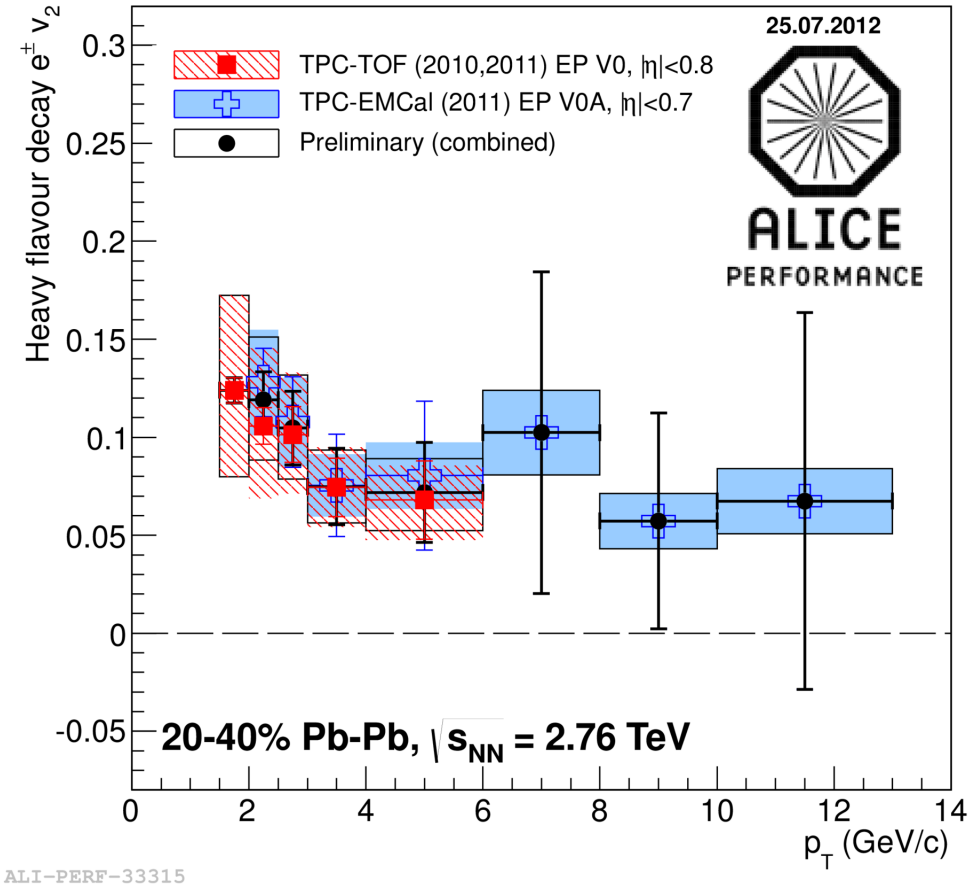

Figure 8.2.: Elliptic azimuthal anisotropy of electrons after subtraction of the background electrons estimated with the cocktail method in 20-40% central Pb-Pb collisions at $\sqrt{s_{NN}}$ = 2.76 TeV. Vertical error bars are the statistical uncertainties, horizontal error bars indicate the bin widths, and empty boxes are the total systematic uncertainties.

Figure 8.3 shows the elliptic azimuthal anisotropy of electrons from heavy-flavour decays in 20-40% Pb-Pb collisions at $\sqrt{s_{NN}}$ = 2.76 TeV. The measurement is compatible within uncertainties with previous measurement in Au-Au collisions at $\sqrt{s_{NN}}$ = 0.2 TeV at RHIC. Theoretical predictions of heavy-quark transport in the medium are compared with the measurement:

- Uphoff et al. [41]: heavy-quark transport model is calculated with a Boltzmann approach to multi-parton scattering (BAMPS). The Boltzmann equation is solved for on-shell partons and pQCD interactions.

- R. Rapp et al. [42]: heavy-quark transport model based on in-medium resonance scattering and coalescence.
- M. Monteno et al. [43]: heavy-quark propagation in the QGP is described with a relativistic Langevin equation. The interaction of the heavy quarks is calculated with pQCD calculations with resummation of medium effects.
- J. Aichelin at al. [44]: heavy-quark transport model based on collisional mechanisms.

The BAMPS model describes well the measured elliptic azimuthal anisotropy of electrons from heavy-flavour decays in all p_T interval, and other theoretical predictions are systematically lower than the measured v_2, however they are compatible with the result due to the high systematic uncertainty at low transverse momentum.

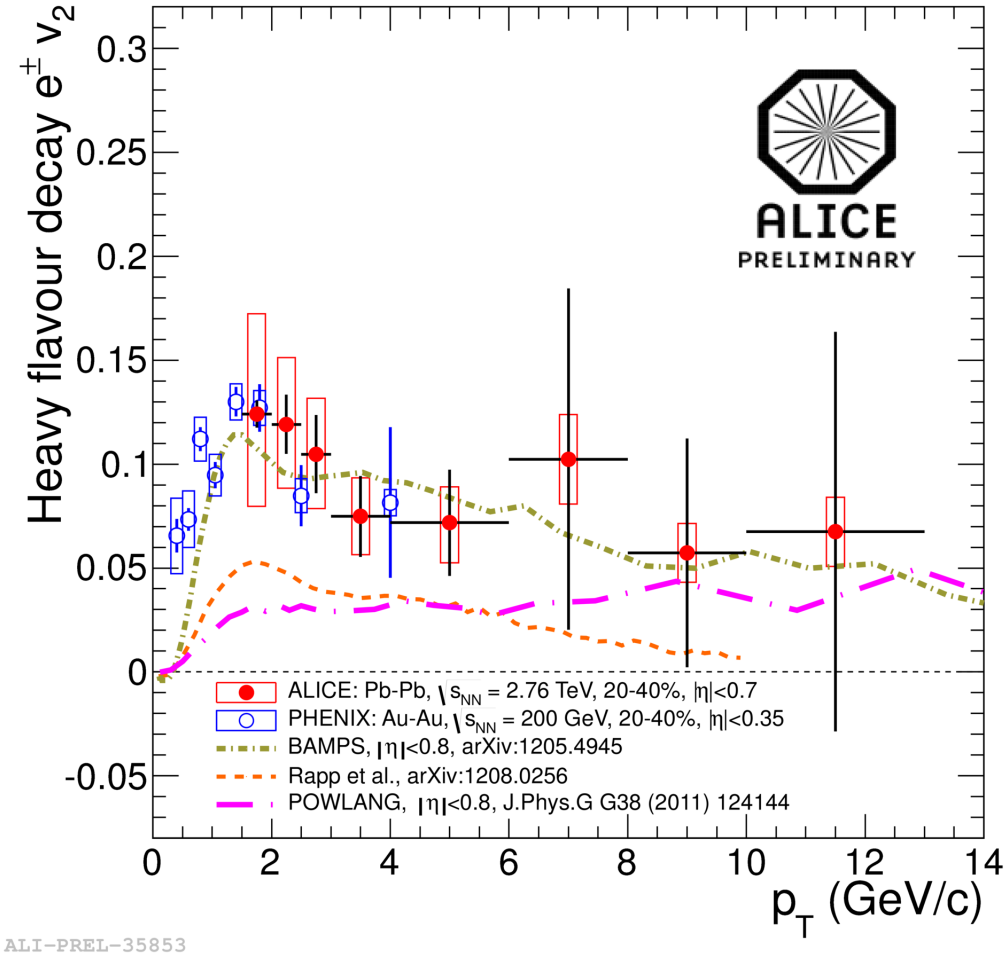

Figure 8.3.: Elliptic azimuthal anisotropy of electrons from heavy-flavour decays in 20-40% Pb-Pb collisions at $\sqrt{s_{NN}}$ = 2.76 TeV. Result is compared with theoretical predictions [41, 42, 43, 44], and previous measurement in Au-Au collisions at $\sqrt{s_{NN}}$ = 0.2 TeV at RHIC.

Results from theoretical model calculations [41, 42, 43, 44] are compared simultaneously with the measured nuclear modification factor (Eq. 2.11) and elliptic azimuthal anisotropy of electrons from heavy-flavour decays. The left panel of Fig. 8.4 shows the R_{AA} of electrons from heavy-flavour decays as a function of p_T in the range $3 < p_{\mathrm{T}} < 18$ GeV/c at mid-rapidity ($|\eta| < 0.6$) in 0-10% centrality class. The observed suppression of the heavy-flavour decay electron yield at high p_T is understood as predominantly due to parton in-medium energy loss, which results in a modification of the momentum spectra of D and B mesons in Pb-Pb collisions relative to pp collisions.

The theoretical models can describe the data within the uncertainties, but the simultaneous description of R_{AA} and v_2 of heavy-flavour decay electrons is challenging. The BAMPS and "Collisional + LPM radiation" models describe well the result of the elliptic azimuthal anisotropy of electrons from heavy flavou decays in all p_T interval, but and they are systematically lower than the measured nuclear modification factor. On the other hand, the model calculated by Rapp et al. and the POWLANG model are systematically lower than the measured elliptic azimuthal anisotropy of electrons from heavy flavour decays, but they describe well the R_{AA} result, specially at low trasnverse momentum.

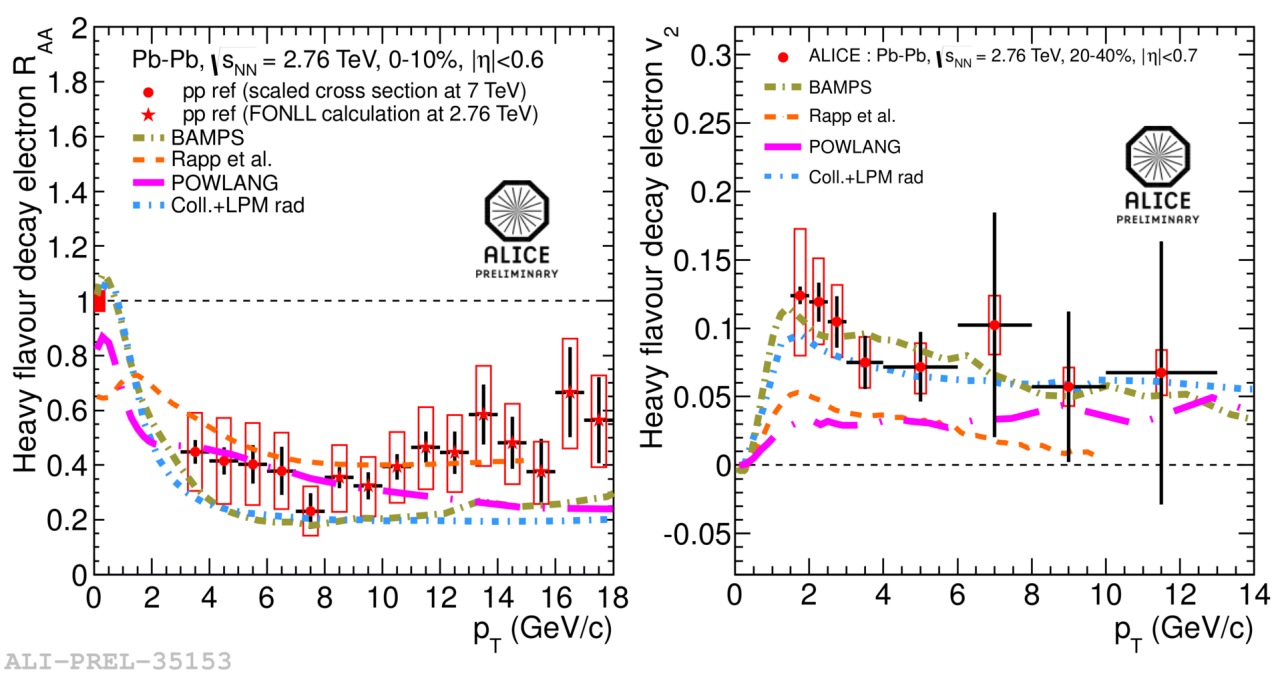

Figure 8.4.: R_{AA} and v_2 of electrons from heavy-flavour electron decays as a function of p_{T} in the 0-10% and 20-40% centrality classes, respectively, in Pb-Pb collisions at $\sqrt{s_{\mathrm{NN}}} = 2.76$ TeV. Results are compared to theoretical predictions [41, 42, 43, 44]. Vertical error bars are the statistical uncertainties, horizontal error bars indicate the bin widths and empty boxes are the total systematic uncertainties. The filled box centered at $R_{\mathrm{AA}} = 1$ depicts the normalization uncertainty.

Figure 8.5 shows the comparison of the elliptic azimuthal anisotropy in 20-40% and 30-50% centrality classes in Pb-Pb collisions at $\sqrt{s_{NN}}$ = 2.76 TeV. The centrality dependence is observed, but not conclusive within the current uncertainties.

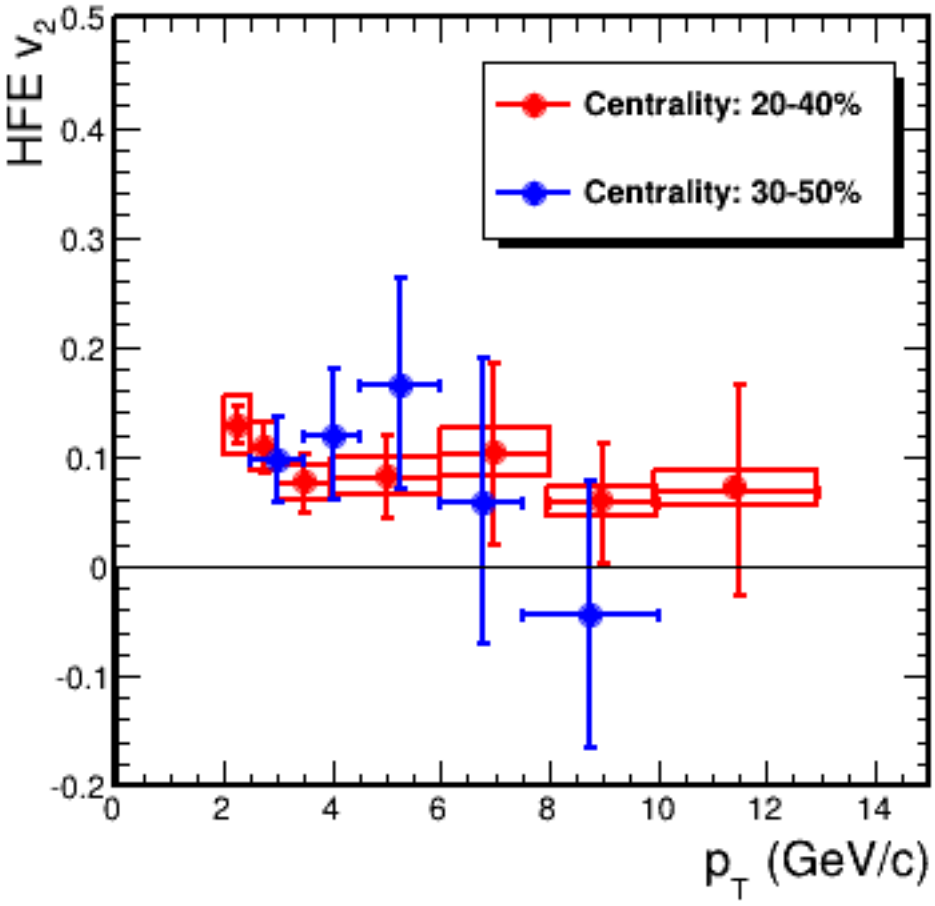

Figure 8.5.: Comparison of the elliptic azimuthal anisotropy in 20-40% and 30-50% centrality classes in Pb-Pb collisions at $\sqrt{s_{NN}}$ = 2.76 TeV.

Figure 8.6 shows the preliminary measurement of the elliptic azimuthal anisotropy of prompt D mesons in 30-50% central Pb-Pb collisions at $\sqrt{s_{NN}}$ = 2.76 TeV compared with the preliminary result of electrons from charm decays. Monte Carlo simulation and the measured elliptic azimuthal anisotropy of prompt D mesons are used to obtain the elliptic azimuthal anisotropy of electrons from charm decays. It is assumed that v_2 of electrons from charm decays and v_2 prompt D mesons are the same but in different p_T interval.

Figure 8.7 shows the elliptic azimuthal anisotropy of heavy-flavour electron decays (charm and beauty)

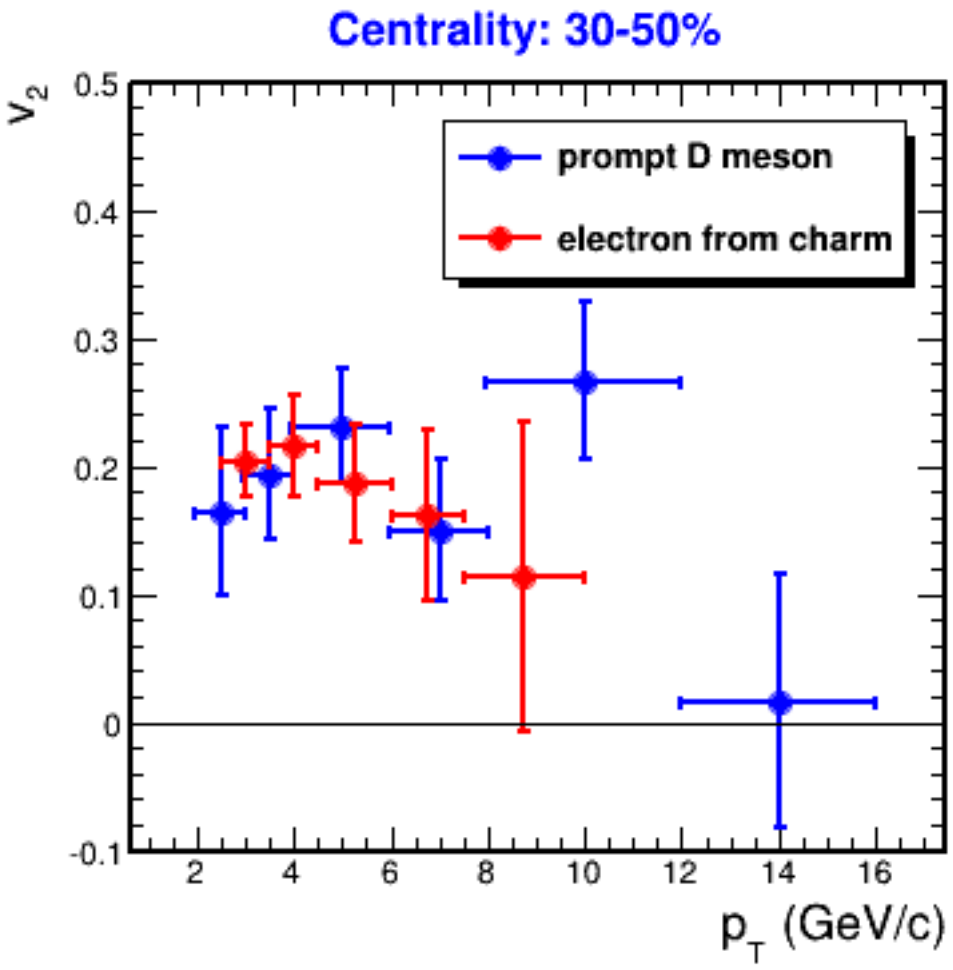

Figure 8.6.: Preliminary measurement of the elliptic azimuthal anisotropy of prompt D mesons and electrons from charm decays and in 30-50% central Pb-Pb collisions at $\sqrt{s_{NN}}$ = 2.76 TeV.

in 30-50% central Pb-Pb collisions at $\sqrt{s_{NN}}$ = 2.76 TeV compared with preliminary results of the elliptic azimuthal anisotropy of electrons from charm decays, and the minimum value of electrons from beauty decays, which is obtained with the electron from beauty decay to heavy-flavour electron ratio measured in pp collisions. The maximum value of the v_2 of electrons from beauty decays corresponds to the measured v_2 of heavy-flavour electron decays. It is observed the $v_2^{e\leftarrow b} \leq v_2^{HFE} < v_2^{e\leftarrow c}$ dependence, but not conclusive within the current uncertainties.

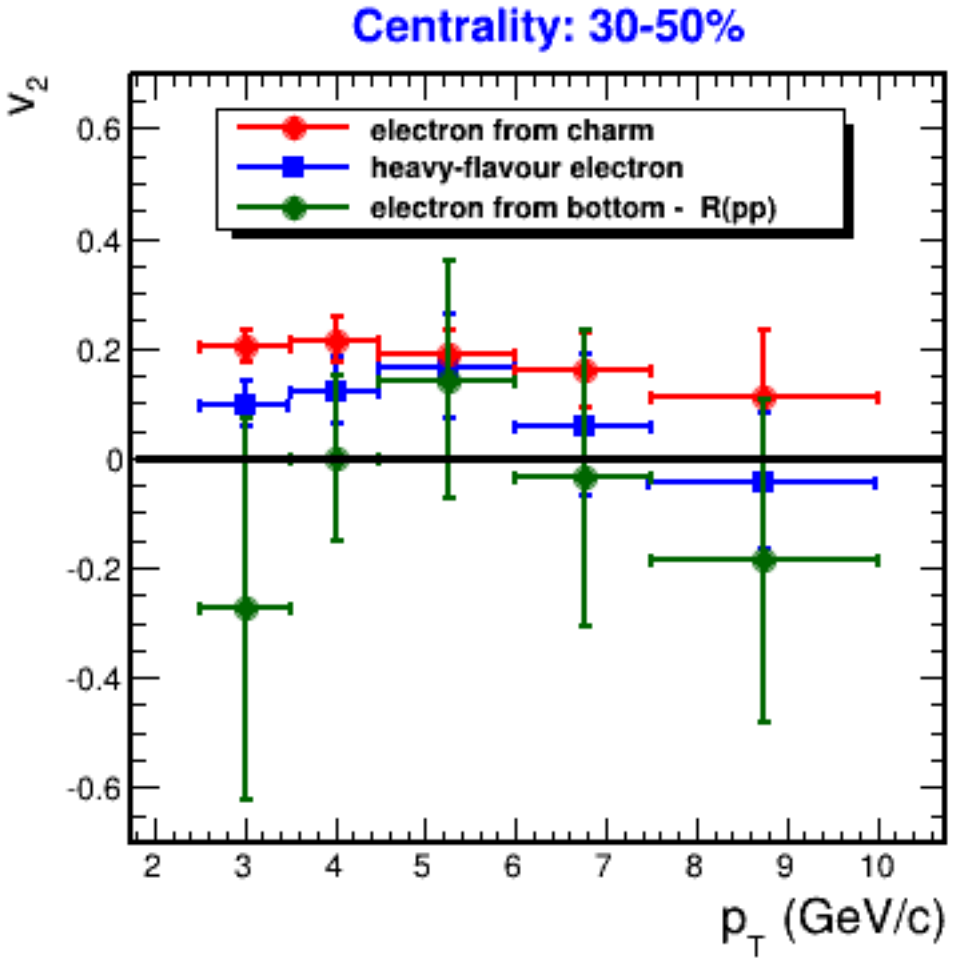

Figure 8.7.: Preliminary measurement of the elliptic azimuthal anisotropy of heavy-flavour electron decays (charm and beauty), electron from charm decays, and minimum value of the electron from beauty decays in 30-50% central Pb-Pb collisions at $\sqrt{s_{NN}}$ = 2.76 TeV.

9

Conclusions

The focus of this thesis is the measurement of the elliptic azimuthal anisotropy of electrons from heavy flavour decays. The v_2 observable is sensitive to the initial geometry of the heavy-ion collisions and can be connected to the properties of the created medium via hydrodynamics. The measurement of the elliptic azimuthal anisotropy of electrons from heavy-flavour decays at low transverse momentum provides a way to test whether heavy quarks take part in the collective expansion of the medium. Whereas, the elliptic azimuthal anisotropy of electrons from heavy-flavour decays at high transverse momentum is interpreted as a path length dependence of heavy-quark energy loss within the created dense medium.

The elliptic azimuthal anisotropy of heavy-flavour decay electrons has been measured as a function of the transverse momentum at mid-rapidity ($|\eta| < 0.7$) in 20-40% central Pb-Pb collisions at $\sqrt{s_{\rm NN}}$ = 2.76 TeV with ALICE. The measured heavy-flavour decay electron v_2 is larger than zero at low p_T, with more than 3σ significance in the range $2 < p_{\rm T} < 3$ GeV/c, which indicates collective motion of heavy quarks (charm and beauty) in the QGP. The charm decay contribution is dominant in the measured yield of heavy-flavour decay electrons at low $p_{\rm T}$ in pp collisions. The simultaneous description of $R_{\rm AA}$

and v_2 of heavy-flavour decay electrons presents a challenge for theoretical predictions of heavy-quark transport in the QGP.

Previous measurement of the elliptic azimuthal anisotropy of prompt D mesons in 30-50% central Pb-Pb collisions at $\sqrt{s_{\rm NN}}$ = 2.76 TeV and Monte Carlo simulation performed with Hijing and Geant are used to obtain a preliminary measurement of the elliptic azimuthal anisotropy of electrons from charm decays in 30-50% central Pb-Pb collisions at $\sqrt{s_{\rm NN}}$ = 2.76 TeV. Based on the observation that the deviation between electrons from D meson decays and D mesons is negiblible, it is assumed that electrons from prompt D mesons have the same v_2 magnitude as the prompt D mesons, but in different p_T interval, since electrons carry a fraction of the D meson total momentum.

The range of the elliptic azimuthal anisotropy of electrons from beauty decays in 30-50% central Pb-Pb collisions at $\sqrt{s_{\rm NN}}$ = 2.76 TeV is obtained from the measurement of the electron from beauty decays to electron from heavy-flavour decay (charm and beauty) ratio in pp collisions at $\sqrt{s}$ = 2.76 TeV and the measurements of v_2 of heavy-flavour electrons and v_2 of electrons from charm decays in 30-50% central Pb-Pb collisions at $\sqrt{s_{\rm NN}}$ = 2.76 TeV. The magnitude of the elliptic azimuthal anisotropy of electrons from beauty decays can not be obtained with the current measurements, since the electron from beauty decays to electron from heavy-flavour decay ratio is measured only in pp collisions. It is observed the $v_2^{e\leftarrow b} \leq v_2^{HFE} < v_2^{e\leftarrow c}$ dependence, but not conclusive within the current uncertainties.

A

Glossary

ACORDE: A Cosmic Ray Detector

ALICE: A Large Ion Collider Experiment

ATLAS: A Toroidal LHC Apparatus

CERN: the European Organization for Nuclear Research

CMS: Compact Muon Solenoid

DIS: Deep Inelastic Scattering

EMCal: Electromagnetic Calorimeter

EP: Event Plane

ESD: Event Summary Data

FMD: Forward Multiplicity Detector

HMPID: High-Momentum Particle Identification Detector

ITS: Inner Tracking System

LHC: Large Hadron Collider

LHCb: Large Hadron Collider beauty

LINAC: Linear Accelerator

LO: Leading Order

MC: Monte Carlo

NLO: Next to Leading Order

PHOS: Photon Spectrometer

PID: Particle Identification

PMD: Photon Multiplicity Detector

pQCD: perturbative Quantum Chromodynamics

PS: Proton Synchrotron

PSB: Proton Synchrotron Booster

QCD: Quantum Chromodynamics

QGP: Quark-Gluon Plasma

RHIC: Relativistic Heavy-Ion Collider

RP: Reaction Plane

SDD: Silicon Drift Detector

SLAC: Stanford Linear Accelerator Center

SPD: Silicon Pixel Detector

SPS: Super Proton Synchrotron

SSD: Silicon Strip Detector

TOF: Time of Flight

TPC: Time-Projection Chamber

TRD: Transition-Radiation Detector

ZDC: Zero-Degree Calorimeter

B

Appendix

B.1. Kinematic variables

Two convenient variables are used to describe the kinematic of the particles in nucleus-nucleus collisions at high energy: rapidity (y) and pseudorapidity (η).

The rapidity is defined as:

$$y \equiv \frac{1}{2} \ln \left(\frac{E + p_z}{E - p_z} \right) , \tag{B.1}$$

where $E = \sqrt{p^2 + m^2}$ is the energy of the particle, and p_z is the component of the total momentum of the particle in the beam direction. The term "mid-rapidity" is related to the case $y \approx 0$, i.e. when $p_z \approx 0$. Backward and forward rapidies correspond, respectively, to negative and positive high values of rapidity.

This is an useful variable, since the rapidities of two particles in different frame references differ by a constant.

The pseudorapidity is defined as:

$$\eta \equiv \frac{1}{2} \ln \left(\frac{p + p_z}{p - p_z} \right) , \tag{B.2}$$

where p is the magnitude of the total momentum of the particle. $\eta \approx y$ at high transverse momentum of the particle.

The pseudorapidity can also be expressed as:

$$\eta \equiv - \ln \left(\tan \frac{\theta}{2} \right) , \tag{B.3}$$

where θ is the angle of the particle with respect to the beam axis.

B.2. Data sample and Monte Carlo productions

The results shown in this thesis are obtained from a data sample (LHC11h_pass2) of Pb-Pb collisions at $\sqrt{s_{NN}}$ = 2.76 TeV collected in 2011. The list of runs is presented below.

168311, 169035, 169475, 169965, 170268, 168322, 169044, 169498, 170027, 170269, 168325, 169091, 169504, 170040, 170270, 168341, 169094, 169512, 170081, 170306, 168342, 169099, 169550, 170083, 170308, 168361, 169138, 169554, 170084, 170309, 168362, 169144, 169557, 170085, 170311, 168458, 169145, 169586, 170088, 170312, 168460, 169148, 169588, 170089, 170313, 168464, 169156, 169591, 170091, 170315, 168467, 169160, 169835, 170155, 170387, 168511, 169167, 169837, 170159, 170388, 168512, 169238, 169838, 170163, 170572, 168514, 169411, 169846, 170193, 170593, 168777, 169415, 169855, 170203, 168826, 169417, 169858, 170204, 168988, 169418, 169859, 170228, 168992, 169419, 169923, 170230.

The results from Monte Carlo are obtained from two productions of a hadronic charm simulation (LHC12a17e_label_fix, and LHC12a17b) with Hijing 2012 and Geant 3 in Pb-Pb collisions at $\sqrt{s_{NN}}$ = 2.76 TeV. The anchor runs are listed below:

LHC12a17b production:
170593, 170572, 170388, 170387, 170315, 170313, 170312, 170311, 170309, 170308, 170306, 170270,

170269, 170268, 170230, 170228, 170204, 170203, 170193, 170163, 170159, 170155, 170091, 170089, 170088, 170085, 170084, 170083, 170081, 170040, 170027, 169965, 169923, 169859, 169858, 169855, 169846, 169838, 169837, 169835, 169591, 169588, 169586, 169557, 169554, 169550, 169512, 169504, 169498, 169475, 169419, 169418, 169417, 169415, 169411, 169238, 169167, 169160, 169156, 169148, 169145, 169144, 169138, 169099, 169094, 169091, 169044, 169035, 168992, 168988, 168826, 168777, 168514, 168512, 168511, 168467, 168464, 168460, 168458, 168362, 168361, 168342, 168341, 168325, 168322, 168311.

LHC12a17e_label_fix production:
168311, 168988, 169238, 169555, 170027, 170228, 168322, 168992, 169411, 169557, 170040, 170230, 168325, 169035, 169415, 169586, 170081, 170268, 168341, 169040, 169417, 169587, 170083, 170269, 168342, 169044, 169418, 169588, 170084, 170270, 168361, 169045, 169419, 169590, 170085, 170306, 168362, 169091, 169420, 169591, 170088, 170308, 168458, 169094, 169475, 169835, 170089, 170309, 168460, 169099, 169498, 169837, 170091, 170311, 168464, 169138, 169504, 169838, 170155, 170312, 168467, 169144, 169506, 169846, 170159, 170313, 168511, 169145, 169512, 169855, 170163, 170315, 168512, 169148, 169515, 169858, 170193, 170387, 168514, 169156, 169550, 169859, 170203, 170388, 168777, 169160, 169553, 169923, 170204, 170572, 168826, 169167, 169554, 169965, 170207, 170593.

B.3. Code

The code used in this analysis is implemented in the Aliroot, which is the ALICE offline framework. It can be found in:

$ALIROOT/PWGHF/hfe/AliAnalysisTaskFlowTPCEMCalEP.cxx

Bibliography

[1] D. Griffiths, *Introduction to Elementary particles* (John Wiley and Sons).

[2] A. M. F. Halzen, *Quarks and leptons: an introductory course in Modern Particle Physics* (John Wiley and Sons).

[3] E. S. W. Greiner, S. Schramm, *Quantum Chromodynamics* (Springer).

[4] L. B. Okun, *Leptons and quarks*.

[5] J. E. Dodd, *The ideas of particle physics*.

[6] C. Quigg, *Gauge theories of the strong, weak, eletromagnetic interactions*.

[7] R. G. Roberts, *The structure of the proton*.

[8] J. B. et al., *Particle Data Group* (APS Physics).

[9] A. Pich, *arXiv* **9505231** (1995).

[10] S. Bethke, *Progress in Particle and Nuclear Physics* **58**, 351 (2007).

[11] S. Bethke, *Prog.Part.Nucl.Phys.* **58**, 351 (2007).

[12] E. V. Shuryak, *Physics Reports* **61**, 71 (1980).

[13] P. Braun-Munzinger, *Nucl.Phys.* **A663**, 183 (2000).

[14] R. Hagedorn, *La Rivista del Nuovo Cimento* **6**, 1 (1983).

[15] R. K. Ellis, W. J. Stirling, B. R. Webber, *QCD and collider physics*.

[16] V. D. Barger, R. J. N. Phillips, *Collider physics*.

[17] F. Karsch, *Nucl.Phys.* **A698**, 199 (2002).

[18] F. Karsch, *Nuclear Physics A* **698**, 199 (2002). 15th Int. Conf. on Ultra-Relativistic Nucleus-Nucleus Collisions (Quark Matter 2001).

[19] R. C. Hwa, X. Wang, *Quark-Gluon Plasma*, vol. 3 (Word Scientific, 2004).

[20] J. Adams, *et al.*, *Nuclear Physics A* **757**, 102 (2005). First Three Years of Operation of RHIC.

[21] J.-Y. Ollitrault, *Eur.J.Phys.* **29**, 275 (2008).

[22] T. Hirano, N. van der Kolk, A. Bilandzic, *Lect.Notes Phys.* **785**, 139 (2010).

[23] L. D. Landau, *Izv. Akad. Nauk SSSR Ser. Fiz.* **17**, 51 (1953).

[24] Duke, http://www.phy.duke.edu/research/NPTheory/QGP/transport/index.php (2013).

[25] K. Adcox, *et al.*, *Nucl.Phys.* **A757**, 184 (2005).

[26] J. D. Bjorken, *Phys. Rev. D* **27**, 140 (1983).

[27] J. Adams, *et al.*, *Nucl.Phys.* **A757**, 102 (2005).

[28] C. A. S. et al., *Journal of Physics G: Nuclear and Particle Physics* **39**, 015010 (2012).

[29] *Nuclear Physics B - Proceedings Supplements* **214**, 80 (2011).

[30] D. A. M. de Godoy, *JPCS* **458** (2013).

[31] J. Babcock, D. Sivers, S. Wolfram, *Phys. Rev. D* **18**, 162 (1978).

[32] E. Norrbin, T. Sjöstrand, *The European Physical Journal C - Particles and Fields* **17**, 137 (2000).

[33] M. Cacciari, *et al.*, *JHEP* **1210**, 137 (2012).

[34] E. Norrbin, T. Sjostrand, *Eur.Phys.J.* **C17**, 137 (2000).

[35] J. Babcock, D. W. Sivers, S. Wolfram, *Phys.Rev.* **D18**, 162 (1978).

[36] B. Abelev, *et al.*, *Phys.Rev.* **D86**, 112007 (2012).

[37] *The European Physical Journal C* (2006).

[38] A. Mischke, *hep-ph/1309v4* (2009).

[39] M. Djordjevic, *Phys. G* **32** (2006).

[40] M. Djordjevic, U. Heinz, *arXiv:* **0705.3439** (2007).

[41] Z. X. J. Uphoff, O. Fochler, C. Greiner, *Physics Letters B* **717**, 430 (2012).

[42] M. He, R. J. Fries, R. Rapp, *arXiv:* **1208.0256**.

[43] M. Monteno, *et al.*, *J. Phys. G.* **124144** (2012).

[44] R. B. P. B. Gossiaux, J. Aichelin, *Phys. Rev. C* **79** (2009).

[45] J. Casalderrey-Solana, C. A. Salgado, *Acta Phys.Polon.* **B38**, 3731 (2007).

[46] D. d'Enterria, *arXiv* **0902.2011** (2009).

[47] Y. Mehtar-Tani, C. A. Salgado, K. Tywoniuk, *JHEP* **1204**, 064 (2012).

[48] P. Gossiaux, R. Bierkandt, J. Aichelin, *Phys.Rev.* **C79**, 044906 (2009).

[49] M. Monteno, *et al.*, *J.Phys.* **G38**, 124144 (2011).

[50] M. He, R. J. Fries, R. Rapp, *Nuclear Physics A* **910–911**, 409 (2013). 5th International Conference on Hard and Electromagnetic Probes of High-Energy Nuclear Collisions.

[51] A. Dainese, *Journal of Physics G: Nuclear and Particle Physics* **31**, S589 (2005).

[52] D. Thomas, *arXiv* **1308.5464** (2013).

[53] ALICE Collaboration, *JHEP* **112** (2012).

[54] CMS Collaboration, *JHEP* **05**, 063 (2012).

[55] CMS Collaboration, *CMS-PAS-HIN-12-14* (2012).

[56] R. A. Lacey, *Winter Workshop at Squaw Valley* (2013).

[57] S. Voloshin, Y. Zhang, *Z.Phys.* **C70**, 665 (1996).

[58] S. A. Voloshin, A. M. Poskanzer, R. Snellings (2008).

[59] J.-Y. Ollitrault, *Phys. Rev.* **D46**, 229 (1992).

[60] S. Voloshin, Y. Zhang, *Z. Phys.* **C70**, 665 (1996).

[61] A. M. Poskanzer, S. A. Voloshin, *Phys. Rev.* **C58**, 1671 (1998).

[62] J.-Y. Ollitrault, A. M. Poskanzer, S. A. Voloshin, *Phys. Rev.* **C80**, 014904 (2009).

[63] J.-Y. Ollitrault, *arXiv* **9711003** (1997).

[64] Y. Z. Hang, *Transverse Energy Distributions, Global Event Shapes, and Flow Study in Ultra-relativistic Heavy Ion Collisions* (1995).

[65] U. Heinz, R. Snellings, *Ann.Rev.Nucl.Part.Sci.* **63**, 123 (2013).

[66] I. Selyuzhenkov, S. Voloshin, *Phys.Rev.* **C77**, 034904 (2008).

[67] N. Borghini, P. M. Dinh, J.-Y. Ollitrault, *Phys.Rev.* **C63**, 054906 (2001).

[68] A. Bilandzic, *Anisotropic Flow Measurements in ALICE at the Large Hadron Collider* (2011).

[69] A. Bilandzic, N. van der Kolk, J.-Y. Ollitrault, R. Snellings, *Phys.Rev.* **C83**, 014909 (2011).

[70] S. Sakai, *Measurement of electron azimuthal anisotropy and implications of heavy quark flow in Au+Au collisions at* $\sqrt{s_{NN}} = 200$ *GeV*.

[71] ALICE Collaboration, *Phys. Rev. Lett.* **105**, 252302 (2010).

[72] Abelev, *et al.*, *Phys. Rev. Lett.* **111**, 102301 (2013).

[73] P. L. Evans, *JINST* **3**, S08001 (2008).

[74] CERN, http://te-epc-lpc.web.cern.ch/te-epc-lpc/machines/pagesources/Cern-Accelerator-Complex.jpg (2013).

[75] A. Collaboration, *Journal of Physics G: Nuclear and Particle Physics* **30** (2004).

[76] A. Collaboration", *Journal of Physics G: Nuclear and Particle Physics* **32**, 1295 (2006).

[77] *Philosophical Transactions of The Royal Society A Mathematical Physical and Engineering Sciences* **370**, 917 (2012).

[78] *The European Physical Journal Special Topics* **162**, 205 (2008).

[79] F. Antinori, the ALICE Collaboration, *Journal of Physics G: Nuclear and Particle Physics* **34**, S511 (2007).

[80] G. M. García, the ALICE Collaboration, *Journal of Physics G: Nuclear and Particle Physics* **34**, S943 (2007).

[81] C. Cavicchioli, *Journal of Instrumentation* **5**, C12001 (2010).

[82] *International Journal of Modern Physics E* **16**, 2445 (2007).

[83] B. S. C. Grupen, *Particle Detectors* (Cambridge).

[84] G. Knoll, *Radiation Detection and Measurement* (John Wiley and Sons).

[85] W. Leo, *Techniques for nuclear and particle physics experiments* (Springer).

[86] H. R. Schmidt, the Alice Experiment, *Journal of Physics: Conference Series* **230**, 012023 (2010).

[87] *Physics Procedia* **37**, 434 (2012).

[88] P. Cortese, *et al.*, *CERN-LHCC-2008-014* (2008).

[89] U. Abeysekara, *et al.*, *arXiv* **1008.0413** (2010).

[90] A. Fantoni, the ALICE collaboration, *Journal of Physics: Conference Series* **293**, 012043 (2011).

[91] F. Ronchetti, the ALICE collaboration, *Journal of Physics: Conference Series* **160**, 012012 (2009).

[92] O. Bourrion, *et al.*, *Journal of Instrumentation* **8**, C01013 (2013).

[93] A. Collaboration, *JINST* **5**, C12048 (2010).

[94] *Nucl. Instrum. Meth. A* **617**, 344 (2010).

[95] Y. Zoccarato, *et al.*, *Nuclear Instruments and Methods in Physics Research A-accelerators Spectrometers Detectors and Associated Equipment* **626**, 90 (2011).

[96] e. a. Y. Zoccarato, *Nuclear Instruments and Methods in Physics Research Section A: Accelerators, Spectrometers, Detectors and Associated Equipment* **626–627**, 90 (2011).

[97] P. Cortese, *et al.*, *CERN-LHCC-2004-025* (2004).

[98] ALICE collaboration, *Journal of Instrumentation* **8**, P10016 (2013).

[99] *Indian Journal of Physics* **85**, 965 (2011).

[100] J. Conrad, J. Contreras, C. Jorgensen, *ALICE-INT-2005-025* (2005).

[101] BNL, www.bnl.gov/rhic/news/061907/story2.asp (2013).

[102] M. L. Miller, K. Reygers, S. J. Sanders, P. Steinberg, *Ann.Rev.Nucl.Part.Sci.* **57**, 205 (2007).

[103] ALICE Collaboration, *Phys. Rev. Lett.* **106**, 032301 (2011).

[104] *Nuclear Instruments and Methods in Physics Research Section A Accelerators Spectrometers Detectors and Associated Equipment* **650**, 30 (2011).

[105] STAR collaboration, *STAR c++ class library* (1998).

[106] V. Russkikh, Y. Ivanov, *Phys.Rev.* **C74**, 034904 (2006).

[107] T. Rascanu, *Quark Matter* (2012).